

AMMONIA-WATER ABSORPTION IN THE PRESENCE OF SURFACE-ACTIVE AGENTS

A Dissertation
Presented to
The Academic Faculty

by

Girish Anant Kini

In Partial Fulfillment
of the Requirements for the Degree
Doctor of Philosophy in the
School of Mechanical Engineering

Georgia Institute of Technology
December 2021

COPYRIGHT © 2021 BY GIRISH ANANT KINI

AMMONIA-WATER ABSORPTION IN THE PRESENCE OF SURFACE-ACTIVE AGENTS

Approved by:

Dr. Srinivas Garimella, Chair
G.W. Woodruff School of Mechanical
Engineering
Georgia Institute of Technology

Dr. Ryan P. Lively
School of Chemical and Biomolecular
Engineering
Georgia Institute of Technology

Dr. G. P. "Bud" Peterson
G.W. Woodruff School of Mechanical
Engineering
Georgia Institute of Technology

Dr. Fani Boukouvala
School of Chemical and Biomolecular
Engineering
Georgia Institute of Technology

Dr. S. Mostafa Ghiaasiaan
G.W. Woodruff School of Mechanical
Engineering
Georgia Institute of Technology

Date Approved: December 1, 2021

To my parents for their unconditional love and unwavering support

ACKNOWLEDGEMENTS

I would like to express my deepest gratitude to my adviser, Dr. Srinivas Garimella, for his guidance, support, and continuous encouragement to strive for excellence throughout my graduate education. I have always valued his advice both in my professional and personal spheres, and I hope this is the beginning of a long association. I would like to thank my Ph.D. committee members, Drs. G.P. “Bud” Peterson, Ryan Lively, Fani Boukouvala, and S. Mostafa Ghiaasiaan for their valuable suggestions and patient perusal of my dissertation.

I would also like to thank all the current and past members of the Sustainable Thermal Systems Laboratory for their friendship and support. I would like to particularly thank Dr. Anurag Goyal, Dr. Bachir ElFil, Dr. Daniel Boman, Subhrajit Chakraborty, Sriram Chandrasekaran, Christy Green, Matthew Hughes, and Roland Crystal for their assistance and camaraderie during this process.

My parents have been role models and their dedication and hard work is something I strive to emulate every single day. I would like to thank my extended family for always supporting me. I would specifically like to thank Dr. Amrit Ambirajan, who introduced me to this exciting world of research, and specifically, energy systems. I would also like to thank my friends, Supreeth, Vidyashankar and Subhrajit, who played a constant role, especially during the lows of the pandemic. Most importantly, I would like to thank my fiancée, Eureka. Her advice, patience, encouragement, and companionship are a big part of why I was able to complete this journey.

TABLE OF CONTENTS

ACKNOWLEDGEMENTS	iv
LIST OF TABLES	viii
LIST OF FIGURES	ix
LIST OF SYMBOLS AND ABBREVIATIONS	xiii
SUMMARY	xviii
CHAPTER 1. Introduction	1
1.1 Literature review	4
1.1.1 Ammonia-water absorption	4
1.1.2 Surfactants in absorption heat pumps	8
1.2 Research needs and scope of present work	17
1.3 Research Objectives	18
1.4 Thesis organization	19
CHAPTER 2. Surfactant selection and modeling framework	21
2.1 Introduction	21
2.2 Surfactant selection criterion	25
2.3 Surface tension measurements	28
2.3.1 Experimental method	28
2.3.2 Surface tension measurements	30
2.4 Model development	33
2.5 Results	38
2.5.1 Temperature and concentration profiles	38
2.5.2 Component performance	41
2.6 Conclusions	42
CHAPTER 3. Two-phase flow in the presence of surfactants	44
3.1 Introduction	44
3.2 Test matrix	47
3.3 Experimental Facility	51
3.4 Data analysis methodology	51
3.4.1 Pre-processing	51
3.4.2 Interfacial area	54
3.4.3 Velocity	58
3.5 Results	59
3.5.1 Flow patterns	60
3.5.2 Interfacial area	63
3.5.3 Velocity	69

3.6	Conclusions	72
CHAPTER 4.	Effect of surfactants on the performance of bubble absorbers	74
4.1	Introduction	74
4.2	Experimental test section and facility	76
4.2.1	Measurements and instrumentation	78
4.3	Data reduction	81
4.4	Experimental results	84
4.4.1	Energy balance	84
4.4.2	Effect of coupling fluid flow rate	86
4.4.3	Effect of surfactant concentration	87
4.4.4	Thermal resistance	88
4.5	Model development	91
4.6	Model results	100
4.6.1	Adiabatic section	100
4.6.2	Heat transfer section	102
4.7	Conclusions	106
CHAPTER 5.	Effect of surfactants on performance of falling-film absorbers	108
5.1	Introduction	108
5.2	Experimental approach	111
5.3	Data reduction	117
5.3.1	State point determination	117
5.3.2	Heat transfer resistance network	120
5.4	Results	122
5.4.1	Effect on absorber performance	123
5.4.2	System level effects	129
5.5	Conclusions	133
CHAPTER 6.	Comparison of bubble and falling-film modes of absorption	135
6.1	Introduction	135
6.2	Operating conditions	136
6.3	Absorber geometry	136
6.3.1	Falling-film absorber	137
6.3.2	Bubble absorber	140
6.4	Modeling framework	142
6.4.1	Falling-film absorber model	142
6.4.2	Bubble absorber model	145
6.5	Results	147
6.6	Conclusions	152
CHAPTER 7.	Conclusions and Recommendations	153
7.1	Recommendations for future work	155

APPENDIX A. Data reduction and uncertainty propagation	158
A.1 Data reduction for a sample point	159
APPENDIX B. Model sample calculation	163
REFERENCES	173

LIST OF TABLES

Table 1.1: Summary of surfactant-enhanced absorption literature	11
Table 2.1: Summary of experimental conditions	31
Table 4.1: Instrumentation and uncertainties	80
Table 4.2: Bubble absorber test matrix	81
Table 5.1: Absorber geometry details	112
Table 5.2: Instrumentation specification in the facility	116
Table 5.3: Test matrix for falling-film experiments	117
Table 6.1: Operating conditions of the absorber	137
Table 6.2: Geometry of falling-film absorbers	139
Table 6.3: Geometry of bubble absorber	141
Table 6.4: Heat transfer correlations for cross-flow through tube banks	145

LIST OF FIGURES

Figure 1.1: Vapor absorption cycle.....	3
Figure 1.2: Typical temperature and concentration profile	5
Figure 1.3: Heat and mass transfer resistances	5
Figure 1.4: (a) Falling film absorber (b) Bubble absorber.....	6
Figure 2.1: Summary of the literature.....	25
Figure 2.2: Surface tension of fluid with added surfactant.....	26
Figure 2.3: Mass transfer dependency on Marangoni number	28
Figure 2.4: Experimental facility (a) schematic (b) photograph.....	30
Figure 2.5: Droplet with 1-octanol 0 PPM (left) 1000 PPM (right)	31
Figure 2.6: Surface tension of ammonia-water solution with 1-octanol.....	33
Figure 2.7: Surface tension with four additives.....	34
Figure 2.8: Representative segment of the falling-film absorber	36
Figure 2.9: Results for absorber without surfactant.....	39
Figure 2.10: Results for absorber with 500 PPM of 1-octanol	40
Figure 2.11: Concentration profile in absorber with 500 PPM of 1-octanol	40
Figure 3.1: Flow regimes in upward flow.....	48
Figure 3.2: Variation of circulation ratio	49
Figure 3.3: Region of interest for bubble absorbers	50
Figure 3.4: Test matrix.....	50
Figure 3.5: (a) Experimental facility (b) Test section.....	52
Figure 3.6: Determination of pixel-to-mm conversion	53

Figure 3.7: Flow visualization steps (a) flow image (b) calibration image (c) de-noised image (d) Edge detection (e) final image.....	55
Figure 3.8: Algorithm to calculate interfacial area	57
Figure 3.9: Effect of surfactant on flow patterns	61
Figure 3.10: Comparison of slug flow in the presence of surfactant	63
Figure 3.11: Variation of interfacial area concentration with superficial velocities.....	65
Figure 3.12: Group 1 bubble density variation	66
Figure 3.13: Measured versus predicted IAC	68
Figure 3.14: Visualization of optical flow algorithm.....	69
Figure 3.15: Tracer independence for optical flow.....	70
Figure 3.16: Velocity results.....	71
Figure 3.17: Effect of surfactant on bubble path	72
Figure 4.1: (a) Test section schematic (b) Detailed view of adiabatic mixing section.....	77
Figure 4.2: Schematic of experimental facility.....	78
Figure 4.3: Photograph of test facility	79
Figure 4.4: Heat transfer resistance network	83
Figure 4.5: Energy balance of all data points	85
Figure 4.6: Effect of coupling fluid flow rate	86
Figure 4.7: Effect of surfactant concentration	88
Figure 4.8: Variation of apparent heat transfer coefficient with the addition of 1-octanol	89
Figure 4.9: Solution resistance as a fraction of the overall resistance	90
Figure 4.10: Variation of absorber performance with system pressure	91

Figure 4.11: Representative segment for the heat and mass transfer.....	93
Figure 4.12: Heat and mass transfer resistances for bubble absorber model.....	93
Figure 4.13: Resistance network for determining wall temperatures	98
Figure 4.14: Temperature profiles in the adiabatic mixing section	101
Figure 4.15: Temperature profiles along the entire length of the absorber	102
Figure 4.16: Comparison of temperature profiles with and without surfactant.....	103
Figure 4.17: Comparison of interfacial area concentration with and without surfactant	104
Figure 4.18: Comparison of mass flow rates and heat duty with and without surfactant	105
Figure 4.19: Comparison between predicted and measured absorber heat duties	106
Figure 5.1: Shell-and-tube absorber schematic.....	113
Figure 5.2: Experimental facility	114
Figure 5.3: Photograph of experimental facility	115
Figure 5.4: Error versus assumed degree of subcooling	118
Figure 5.5: Thermal resistance network.....	121
Figure 5.6: Heat duty balance between coupling and working fluids.....	123
Figure 5.7: Variation of absorber UA with coupling fluid inlet temperature.....	124
Figure 5.8: Variation of solution heat transfer coefficient.....	125
Figure 5.9: Thermal resistance of a single tube in the absorber	126
Figure 5.10: Absorber closest approach temperature (CAT)	127
Figure 5.11: Absorber UA at lower solution flow rate $\dot{m}_{conc} = 24 \times 10^{-3} \text{ kg s}^{-1}$	128
Figure 5.12: Variation of wetting area ratio.....	129
Figure 5.13: Steady state absorber pressure.....	130
Figure 5.14: Effect of 1-octanol on desorber UA	132

Figure 5.15: Effect of 1-octanol on desorber normalized energy input.....	133
Figure 6.1: Schematic of falling-film absorber.....	138
Figure 6.2: Schematic of bubble absorber	140
Figure 6.3: Liquid-vapor distribution at the bottom of bubble absorber	141
Figure 6.4: Absorber heat duty for falling-film design 1.....	147
Figure 6.5: Absorber heat duty for falling-film design 2.....	148
Figure 6.6: Absorber duty for bubble mode.....	149
Figure 6.7: Comparison of absorber duties in the presence of surfactants	150
Figure 6.8: Comparison of absorber mass and surface area	151

LIST OF SYMBOLS AND ABBREVIATIONS

A	area	(m^2)
C	concentration	(kg m^{-3})
CAT	closest approach temperature	(K)
CR	circulation ratio	(-)
C_t	Multiplication factor for churn flow	(-)
c_p	specific heat	$(\text{J kg}^{-1} \text{K}^{-1})$
d	diameter	(m)
D	diffusivity	$(\text{m}^2 \text{s}^{-1})$
\tilde{E}_{des}	normalized desorber energy input	(kJ kg^{-1})
h	specific enthalpy	(J kg^{-1})
k	thermal conductivity	$(\text{W m}^{-1} \text{K}^{-1})$
g	gravitational constant	(m s^{-2})
G	mass flux	$(\text{kg m}^{-2}\text{s}^{-1})$
I	pixel intensity	(-)
IA	interfacial area	(m^2)
IAC	interfacial area concentration	(m^{-1})

j	superficial velocity	(m s ⁻¹)
L	tube length	(m)
L_o	Laplace length	(m)
LMTD	log-mean temperature difference	(K)
\dot{m}	mass flow rate	(kg s ⁻¹)
Ma	Marangoni number	(-)
\dot{n}''	molar flux of species undergoing absorption	(kmol m ⁻² s ⁻¹)
OD	outer diameter	(m)
P	pressure	(kPa)
q	vapor quality	(-)
\dot{Q}	heat transfer rate	(W)
R	thermal resistance	(K W ⁻¹)
Re	Reynolds number	(-)
Sc	Schmidt number	(-)
Sh	Sherwood number	(-)
T	temperature	(°C)
u	velocity along x-axis	(m s ⁻¹)
UA	overall heat transfer conductance	(W K ⁻¹)

\dot{V}	volumetric flow rate	$(\text{m}^3 \text{ s}^{-1})$
v	velocity along y-axis	(m s^{-1})
Vol	volume	(m^3)
x	ammonia concentration (mass basis)	$(-)$
\tilde{x}	ammonia concentration (molar basis)	$(-)$
\tilde{z}	molar concentration of condensing flux	$(-)$

Greek Symbols

α	heat transfer coefficient, void fraction	$(\text{W m}^{-2} \text{ K}^{-1}, -)$
β	mass transfer coefficient	(m s^{-1})
δ	liquid film thickness	(m)
ε	energy dissipation rate per unit mass	$(\text{m}^2 \text{ s}^{-3})$
μ	dynamic viscosity	$(\text{kg m}^{-1} \text{ s}^{-1})$
ρ	density	(kg m^{-3})
Φ	heat transfer correction parameter	$(-)$
φ	wetting area ratio	$(-)$
σ	surface tension	(N m^{-1})
ν	kinematic viscosity	$(\text{m}^2 \text{ s}^{-1})$

Subscript

1	Group 1 bubbles
---	-----------------

2	Group 2 bubbles
A	ammonia
abs	absorber
app	apparent
avg	average
CF	coupling fluid
conc	concentrated solution
cond	conduction
des	desorber
dil	dilute solution
eqv	equivalent
film	liquid solution film
in	inlet
int	interfacial
mix	mixture
out	outlet
seg	segment
sol	liquid solution
sm	sauter mean

subcool	solution Subcooling
surf	surfactant
vap	vapor
W	water
wf	working fluid

SUMMARY

Absorption-based heating, ventilation, and air conditioning (HVAC) systems have received increased interest in recent years due to their ability to use low-grade waste heat streams, and the low global warming potential of their working fluids. Advances in manufacturing have led to the development of heat exchangers with microscale features that demonstrate enhanced heat and mass transfer. While these developments have resulted in more efficient and compact absorption systems, the system performance depends significantly on the absorber, which absorbs the refrigerant ammonia vapor into the absorbent fluid. The absorber can often be the largest component in the system and dictates system size. Thus, enhancement of absorption will directly translate to more efficient and compact systems.

Surface active agents or surfactants have the potential to substantially enhance heat and mass transfer in ammonia-water absorption by reducing the surface tension of the working fluid. The enhancement is caused by improved interactions at the vapor-liquid interface that result from surface tension gradients. Absorbers are designed to operate in either the bubble mode or the falling-film mode. In this study, the effect of surfactants on absorber performance is evaluated for both configurations. A screening analysis is conducted to identify the ideal surfactant based on the value of surface tension and critical concentration. It is determined that 500 PPM of 1-octanol is the preferred additive. A flow visualization study is performed to understand the impact of surfactants on flow parameters such as bubble radii, interfacial area, and velocities in bubble absorbers. The addition of 1-

octanol results in enhancement in interfacial area by up to 37% due to the prevention of bubble coalescence leading to many small diameter bubbles.

Ammonia-water bubble absorption experiments are conducted to evaluate the effect of adding surfactants. Enhancements in mass transfer coefficient and interfacial area result in a reduction in absorber size by 25%. A detailed heat and mass model is developed to predict the performance of the bubble absorber in the presence of surfactants with an AAD of 8.2%. The performance of a falling-film absorber in the presence of surfactants is evaluated in a two-pressure experimental facility. A reduction of 37% in the solution-side resistance is achieved due to Marangoni convection and improved wetting. In addition to understanding the changes in the absorber, these experiments demonstrate the reduction in low-side pressure and the benefits to the overall system performance by the addition of surfactants. Finally, a comparative assessment between the two absorption modes is conducted. Prototype falling-film and bubble absorbers are designed for a representative absorber that is part of a 10.5 kW cooling capacity absorption chiller. The bubble absorber is found to be favorable overall due to its performance, low cost, and simpler design. The results and insights gained from this work will guide the development of enhanced absorbers and compact sorption heat pumps.

CHAPTER 1. INTRODUCTION

With an increasing emphasis on the reduction of electricity consumption and the eventual phasing out of commonly used refrigerants, there is renewed interest in non-vapor compression technologies for space conditioning. Thermally driven systems replace electricity as the main energy input with low-grade thermal energy, which can be in the form of waste heat or solar energy. The advantages of such a system are multi-fold – a more efficient overall energy system based on primary energy use, flexible use of energy sources, and avoidance of environmentally deleterious synthetic refrigerants. Specifically, the vapor absorption cycle has been in use for over a century. But due to typical component size requirements for absorption systems, the proliferation of vapor compression machines relegated absorption systems to large capacity industrial applications (Darwish et al., 2008). However, recent developments in microscale heat and mass exchangers have led to the development of small capacity machines that can be used for residential and mobile applications (Garimella et al., 2016).

Vapor absorption systems use binary fluid mixtures as working fluids. Many combinations have been considered, but only the working pairs of ammonia-water and water-lithium bromide are currently considered to be commercially viable. Water- lithium bromide is not suitable for operation below freezing temperatures as water is the refrigerant. Further, crystallization concerns limit the range of operating conditions. Ammonia as a refrigerant has favorable transport and thermodynamic properties and is suitable for refrigeration and low-temperature applications. In addition, the specific volume of ammonia vapor at typical operating pressures is sufficiently small to enable the use of

microchannel heat exchangers without excessive pressure drop requirements. Figure 1.1 shows a schematic of a single-effect ammonia-water absorption heat pump. The left side of the cycle, i.e., condenser, evaporator, and refrigerant pre-cooler, closely resembles the corresponding portion of a vapor compression cycle. In the vapor absorption cycle, however, the mechanical compressor is replaced with a set of heat exchangers and a pump. Their combined objective is to produce high pressure refrigerant vapor while receiving low pressure refrigerant. Heat input to the thermal compressor is used in a thermal separation process of a mixture consisting of an absorbent and a refrigerant. The latter is the more volatile constituent, allowing for separation from the absorbent during phase change. This process occurs in the desorber. The refrigerant-depleted absorbent (dilute solution) is expanded to a low pressure at the absorber inlet. Refrigerant from the refrigerant pre-cooler is absorbed into that stream in the absorber. This process is exothermic and requires heat rejection. The coefficient of performance (COP) is used to assess the performance of heat pumps. The primary energy factor is used to convert any electrical input to the equivalent thermal energy.

$$COP = \frac{\dot{Q}_{cool}}{\dot{Q}_{in,total}} \quad (1.1)$$

The performance of the absorber often limits the performance of the overall system (Goyal et al., 2017; Jiménez-García and Rivera, 2019), and can also be the largest component in the system, thereby dictating system size. Absorption of ammonia vapor into a dilute ammonia-water solution is a coupled heat and mass transfer process, typically limited by the high mass transfer resistance (Hoysall and Garimella, 2019). The high mass transfer resistance can be attributed to the low diffusivity of ammonia and low circulation

velocity in microscale geometries. The addition of surface-active agents or surfactants to the working fluid could lead to increased interfacial turbulence and better absorption. The interfacial turbulence is induced by surface tension gradients, also known as the Marangoni effect. Although surfactants have been studied well for water-LiBr absorption systems, their effect on ammonia-water systems is not well understood. This lack of understanding of the underlying phenomena has hindered the development of surfactant enhanced ammonia-water absorption systems.

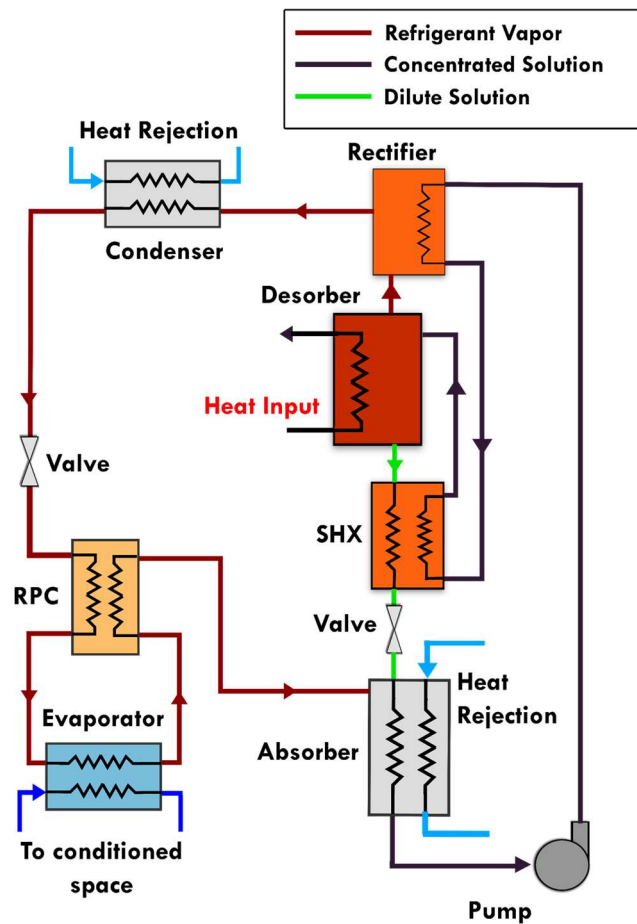


Figure 1.1: Vapor absorption cycle

In the proposed effort, the effect of surfactants on ammonia-water absorption will be understood for geometries and conditions relevant to absorption heat pumps.

1.1 Literature review

1.1.1 Ammonia-water absorption

The dilute solution combines with the ammonia vapor in the absorber and leaves as a concentrated solution. During phase change of the binary mixture, non-equilibrium conditions exist in the vapor and liquid bulk, while equilibrium exists at the vapor-liquid interface. The temperature and concentration in vapor and liquid bulk are different from those at the interface, resulting in temperature and concentration gradients in the respective phases that act as the driving potential for the heat and mass transfer (Figure 1.2). During absorption, the working fluid undergoes significant changes in temperature and concentration, which could result in unfavorable gradients between the bulk and interface for heat and mass transfer. In addition, the absorption process is exothermic and releases a substantial amount of heat. The heat and mass transfer resistances involved in this process are shown in Figure 1.3. These factors necessitate a large surface area for the absorber, resulting in increased overall dimensions of absorption heat pumps.

Absorbers typically operate in either the falling-film or the bubble/forced convection configuration (Figure 1.4). In the falling-film configuration, the absorbent liquid film flows due to gravity over horizontal or vertical tube banks. Ammonia vapor can be introduced either pre-mixed in co-current flow, or the absorbent and refrigerant vapor streams could be in counterflow. In the bubble mode, the refrigerant is bubbled through a pool of stationary or flowing liquid absorbent.

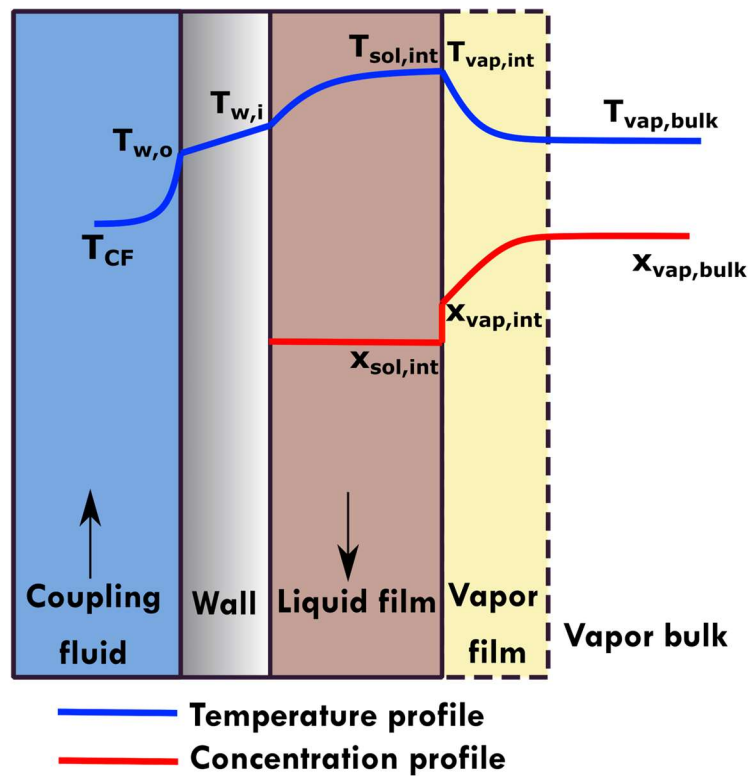


Figure 1.2: Typical temperature and concentration profile

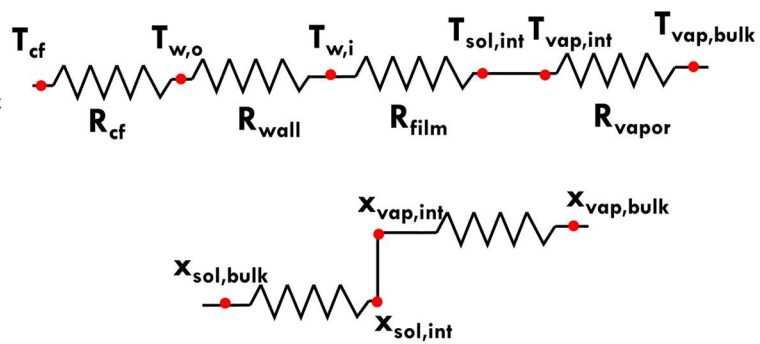


Figure 1.3: Heat and mass transfer resistances

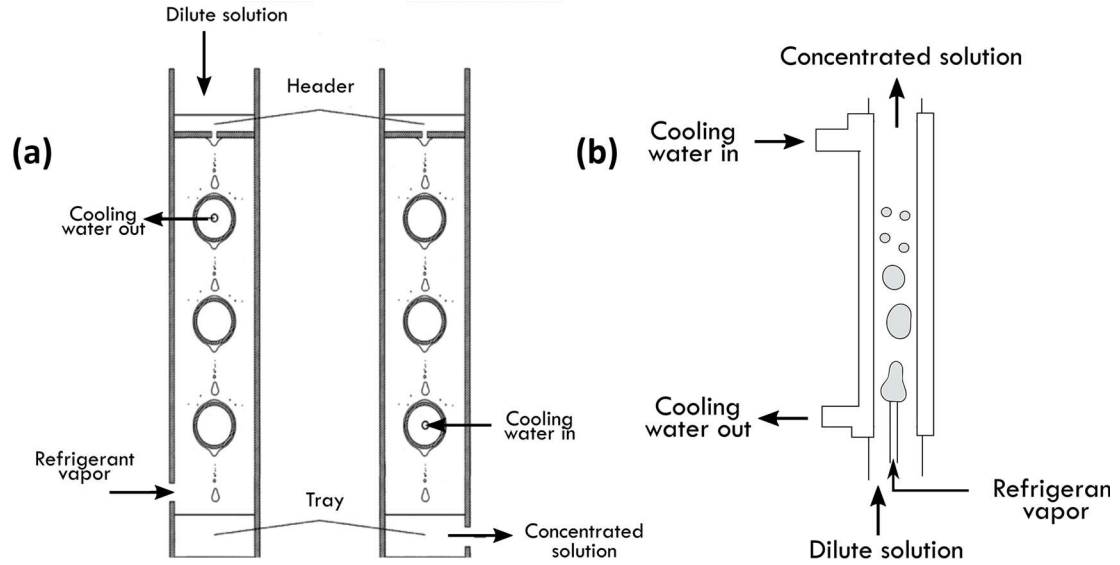


Figure 1.4: (a) Falling film absorber (b) Bubble absorber

Kang et al. (2000) compared the performance of falling-film and bubble absorbers analytically in a plate heat exchanger. They reported that the absorption rate during bubble mode was always higher than during falling-film mode, noting that a bubble absorber can be ~49% smaller than a falling-film absorber for the same duty. The models showed that the vapor side presented the dominant heat transfer resistance in the falling-film mode. It was also observed that in bubble mode, the dominant mass transfer resistance was on the liquid side. Castro et al. (2009) compared the performance of air-cooled falling film and bubble absorbers. Absorption in the bubble mode was observed to outperform falling-film absorption at low flow rates, which was attributed to wetting issues. As the solution flow rate increased, tube wetting increased, and the performance of both modes was comparable.

Meacham and Garimella (2004) demonstrated a compact falling-film absorber using alternating mutually perpendicular arrays of small diameter horizontal tubes. This

design yielded high heat and mass transfer rates with low resistances on both the solution and coolant sides. The vapor was introduced in counter flow. Kwon and Jeong (2004) developed a falling-film helical coil absorber and studied the effect of the vapor flow direction. They observed that in countercurrent flow, the increase in vapor flow rate beyond a threshold deteriorated heat and mass transfer performance. Triché et al. (2017) investigated the use of a plate-heat-exchanger in the falling-film configuration and concluded that the design is limited by solution-side mass transfer resistance. Nagavarapu and Garimella (2019) presented an experimentally validated heat and mass transfer model for falling-film absorption over horizontal microchannel tube banks. The Nusselt number correlation developed in this study, when coupled with a suitable hydrodynamic model, was found to predict the performance of other falling film studies on horizontal tube banks in the literature well.

Vertical tubular absorbers have been investigated for bubble mode absorption, and several authors have identified distinct flow regimes during absorption: churn flow, slug flow, and bubble flow (Ferreira et al., 1984; Kim et al., 2003a). The bubbles resemble the shape of a Taylor bubble and some authors refer to these absorbers as slug flow absorbers. Kim et al. (2003b) presented a heat and mass transfer model to estimate local transfer coefficients during absorption. They used a drift flux model with Taylor bubbles to model the slug flow and accounted for the interfacial area. The heat and mass transfer analogy was used to estimate mass transfer coefficients from the heat transfer coefficients. Fernández-Seara et al. (2005) investigated ammonia-water absorption in a shell-and-tube absorber in co-current flow configuration. The ammonia vapor is introduced as bubbles into the tubes as the weak solution flows upwards. They used correlations in the literature

and the Colburn and Drew (1937) framework to estimate the heat and mass transfer rates. They reported that churn flow was expected to be merely an entrance effect and was followed by transition to slug flow. High absorption rates were observed in churn and slug flow regimes. Many researchers have investigated bubble absorption in plate-heat-exchangers (Lee et al., 2002; Jung et al., 2014; Jiménez-García and Rivera, 2019). Correlations have been developed for the Sherwood number, Nusselt number, and initial bubble diameter. It should be noted, however, that these authors often neglect mass transfer in the vapor phase for data reduction. Cerezo et al. (2009) demonstrated the use of a plate heat exchanger in the bubble mode and showed that increases in system pressure, solution or cooling water flow rates improve absorber performance.

1.1.2 Surfactants in absorption heat pumps

Surfactants have been widely used and studied for water-LiBr absorption systems. The enhancement caused by surfactants was first reported by Kashiwagi (1985). Based on experimental evidence from three additives, Beutler et al. (1996) concluded that 2-ethyl-1-hexanol (2E1H) caused the best enhancement by a factor of 1.5. However, they concluded that the reduction in surface tension cannot be the only reason for enhancement, as the addition of 1-decanol reduced surface tension but did not enhance performance. Hoffmann et al. (1996) investigated the effect of surfactants on a horizontal falling-film water-LiBr absorber and suggested that the improvement in performance was due to the combined effect of surface tension reduction and change in droplet characteristics. Kulankara and Herold (2000) studied the effect of surfactants on falling-films over vertical tubes and developed the so-called vapor surfactant theory. Möller and Knoche (1996) were the first to conduct experiments on the ammonia-water working fluid and concluded that 50 PPM

of 1-octanol resulted in the best enhancement in a bubble absorber. Kim et al. (2006) visually investigated the effect of surfactants and confirmed that Marangoni convection played a role in the enhancement of performance. They suggest using 700 PPM of 2-ethyl-1-hexanol to maximize absorption rates in the bubble mode. Kim et al. (2007b) showed enhancement in ammonia-water bubble absorbers by adding copper nanoparticles. It must be noted that all ammonia-water studies, except Hoysall and Garimella (2019), are conducted on the bubble mode of ammonia-water absorption. There is a need to study the effect of these additives in convective flow and falling-film absorbers. Excepting Marlon-A, an anionic tenside, all studies employed various hydrocarbon alcohols as the additive. A few different theories have been proposed to explain the mechanism of enhancement. Kashiwagi (1988) explained the enhancement in water-LiBr based on Marangoni convection. He proposed that the presence of droplets or islands of additive on the surface is required to induce Marangoni convection. It is thus referred to as the island theory. The strong gradients of surface tension around these islands during absorption results in Marangoni convection. According to this model, the additive concentration should exceed the solubility limit and thus be able to form droplets on the surface. However, many studies have reported the presence of islands is not a necessary condition for enhancement.

According to the radical out effect, additive molecules dissociate in the solution, with one part dissolving in the bulk solution and the other part adsorbing on the surface. For instance, 1-octanol dissociates into $C_8H_{17}^+$ and OH^- . The OH^- ion bonds with NH_4^+ , allowing the $C_8H_{17}^+$ ions to diffuse to the interface and reduce local surface tension in various regions, resulting in interfacial turbulence (Kim et al., 2006). Kulankara and Herold (2000) proposed the vapor surfactant theory to explain the enhancement caused by

surfactants in water-LiBr absorption chillers. This theory also attributes the enhancement to Marangoni convection but differs from other theories in how the instability is induced. According to this theory, some of the alcohol vaporizes and travels in the vapor phase and condenses on the vapor-liquid surface, leading to secondary flows. A summary of surfactant-enhanced absorption literature is presented in Table 1.1.

Table 1.1: Summary of surfactant-enhanced absorption literature

Study	Working fluids	Experimental method	Results
Kim et al. (1996)	Working fluid: H ₂ O-LiBr Surfactant: 2-ethyl-1-hexanol (2E1H)	Vertical falling film, single tube. Cooling water included. Heat and mass transfer based experiments.	<ul style="list-style-type: none"> • Mass transfer enhancement observed and quantified • Interfacial turbulence starts at 3-6 ppm and is maximum at 30 ppm
Möller and Knoche (1996)	Working Fluid: NH ₃ -H ₂ O Surfactants: Tensides (Marlon A, Marlon PS, Dehydol), 1-Octanol	Pool experiments	<ul style="list-style-type: none"> • Surface tension reduction by tensides did not result in enhancement. • 50 ppm of dissolved 1-Octanol demonstrated highest enhancement • Findings do not support island theory.
Nordgren and Setterwall (1996)	Working fluid - Water	Vertical falling film experiments of water-glycerol mixture Effect of surfactant on surface wave in long falling distance	<ul style="list-style-type: none"> • Addition of surfactant below solubility limit stabilizes surface wave, while the addition of surfactant above the limit helps in destabilizing the wave

Table 1.1: Summary of surfactant-enhanced absorption literature (continued)

Study	Working fluids	Experimental method	Results
Hoffmann et al. (1996)	Working fluid: H ₂ O-LiBr Surfactant: 2-ethyl-1-hexanol and 1-octanol	Falling film over horizontal tubes. (both plain and knurled) Additives were added in varying concentrations from 10 to 600 ppm	<ul style="list-style-type: none">• Improvement in heat transfer coefficient attributed to reduced surface tension, different droplet characteristics.• Knurled tubes perform better both with and without additives.
Beutler et al. (1996)	Working fluid: H ₂ O-LiBr Surfactant: 2-ethyl-1-hexanol, 1-octanol and 1-decanol	Falling film over horizontal tubes.	<ul style="list-style-type: none">• Reduction in surface tension by itself does not lead to improved heat transfer.• 1-Decanol reduced surface tension but did not improve heat transfer.
Kang et al. (1999b)	Working Fluid: NH ₃ -H ₂ O Surfactants: 2E1H, n-Octanol, 2-Octanol, 3-Octanol, 4-Octanol, n-Decanol, 2-Decanol and 3-Decanol	Measurement of surface tension by Wilhelmy plate method Optical method to visualize Marangoni convection using shadowgraph technique.	<ul style="list-style-type: none">• Radical out effect provides explanation.• Solubility limits of additives are much higher in NH₃-H₂O• Exceeding solubility not necessary to induce convection but it enhances it.

Table 1.1: Summary of surfactant-enhanced absorption literature (continued)

Study	Working fluids	Experimental method	Results
Kulankara and Herold (2000)	Working fluid: H ₂ O-LiBr Surfactant: 2-ethyl-1-hexanol and 1-octanol	Absorption: Falling film along vertical tube with vapor and solution in co-flow. Condensation: Water condensation in presence of 2-ethyl-1-hexanol.	<ul style="list-style-type: none"> • Enhancement observed within a second of addition of surfactant implying that the transport is in vapor phase. • Condensation mode changes from filmwise to dropwise with the addition of 2-ethyl-hexanol. • Results led to the development of vapor surfactant theory
Kulankara and Herold (2002)	Working fluid: H ₂ O-LiBr Surfactant: 2-ethyl-1-hexanol, 3,5,5-trimethyl-1-hexanol, 2-methyl-1-hexanol and 3-phenyl-1-propanol	Drop weight method used for determining surface tension	<ul style="list-style-type: none"> • The distance from the tip of the needle to the collection vessel greatly influenced the value of surface tension. • Effect of additive vapor on surface tension is pronounced but is not quantified.

Table 1.1: Summary of surfactant-enhanced absorption literature (continued)

Study	Working fluids	Experimental method	Results
Kang and Kashiwagi (2002)	Working fluid: $\text{NH}_3\text{-H}_2\text{O}$ Surfactant: 1-Octanol	Ammonia vapor sprayed from top into a pool of solution. Optical measurements by holographic interferometer.	<ul style="list-style-type: none"> • Marangoni convection observed only with additive. • Enhancement in the order of 3 to 4.6 times. • Interface temperature is higher with surfactants.
Kim et al. (2006)	Working fluid: $\text{NH}_3\text{-H}_2\text{O}$ Surfactant: 2-ethyl-1-hexanol, n-octanol and 2-octanol	Bubble absorber with no coupling fluid. Mass based experiments.	<ul style="list-style-type: none"> • Two competing effects – Marangoni convection and Barrier effect. • Correlations developed for effective absorption enhancement based on experimental findings.

Table 1.1: Summary of surfactant-enhanced absorption literature (continued)

Study	Working fluids	Experimental method	Results
Kang and Kim (2006)	Working fluid: H ₂ O-LiBr Surfactant: n-octanol	Falling film absorption over horizontal tubes for H ₂ O-LiBr. Hatched and bare tubes tested.	Enhancement observed for H ₂ O-LiBr <ul style="list-style-type: none"> • Hatched tubes, no additives: 2.4 • Bare tubes with additives: 3.8 • Hatched tubes with additives: 4.5
	Working fluid: NH ₃ -H ₂ O Surfactant: 2-ethyl-1-hexanol, n-octanol, 2-octanol and nanofluids	Bubble absorption for NH ₃ -H ₂ O	Enhancement observed for NH ₃ -H ₂ O <ul style="list-style-type: none"> • 2E1H additive: 4.6; n-octanol: 4 • Additives are more effective than nanoparticles when difference in concentration between solution and vapor is low.
Zhang et al. (2019)	Working fluid: H ₂ O-LiBr Surfactant: 2-ethyl-1-hexanol and 1-octanol	Horizontal falling-film absorber. Coupled heat and mass transfer experiments.	<ul style="list-style-type: none"> • Enhancement in both heat and mass transfer coefficients observed • Mass transfer coefficient enhancement is twice of α • Peak enhancement observed at 160-320 PPM • Further addition of surfactant results in no additional change

Table 1.1: Summary of surfactant-enhanced absorption literature (continued)

Study	Working fluids	Experimental method	Results
Hoysall and Garimella (2019)	Working fluid: $\text{NH}_3\text{-H}_2\text{O}$ Surfactant: 1-octanol,	Vertical microchannels of depth 500 μm and width 760 μm . Coupled heat and mass transfer experiments.	<ul style="list-style-type: none">• Apparent heat transfer coefficient enhancement by 30-50%• Marangoni convection primary reason for enhancement• Improved flow distribution in header due to low surface tension.

1.2 Research needs and scope of present work

The above discussion shows that ammonia-water absorption remains a complex process to simulate due to the coupled heat and mass transfer processes, and the resulting concentration and temperature gradients in both phases. Although surfactants have been studied well for water-LiBr absorption systems, their effect on ammonia-water systems is not well understood. Even the choice of surfactant has not been substantiated in the literature. The effect of surfactants on hydrodynamics, wetting, and heat and mass transfer in different geometries is not clear. This lack of understanding of the underlying phenomena has prevented the development of surfactant enhanced ammonia-water absorption systems.

For the case of hydrodynamics, there are a handful of studies in the literature that investigate two-phase flow with surfactants. Most of them use a two-phase mixer at the inlet of the test section. However, there are many flow systems in which dispersed bubbles flow through single orifice nozzles into a liquid stream (Kuo and Wallis, 1988). This is especially relevant to bubble absorbers for ammonia-water absorption heat pumps (Cerezo et al., 2009; Amaris et al., 2018). In addition, Lioumbas et al. (2006) investigated two-phase flow patterns with surfactants for downward flow and inferred that flow patterns depended upon surfactant chemical structure in addition to surface tension values. Therefore, it is important to study changes to flow parameters in the presence of the surfactant in consideration of the exact flow geometries.

The models that are proposed in the literature predict enhancement due to surfactant addition using an enhancement factor derived from experimental results (Kim et al., 2006).

Most models for bubble absorbers use simplistic assumptions such as uniform bubble size, which can be a source for significant error. Experimental studies have often been conducted on stand-alone, bench-top, single component, single-pressure test facilities where the absorbers are tested under conditions that are not representative of space-conditioning systems, and influences of other absorption system components are not considered. Therefore, there is a need to develop a theory-based, experimentally validated model that can capture the coupled heat and mass transfer processes during ammonia-water absorption in the presence of surfactants.

1.3 Research Objectives

The primary objective of the proposed work is to demonstrate enhancement in ammonia-water absorption and to understand the mechanisms of enhancement in geometries and conditions relevant to absorption heat pumps by adding surfactants. To accomplish this objective, the following tasks are proposed:

1. Systematic screening of surface-active agents by measuring surface tension values in ammonia-water solutions.
2. Investigation of two-phase flow through a single-orifice nozzle in the presence of the selected surfactant, and the quantitative analysis of flow parameters.
3. Heat and mass transfer modeling of a bubble absorber in the presence of surfactants with experimental validation in a single-pressure facility.
4. Investigation of surfactants on the performance of a microchannel shell and tube falling-film absorber in a two-pressure facility.

5. Development of guidelines based on the findings of this study for the design of different absorber geometries enhanced with surfactants.

1.4 Thesis organization

This dissertation is organized as follows:

- Chapter 2 presents experimental results from the surfactant screening study and introduces a modelling framework to evaluate the heat and mass transfer enhancement due to the addition of surfactant.
- Chapter 3 investigates air-water two-phase flow in the presence of surfactants and presents flow visualization results. This chapter also quantifies the changes in flow behavior due to the addition of surfactants.
- Chapter 4 presents an investigation on surfactant-enhanced ammonia-water bubble absorption. Development of the experimental facility, experimental procedures, and the data reduction methodology are discussed. This chapter also describes the development of a heat and mass transfer model to predict bubble absorber performance.
- Chapter 5 describes the effect of surfactants on falling-film absorption in a two-pressure experimental facility. This chapter also discusses the effect of surfactants on other components in the system and overall system performance.
- Chapter 6 presents a comparative assessment between surfactant-enhanced falling-film and bubble absorption modes in terms of possible heat and mass transfer rates within similar envelopes.

- Chapter 7 summarizes the important conclusions of this study and provides recommendations for future work in this area.

CHAPTER 2. SURFACTANT SELECTION AND MODELING FRAMEWORK

The development of a surfactant selection criterion based on enhancement mechanisms and the value of surface tension is described here. A preliminary modeling framework is developed to study the effect of surfactants on the performance of absorbers¹.

2.1 Introduction

The significance of Marangoni convection on heat and mass transfer processes has been highlighted in many investigations (Sternling and Scriven, 1959; Nekoeian et al., 2019). Artificially induced Marangoni convection by the addition of low surface tension fluid at the gas-liquid interface effectively enhances the rate of mass transfer across the interface (Smigelschi et al., 1969). The determination of the degree of enhancement is important in many applications, including gas-liquid absorption and desorption (Brian et al., 1971), liquid-liquid extraction (Orell and Westwater, 1962), and distillation (Proctor et al., 1998). Thermally driven vapor absorption systems have received increased interest in recent years as viable alternatives to vapor compression systems (Xu and Wang, 2016). Absorption systems that employ ammonia-water as the working fluid have many advantages, including the ability to operate over a wide range of conditions, and compact system footprint due to the low specific volume of ammonia vapor and the use of microscale geometries (Determan and Garimella, 2012; Garimella et al., 2016; Kini et al.,

¹ This chapter is adapted from: Kini, G., Garimella, S., Passive enhancement of ammonia-water absorption by the addition of surfactants, *International Journal of Heat and Mass Transfer* (2021), DOI: <https://doi.org/10.1016/j.ijheatmasstransfer.2021.121478>

2020). The absorber is considered as the key component in absorption systems due to the complex coupled heat and mass transfer processes that occur within, and the typically low driving temperature differences. The overall performance of absorption systems is typically limited by the performance of the absorber (Goyal et al., 2017; Hoysall and Garimella, 2019). The use of passive enhancement techniques that achieve higher absorption rates is critical, as they enable compact absorber sizes, and/or lower cycle driving temperatures in solar or waste-heat driven applications (Amaris et al., 2018). Passive enhancement techniques include the use of rough or extended surfaces or the inclusion of small quantities of additives to the working fluid.

The addition of surfactants to the working fluid leads to increased interfacial turbulence and better absorption. The interfacial turbulence is induced by surface tension gradients, also known as the Marangoni effect. One of the early investigators to report this enhancement by surfactants was Kashiwagi (1988). Surfactants have been widely used in water-LiBr absorption systems, while there are only a handful of studies that consider surfactants in ammonia-water systems. Although the physics of absorption enhancement due to surfactants has been discussed since their introduction in the 1980s, the details of the mechanisms responsible for the enhancement need further clarity (Kyung and Herold, 2001).

Hoffmann et al. (1996) investigated the effect of surfactants on a horizontal falling-film water-LiBr absorber and suggested that the improvement in performance was due to the combined effect of surface tension reduction and change in droplet characteristics. Kulankara and Herold (2000) studied the effect of surfactants on falling-films over vertical tubes, and developed the “vapor surfactant” theory. Beutler et al. (1996) concluded that 2-

ethyl-1-hexanol (2E1H) provided the best enhancement based on experimental evidence from three enhancement additives. Miller (1999) studied the combined effect of advanced surfaces and additives in a water-LiBr falling-film absorber and concluded that additives are more effective than surface modifications. Fu Lin and Shigang (2011) investigated enhancement of absorption in a vertical falling-film water-LiBr absorber and observed the mass transfer coefficient improve for various operating conditions. Zhang et al. (2019) compared the enhancement due to surface modification and surfactants and inferred that the effect of surfactant on heat and mass transfer is greater than that of tube surface geometry. Olbricht et al. (2018) and Giannetti et al. (2018) presented numerical models for falling-film water-LiBr absorbers with surfactants. Marangoni convection leads to internal mixing and continuous renovation of the interfacial conditions, thereby intensifying mass transfer at the interface (Giannetti et al., 2018). Möller and Knoche (1996) were the first to conduct experiments on the ammonia-water working fluid and concluded that 50 parts per million (PPM) of 1-octanol resulted in the best enhancement in a bubble absorber. Kang et al. (1999b) and Kim et al. (2006) visually investigated the effect of surfactants and confirmed that Marangoni convection played a role in the enhancement of performance. Kim et al. (2007b) show a five-fold enhancement in ammonia-water bubble absorbers by adding a combination of copper nanoparticles and surfactants. Hoysall and Garimella (2019) investigated ammonia-water absorption in microchannels and attributed the improvements in absorption by the addition of surfactants to improved flow distribution and Marangoni convection.

While the above studies demonstrated an enhancement in absorption by the addition of surfactants, the work of Beutler et al. (1996) highlighted that the reduction in surface

tension cannot be the only reason for enhancement. They observed that the addition of 1-decanol reduced surface tension, but did not enhance performance. Similar observations were reported by Möller and Knoche (1996) for anionic-tenside Marlon PS which caused a reduction in surface tension without demonstrating enhancement. These results underscore the importance of understanding the mechanism of enhancement beyond just the reduction of surface tension.

Figure 2.1 provides a summary of the enhancements observed in the literature where surfactant enhancement ratio is calculated as the ratio of mass absorbed with additives to the mass absorbed in the absence of additives. The surfactant concentration ranged from 5 PPM (Kim et al., 1996) to 1000 PPM (Kim et al., 2006). While additives can cause enhancement in absorption by up to 4 times, the lack of understanding of the underlying phenomena has prevented the development of surfactant enhanced ammonia-water absorption systems. In addition, the magnitude of enhancement is significantly dependent on the conditions of the working fluid (Amaris et al., 2018). It must also be noted that many of these studies are performed with non-representative geometries such as stagnant liquid pools and operating conditions. For instance, major enhancements in mass transfer were obtained for low solution flow rates, absence of a coupling fluid stream and at low ammonia concentrations. However, the benefits in heat and mass transfer by these passive enhancement techniques might be reduced at higher flow rates, resulting in different flow regimes, or at higher solution concentrations.

In this chapter, the enhancement in ammonia-water absorption by the addition of surfactants (1-octanol; 2-ethyl-1-hexanol; 1-decanol and sodium dodecyl sulfate) is studied. A surfactant selection criterion that considers the enhancement mechanism in

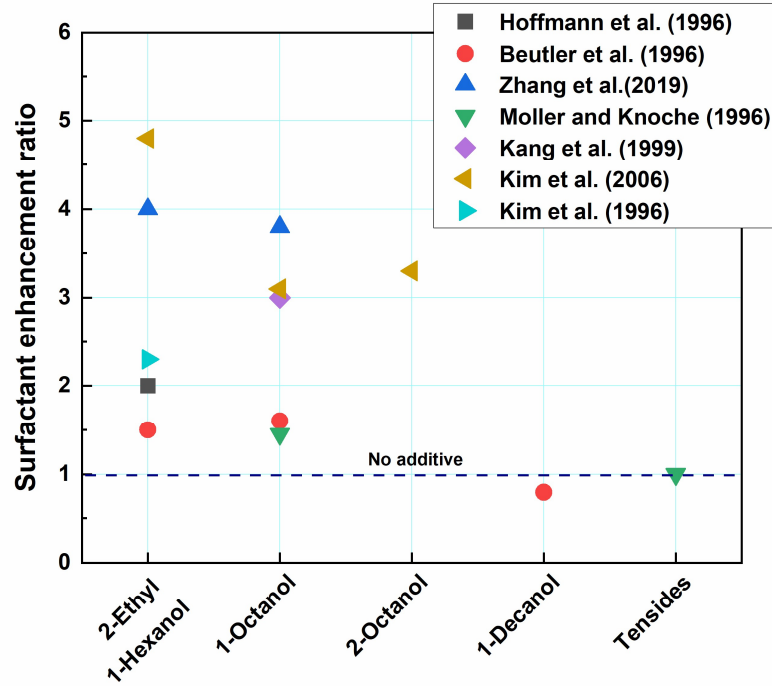


Figure 2.1: Summary of the literature

addition to the magnitude of surface tension reduction is developed. A screening analysis is performed to identify the best surfactant and the ideal concentration. A coupled heat and mass transfer model is developed to understand the impact of adding surfactants on ammonia-water absorption in a falling-film absorber. A representative geometry and conditions from an absorber operating in a 10.5 kW cooling capacity absorption heat pump are used (Kini et al., 2020). The enhancement in overall absorber performance is demonstrated by the increase in overall conductance of the heat and mass exchanger.

2.2 Surfactant selection criterion

The surface tension of a typical fluid decreases with increasing concentration of added surfactants and reaches a plateau value as shown schematically in Figure 2.2. The

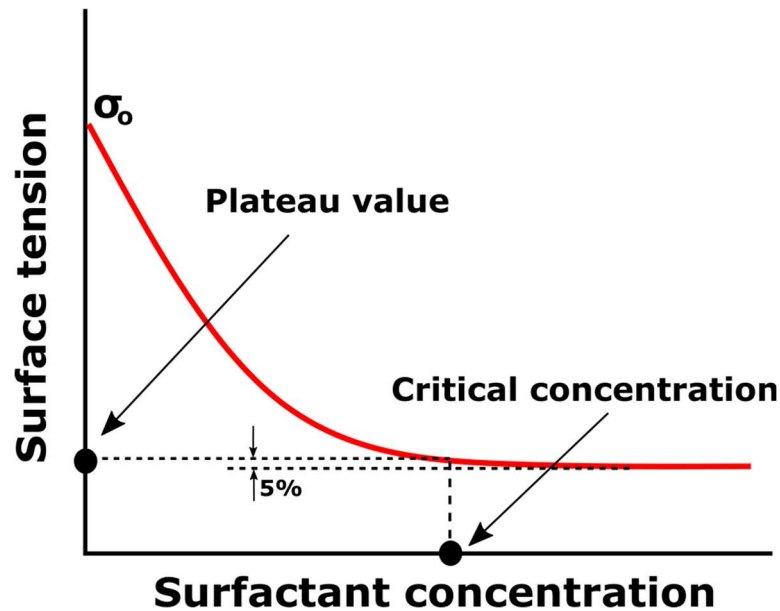


Figure 2.2: Surface tension of fluid with added surfactant

amount of surfactant required to reduce the surface tension to within 5% of the plateau value is known as the critical concentration of the surfactant (Kim et al., 2006). A low plateau value of surface tension is useful to create a larger surface tension gradient to drive Marangoni convection. A low value of critical concentration ensures that the thermophysical properties of the base fluid such as density, viscosity and specific heat remain essentially unaltered.

Conventional mass transfer theories, such as film theory, penetration theory, and the surface renewal theory, do not consider the effects of surface tension on mass transfer (Wu et al., 2001). Smigelschi et al. (1969) and Ruckenstein et al. (1970) added iso-butanol to the air-water interface and observed an increase in the efficiency of CO₂ absorption. They related this to an increase in the mass transfer coefficients due to the artificially induced surface flow at the interface. Smigelschi et al. (1969) also adopted the convection-

diffusion equations to discuss the velocity field due to the surface flow and showed that the analytical solution is consistent with experimental observations. Golovin (1992) presented a semi-empirical model of mass transfer accompanied by interfacial turbulence and showed that the mass transfer coefficient is linearly dependent on the driving force under interfacial turbulence conditions. Lu et al. (1996) investigated artificially induced Marangoni convection by continuously dissolving aqueous binary mixtures of *n*-alcohols (methanol, ethanol, and *n*-propanol) at a water surface for absorption of CO₂. They developed a correlation for mass transfer coefficient using the experimental data ($Sh = 0.74Ma^{0.35}Sc^{-0.35}\tilde{Sc}^{0.5}$), where Sc and \tilde{Sc} are the Schmidt numbers of the alcohol and gas being absorbed, respectively. Their results showed that mass transfer rates with artificially induced Marangoni convection can be as much as 3-4 times larger than those without it. They extended the study to include aqueous solutions of Sodium Dodecyl Sulphate (SDS), Triton X-100, and alcohols with higher number of carbon atoms, and observed that adding surface-active agents does not always induce interfacial turbulence (Lu et al., 1997). They observed that there is a critical Marangoni number (Ma_{cr}) below which interfacial turbulence is not induced. The Marangoni number is the ratio of mass transport caused by surface tension gradient to that caused by diffusion (Eq. (2.1)).

$$Ma = \frac{\Delta\sigma L}{\mu D} \quad (2.1)$$

Based on experimental results, Imaishi et al. (1980) suggested the use of an empirical correlation of the form $R = \left(\frac{Ma}{Ma_{cr}} \right)^n$ to predict the mass transfer enhancement, where R is

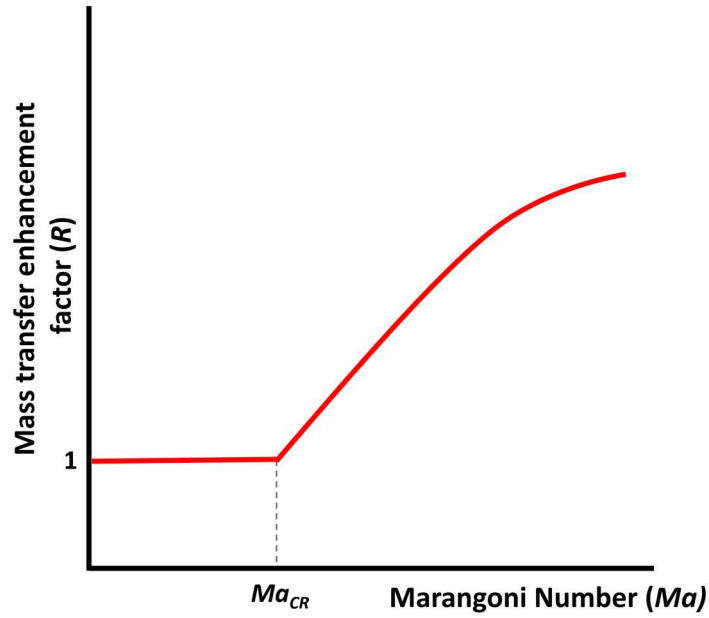


Figure 2.3: Mass transfer dependency on Marangoni number

the enhancement factor (Figure 2.3). Sun et al. (2002) showed that $n = 0.5$ best fits the experimental data.

Therefore, the chosen surfactant must have a low plateau value of surface tension, low critical concentration, and Ma greater than the critical value to initiate interfacial turbulence. The critical Ma can be calculated using the method of Semkov and Kolev (1991).

2.3 Surface tension measurements

2.3.1 Experimental method

Force and optical-based methods are most commonly used to measure surface and interfacial tension (Kini and Garimella, 2019). Force-based methods rely on the

measurement of forces exerted on a probe that is positioned at the gas-liquid or liquid-liquid interface. The forces measured by the balance as the probe interacts with the surface of the liquid are used to calculate surface tension. The Du-Nouy ring and Wilhelmy plate methods are examples of force tensiometry. Surfactant-based solutions, however, pose a challenge. The use of the ring method, where the interface is stretched during measurements means that the equilibrium state is not achieved, because new surface area for surfactants to move to is constantly created. The measured surface tension values are higher than the actual value. On the other hand, the equilibrium state can be achieved with the Wilhelmy plate method as the plate can be kept stationary. However, the change in the wettability of the plate due to unwanted adsorption of surfactants can confound the measured values. It is for these reasons that the pendant drop optical technique is best suited for surfactant-based solutions (Lauren, 2017). It must also be ensured that the needle tip does not influence the drop shape. For the present study, the Dataphysics OCA 25 goniometer with drop shape analysis capability is used (Figure 2.4). The shape of the drop is governed by the Young-Laplace equation given by Eq. (2.2).

$$\Delta P_t = \Delta P_0 \pm \Delta \rho g z = \sigma \left(\frac{1}{r_1} + \frac{1}{r_2} \right) \quad (2.2)$$

It is determined by the combination of surface tension force that tends to create a spherical drop and gravitational forces that stretch the drop, leading to the typical pear or pendant shaped drop. The shape of the drop is extracted by image analysis and the method elucidated by Stauffer (1965) is used to calculate the value of surface tension. Four different surfactants are investigated in this study: 1-octanol; 2-ethyl-1-hexanol; 1-decanol and sodium dodecyl sulfate (SDS). The experimental conditions are summarized in Table 2.1.

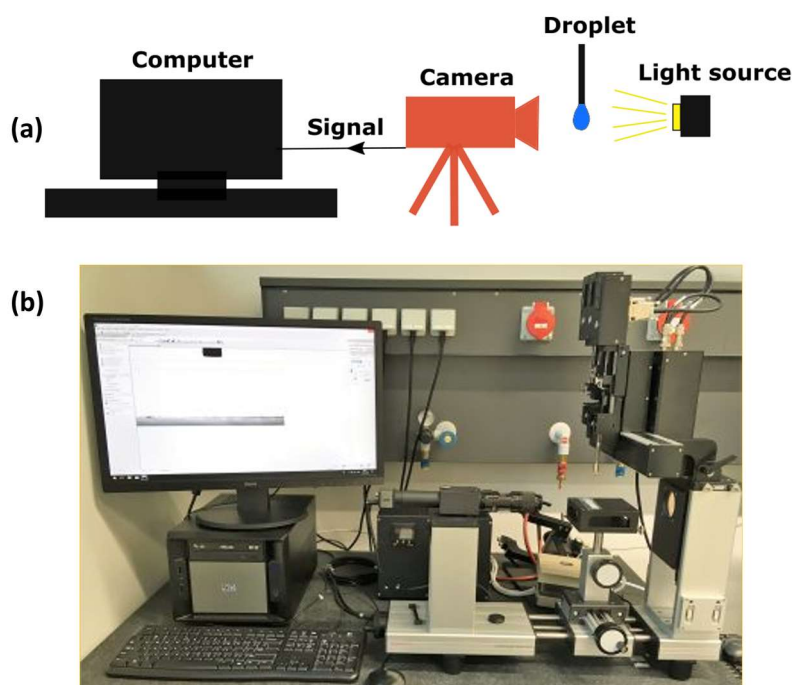


Figure 2.4: Experimental facility (a) schematic (b) photograph

2.3.2 Surface tension measurements

Surface tension measurements with additives are made for water and ammonia-water solutions with various ammonia concentrations. The shape of the drop analyzed using the Dataphysics SCA 22 module is shown for two cases in Figure 2.5. On the left is a drop of pure water with no surfactant, while on the right is a drop with 1000 PPM of 1-octanol. It is observed that with the addition of surfactants, the size of the drop decreases, and it assumes a stretched oval shape. The drop on the left corresponds to surface tension of 0.072 N m^{-1} , while the drop on the right corresponds to 0.028 N m^{-1} . The surface tension values obtained from this method are validated by values reported in the literature for pure water and 15% ammonia-water solution.

Table 2.1: Summary of experimental conditions

Base solution	Ammonia-water solution
Concentration of ammonia (x)	0%; 15%; 28% (percentage of ammonia)
Surfactant	1-octanol; 2-ethyl-1-hexanol; 1-decanol and sodium dodecyl sulfate
Concentration of surfactant (C)	0; 100; 200; 500; 1000 (PPM of surfactant)
Ambient temperature	23 °C
Needle	24 gauge
Dosing volume	$\sim 50 \mu\text{L}$
Instrument uncertainty	10^{-3} Nm^{-1}



Figure 2.5: Droplet with 1-octanol 0 PPM (left) 1000 PPM (right)

Figure 2.6 shows the variation of surface tension of ammonia-water solution with the addition of 1-octanol. As little as 100 PPM of the additive causes a 30% change in surface tension. It is also seen that 500 PPM is the critical concentration of the 1-octanol, beyond which there is no appreciable reduction in surface tension. At surfactant concentrations above the critical concentration, surfactant molecules tend to cluster together, and form structures known as micelles (Tanford, 1974). Figure 2.7 shows measured surface tension values for various surfactants in 15% ammonia-water solution. A critical concentration of about 500 PPM is again observed for all the hydrocarbon alcohols, which have very low solubility in the solution. The plateau value of surface tension for 1-decanol is $33.4 \times 10^{-3} \text{ N m}^{-1}$, while the values for 1-octanol and 2-ethyl-1-hexanol are slightly lower than $28 \times 10^{-3} \text{ N m}^{-1}$. Sodium dodecyl sulfate performs poorly in comparison, reducing the surface tension only to $40.2 \times 10^{-3} \text{ N m}^{-1}$. It is also observed that the slope of surface tension reduction plot $\left(\frac{\partial\sigma}{\partial C}\right)$ is higher for 1-octanol and 2-ethyl-1-hexanol, leading to much higher Ma and mass transfer enhancement factors. Lu et al. (1997) also reported that the length scale (L) used in the Marangoni number is a few orders of magnitude smaller (10^{-9}) for 1-decanol as compared to alcohols with lower number of carbon atoms (10^{-6}). The combined effect results in a Marangoni number lower than the critical Marangoni number required to initiate interfacial turbulence.

The proposed criterion highlights the finding that the reduction in surface tension is not a sufficient condition to initiate interfacial turbulence and helps to explain reports in the literature that showed no enhancement in absorption when certain surfactants were

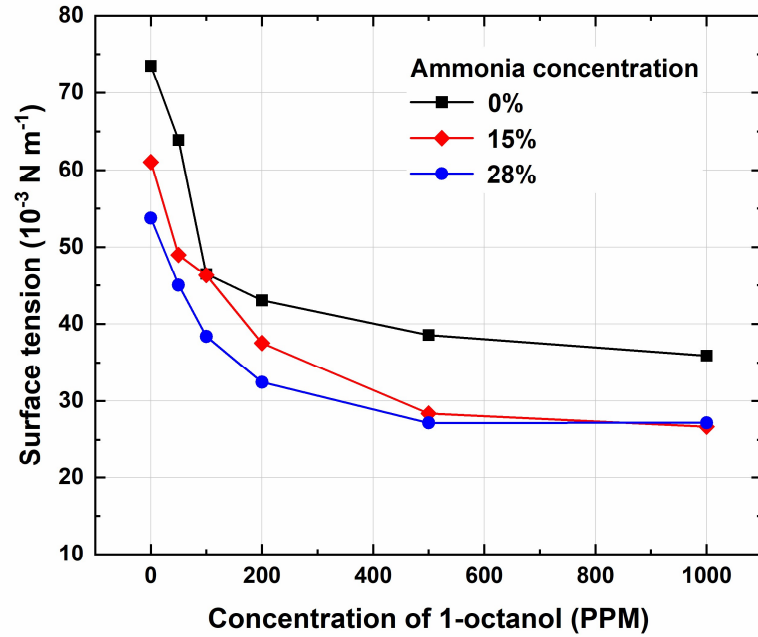


Figure 2.6: Surface tension of ammonia-water solution with 1-octanol

used. It is inferred from this study that 500 PPM of 1-octanol and 2-ethyl-1-hexanol are the preferred additives to enhance ammonia-water absorption.

2.4 Model development

A simplified model for a falling-film absorber is developed based on the framework first presented by Ruhemann (1947) and used by Raisul Islam et al. (2004), among others. The goal of this model is to demonstrate the coupled nature of heat and mass transfer in absorption and provide insights into the impact of enhancement by surfactants at a component level. The model can be extended for other coupled heat and mass transfer processes and geometries. Dilute solution falls in the form of thin films along vertical tubes through which cooling water flows in the upward direction. Ammonia vapor is absorbed into these films from all sides. The following assumptions are made

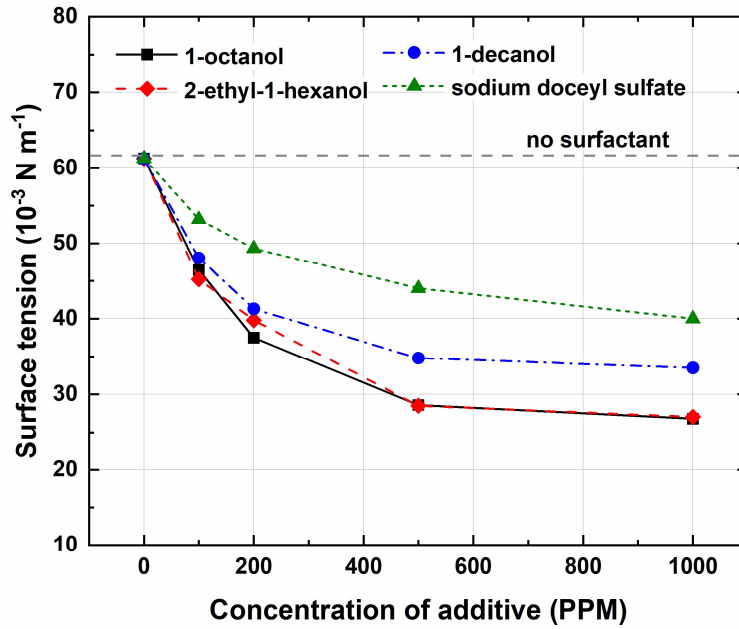


Figure 2.7: Surface tension with four additives

- (a) Ammonia vapor is pure
- (b) The heat of absorption is generated in a theoretical layer at the gas-liquid interface
- (c) The film is well mixed
- (d) The fluid temperatures are invariant in any horizontal section

A representative segment of this absorber is shown in Figure 2.8. Consider l as the length of the absorber taken positive along the downward direction. For a horizontal section of the absorber of infinitesimal length dl , we have the heat balance equation

$$d\dot{Q} = -\dot{m}_{sol} c_{p,sol} dT_{sol} + H d\dot{m}_{sol} = -\dot{m}_{cf} c_{p,cf} dT_{cf} \quad (2.3)$$

where H is the heat of absorption. If the absorber has a surface area of S per unit length and an overall heat transfer coefficient of U , the heat transfer equation can be expressed as

$$d\dot{Q} = U(T_{sol} - T_{cf}) \times S \times dl \quad (2.4)$$

The mass transfer equation is

$$dm_{sol} = \tilde{K}(P_v - P_{int}) \times S \times dl = K(C_v - C_{int}) \times S \times dl \quad (2.5)$$

where K is the mass transfer coefficient. The driving force for mass transfer is the difference in pressure of ammonia vapor and the interfacial pressure. This driving force can also be expressed in terms of a concentration difference, in which case, the mass transfer coefficient has the units of m s^{-1} .

By rearranging Eqs. (2.3) - (2.5), three differential equations for changes in m_{sol} , T_{cf} , T_{sol} along the length of the absorber are obtained.

$$\frac{dm_{sol}}{dl} = K \times S \times (C_v - C_{int}) \quad (2.6)$$

$$\frac{dT_{cf}}{dl} = -U \times S \times \left(\frac{T_{sol} - T_{cf}}{m_{cf} \times Cp_{cf}} \right) \quad (2.7)$$

$$\frac{dT_{sol}}{dl} = \frac{S}{m_{sol} c_{p,sol}} \times \left(H \times K \times (C_v - C_{int}) - U \times (T_{sol} - T_{cf}) \right) \quad (2.8)$$

The coupled nature of heat and mass transfer in ammonia absorption is shown in Eq. (2.8), where the solution temperature T_{sol} is dependent on both the heat transfer coefficient U and the mass transfer coefficient K . Based on the relative magnitudes of the two terms involved, $\frac{dT_{sol}}{dl}$ can be positive, negative or zero. Nominal values of $U = 500 \text{ W m}^{-2} \text{ K}^{-1}$ and $K = 1 \times 10^{-3} \text{ m s}^{-1}$ for a falling- film ammonia-water absorber are used (Kang

et al., 1999a). The geometric features of a shell-and-tube absorber, $S = 4 \text{ m}^2 \text{ m}^{-1}$ and length of absorber $l = 0.75 \text{ m}$ are used (Chandrasekaran et al., 2020). The inlet temperatures of dilute solution ($T_{sol} = 55^\circ\text{C}$) and cooling water ($T_{cf} = 20^\circ\text{C}$) are specified. A solution inlet mass flow rate of $\dot{m}_{sol} = 24 \times 10^{-3} \text{ kg s}^{-1}$ is used. These are representative conditions for an absorber in a 10.5 kW cooling capacity absorption heat pump (Kini et al., 2020).

The addition of surfactants enhances the mass transfer coefficient as noted from Section 2. The enhancement factor is calculated from Eqs. (2.9) and (2.10)

$$Ma = \frac{\partial \sigma}{\partial C} \frac{\Delta c L}{\mu D} \quad (2.9)$$

$$R = \left(\frac{Ma}{Ma_{cr}} \right)^{0.5} \quad (2.10)$$

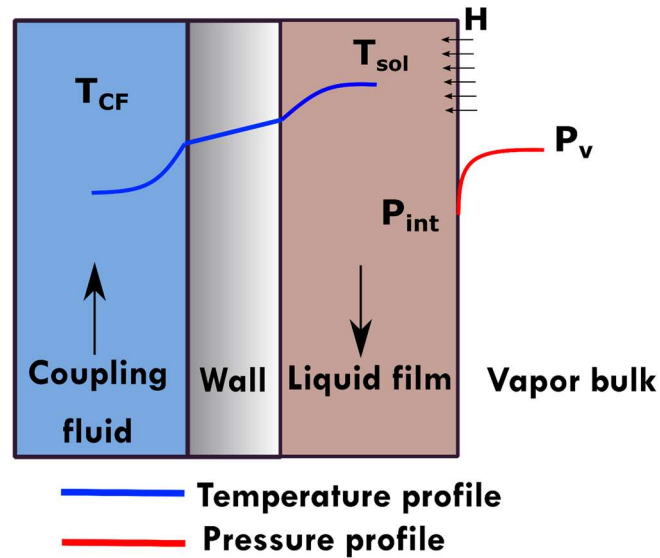


Figure 2.8: Representative segment of the falling-film absorber

It is established from the results of Section 3 that 500 PPM of 1-octanol is the preferred additive. The results from the surface tension measurements are used to calculate the surface tension reduction gradient $\left(\frac{\partial\sigma}{\partial C}\right)$. The diffusivity D is calculated using the Wilke and Chang (1955) equation. The length scale in artificially induced interfacial turbulence is adapted from Lu et al. (1996). A critical Ma of 2500 as proposed by Lu et al. (1997) is used to determine the initiation of interfacial turbulence in falling-films. The mass transfer coefficient in the presence of 1-octanol is given by

$$K_{surf} = K \times R \quad (2.11)$$

It must be noted that when the Ma corresponding to the driving concentration is lower than the critical Ma , the mass transfer coefficient is equal to that of purely diffusive mass transfer.

In addition to mass transfer intensification, the reduction of surface tension of the fluid enhances wettability. Falling-film absorbers are typically limited by the incomplete use of heat and mass transfer areas due to poor wetting (Triché et al., 2017; Bohra et al., 2019). The reduction of surface tension of the bulk fluid by the addition of surfactants can improve wettability and alleviate this concern. Kang et al. (2007) experimentally investigated the flow characteristics of a falling-film in the presence of surfactants. They inferred that the wetted area of the falling-film increased as the surfactant concentration increased. To account for this effect, an area enhancement factor F is used.

$$S_{surf} = S \times F \quad (2.12)$$

2.5 Results

2.5.1 Temperature and concentration profiles

The three coupled differential equations that govern the solution temperature, coupling fluid temperature, and solution mass flow rate in a falling-film ammonia-water absorber are solved along the length of the absorber. The variation of these quantities in the absence of any additive is shown in Figure 2.9. Dilute solution enters the top of the absorber at 55°C at a solution flow rate of 0.024 kg s⁻¹ and concentration of 0.295. As the solution flows downward, it absorbs ammonia, thereby increasing the flow rate and generating heat that is rejected to the coupling fluid, which enters the bottom at 20°C and leaves at 28°C. The concentrated solution leaves the absorber at 35°C with a concentration of 0.42 after absorbing 0.0047 kg s⁻¹ of ammonia.

For the same inlet conditions of $T_{sol} = 55^\circ\text{C}$, $T_{cf} = 20^\circ\text{C}$ and $\dot{m}_{sol} = 0.024 \text{ kg s}^{-1}$, the addition of 500 PPM of 1-octanol results in significantly different temperature and flow rate profiles (Figure 2.10). The reduction of surface tension by the additive leads to interfacial turbulence at the gas-liquid interface and enhances the mass transfer coefficient. The Ma number corresponding to 500 PPM of 1-octanol results in an enhancement factor $R = 3.1$. In addition, to account for the increased wettability, an area enhancement factor $F = 1.35$ is used (Kang et al., 2007). Due to the increase in mass transfer coefficient K , from Eq. (2.6), it is seen that $\frac{d\dot{m}_{sol}}{dl}$ is large compared to the case without surfactants, resulting in better absorption. The large value of mass transfer coefficient K also leads to a positive value for $\frac{dT_{sol}}{dl}$ as $HK(C_v - C_{int}) > U(T_{sol} - T_{cf})$ in the first few segments at the top of the

absorber. This leads to an increase in the temperature of the solution which continues until the interface concentration C_{int} increases such that the product $HK(C_v - C_{\text{int}}) < U(T_{\text{sol}} - T_{\text{cf}})$. The concentration profiles along the length of the absorber are shown in Figure 2.11. In this case, the concentrated solution leaves the absorber at 38°C with a concentration of 0.46 after absorbing 0.007 kg s^{-1} of ammonia. The coupling fluid enters and exits the absorber at 20°C and 31°C, respectively.

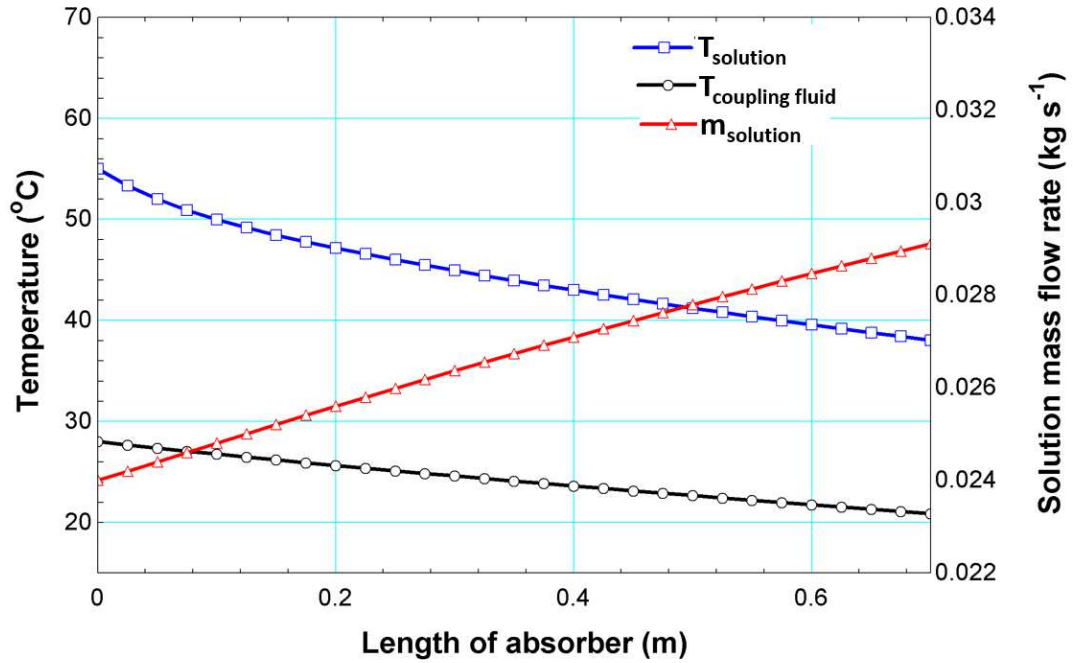


Figure 2.9: Results for absorber without surfactant

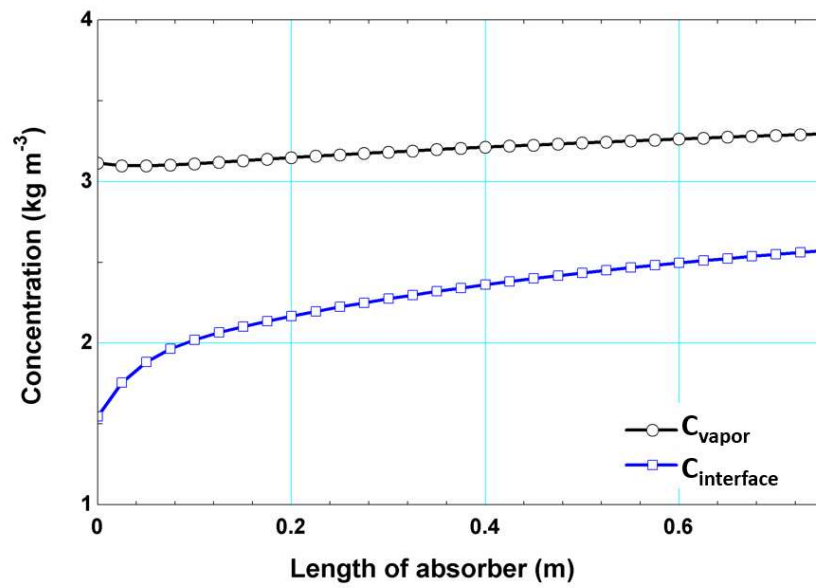
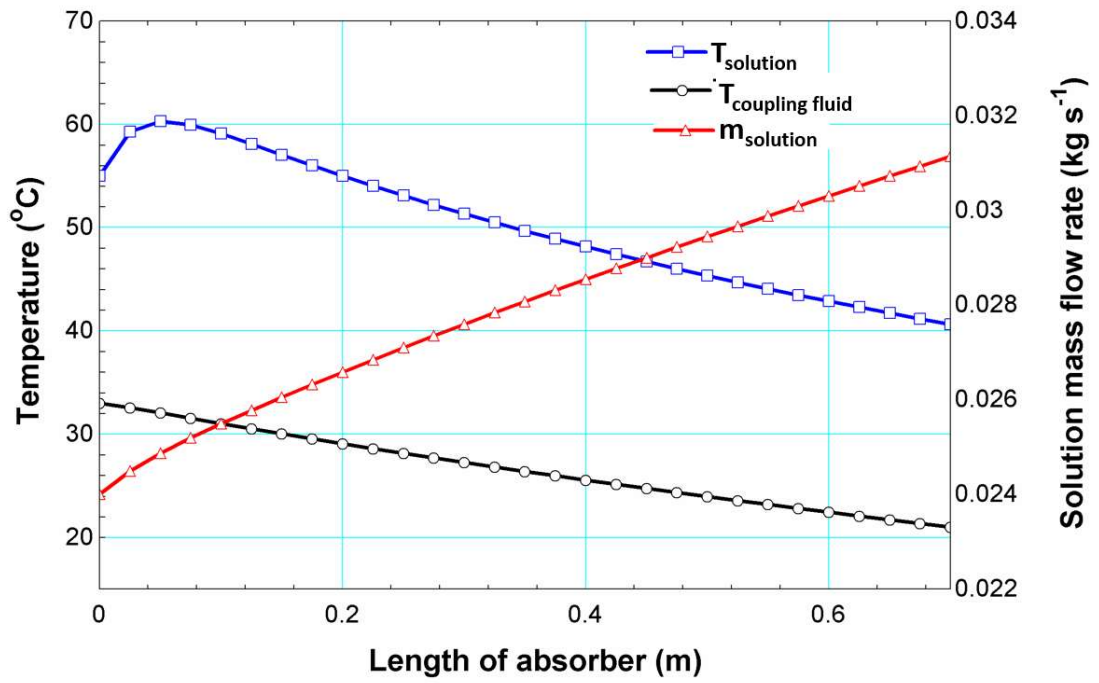


Figure 2.11: Concentration profile in absorber with 500 PPM of 1-octanol

2.5.2 Component performance

The performance of the absorber with and without surfactants can be compared using the overall conductance UA of the absorber. The UA highlights the overall enhancement at the component level rather than focusing on the individual enhancements in mass transfer coefficients or the surface area available for transport processes. This is useful especially in the case of coupled heat and mass transfer processes such as ammonia-water absorption. The UA can be calculated from the temperatures of both the fluid streams and heat duty of the absorber as shown in Eqs. (2.13) - (2.15)

$$\dot{Q}_{abs} = (\dot{m}Cp)_{cf} (T_{cf,out} - T_{cf,in}) \quad (2.13)$$

$$LMTD = \frac{(T_{sol,in} - T_{cf,out}) - (T_{sol,out} - T_{cf,in})}{\ln \left[\frac{(T_{sol,in} - T_{cf,out})}{(T_{sol,out} - T_{cf,in})} \right]} \quad (2.14)$$

$$UA = \frac{\dot{Q}_{abs}}{LMTD} \quad (2.15)$$

The UA of the absorber in the absence of surfactants is 0.88 kW K^{-1} . The addition of 500 PPM of 1-octanol leads to an increase in UA by 33% to 1.17 kW K^{-1} . This is an important result, as it highlights the impact of adding surfactants to passively enhance absorption performance of a heat and mass exchanger. The overall increase in UA is composed of contributions from enhanced mass transfer and improved wetting. The individual contributions are assessed by switching on the enhancement factors R and F , independently. It is observed that the increase in the mass transfer coefficient contributes

to 24% enhancement in UA , while the remaining 9% can be attributed to the increase in surface area.

To underscore the importance of the operating conditions and geometry when studying these enhancements, the above exercise was repeated by assuming a higher mass transfer coefficient $K = 3 \times 10^{-3} \text{ m s}^{-1}$ in the absence of surfactants. This represents a case where the absorber geometry is modified, or a new design configuration is chosen to achieve lower mass transfer resistance. In this scenario, the addition of surfactants results in a UA increase of 26%, highlighting that the effect of surfactants is intricately dependent on the geometry and conditions of the working fluid. The passive enhancement will be less effective if the dominant resistance is on the coupling fluid side like in the cases of Garrabrant and Christensen (1997) and Goel and Goswami (2005)

The results from this study indicate that ~30% reduction in area can be achieved when designing heat and mass exchangers that operate in the presence of surfactants. The enhancement in performance advances the development of compact absorbers and absorption heat pumps. The results from this work can be used to guide heat and mass transfer process intensification in a variety of applications including condensation, boiling, desorption, extraction, and distillation.

2.6 Conclusions

Passive enhancement of ammonia-water absorption by the addition of surface-active agents is investigated. The mechanism of enhancement due to interfacial turbulence at the gas-liquid interface is discussed. A surfactant selection criterion is developed based on the plateau value of surface tension, critical concentration, and the critical Marangoni number

required to initiate interfacial turbulence. A systematic screening analysis is presented, and the ideal surfactants and their concentrations for the enhancement of ammonia-water absorption are recommended. It is determined that 500 PPM of 1-octanol or 2-ethyl-1-hexanol are the preferred additives. The selection criterion highlights the finding that the enhancement in mass transfer is not solely dependent on the reduction in surface tension of the bulk fluid and successfully explains several anomalies reported in the literature.

A coupled heat and mass transfer model is developed to predict the performance of a falling-film absorber at conditions representative of an absorber operating in a 10.5 kW absorption heat pump. The model accounts for enhancement in mass transfer coefficients and an increase in surface area due to the addition of surfactants. The overall conductance of the absorber increases by ~30% in the presence of 500 PPM of 1-octanol. The results indicate that coupled heat and mass transfer processes that involve interfacial interactions can be passively enhanced by the addition of surfactants.

CHAPTER 3. TWO-PHASE FLOW IN THE PRESENCE OF SURFACTANTS

This chapter investigates the effects of surfactants on the characteristics of two-phase flow in a geometry representative of a bubble absorber. Flow visualization and image processing are used to quantify the impact of surfactants. The mechanisms that lead to heat and mass transfer enhancement are discussed.

3.1 Introduction

Two-phase flows are encountered in many industrial and environmental processes, including chemical reactors and heat exchangers. Specifically, two-phase flow in vertical pipes is of importance to many industrial processes (Ghiaasiaan, 2007). The respective flow regimes can strongly influence the pressure drop, holdup, system stability, and heat, mass, and momentum transfer rates. Surface-active agents or surfactants are amphiphilic molecules that adsorb onto the interface between two fluids and reduce the surface tension. Surfactants are used to create emulsions, as wetting agents and as foaming agents in industrial processes (Farn, 2008). The addition of surfactants to two-phase flows can cause dramatic changes to the flow structure through multiscale effects (Takagi and Matsumoto, 2011). The surfactant adsorbs onto the interface and changes the interfacial dynamics, which then affects heat and mass transfer.

Griffith (1962) investigated the impact of surfactants on the terminal velocity of bubbles and drops and showed that the terminal velocity at small Reynolds numbers is related to the cap size and surfactant concentration. Rozenblit et al. (2006) studied flow

patterns in vertical upward air-water flow experimentally in a 0.025 m diameter tube in the presence of counter-ion sodium salicylate (CTAC) as surfactant. They reported visual observations of smaller gas bubbles, but larger in number in the presence of CTAC. They also concluded that the flow regime transitions in the presence of surfactants are consistent with the flow regime map presented by Taitel et al. (1980). They used a two-phase mixer with porous layers at the entrance of the tube. Specifically, in slug flow conditions, bullet-shaped Taylor bubbles are separated with liquid slugs containing small gas bubbles. In the case with surfactants, these bubbles were observed to be much smaller in size and larger in number.

Duangprasert et al. (2008) studied the effects of adding various concentrations of SDS on the flow regimes, bubble sizes, and velocities in upward two-phase flow. The experiments were conducted for superficial air and water velocities ranging from 0.0026-50 m s⁻¹ and 0-0.123 m s⁻¹, respectively. They reported a shift in bubble-slug flow transition at much lower air flow rates in the presence of surfactants. However, no such changes were observed for churn and annular flow regimes. A significant reduction in pressure gradient was observed with the addition of SDS in slug-churn and churn flow regimes, indicating turbulent drag reduction at higher Re. Liu et al. (2014) investigated liquid holdup reduction, pressure drop reduction and drag reduction in a 0.04-m diameter plexiglass tube with commercial surfactant HY-3. Conditions relevant to gas wells that are typically at higher gas-liquid ratios were studied. Consistent with the literature, they concluded that the surfactant does not affect flow transitions but led to liquid holdup reduction and drag reduction. Van Nimwegen et al. (2015) studied churn and annular flow in 0.05-m diameter tubes at conditions relevant to oil wells. They reported changes to the interfacial

morphology that suppress the formation and entrainment of large liquid droplets in addition to observing large agitation of the liquid. They also studied flow in inclined pipes and concluded that surfactants are more effective at larger inclinations and lower liquid flow rates (Van Nimwegen et al., 2016). The addition of surfactants in large diameter tubes (> 0.04 m) can attenuate flow fluctuations, as observed in the temporal pressure data of Amani et al. (2020).

One of the governing factors in microscale two-phase flow is surface tension (Kandlikar, 2006). Therefore, it is of great importance to understand two-phase flow in microchannels and minichannels with surfactants. English and Kandlikar (2006) experimentally investigated flow in 0.001-m minichannels in the presence of Triton DF-12 surfactant at low mass fluxes ($G < 50 \text{ kg m}^{-2}\text{s}^{-1}$). While the surfactant enhanced wetting in the channel and consistently produced only annular flow, there was no quantifiable difference in pressure drop by using surfactants. Kurimoto et al. (2019) investigated slug flow in 500- μm diameter microchannels in the presence of Triton X-100. They reported that the surfactants deformed bubble rear shapes without affecting the front shapes.

It is observed from the literature discussed above that there are a handful of studies that investigate two-phase flow with surfactants. All of these studies use a two-phase mixer at the inlet of the test section and are typically performed at flow conditions relevant to oil wells. However, there are many flow systems in which dispersed bubbles flow through single orifice tubes into a liquid stream (Kuo and Wallis, 1988). This is especially relevant to bubble absorbers for ammonia-water absorption heat pumps (Cerezo et al., 2009; Amaris et al., 2018). In addition, Lioumbas et al. (2006) investigated two-phase flow patterns with surfactants and inferred that flow patterns depended on surfactant chemical structure in

addition to surface tension values. Chapter 2 presented a screening of surfactants for ammonia-water absorption and concluded that 500 PPM of 1-octanol is the preferred additive. It is also to be noted that there are no studies in the literature that investigate the effect of surfactants on interfacial area. Interfacial area plays a critical role in determining heat and mass transfer in two-phase flows. Based on the above discussion, two-phase flow through a single orifice tube is considered in the present study in the presence of 1-octanol at conditions relevant to an ammonia-water bubble absorber. The diameters, interfacial area, and velocities of bubbles and slugs are quantitatively investigated using computer vision techniques.

3.2 Test matrix

One of the key components of vapor absorption systems is the absorber where the refrigerant vapor mixes with the absorbent in a coupled heat and mass transfer process. The two most commonly used geometric configurations for absorbers are falling-film absorbers (Chandrasekaran et al., 2020) and bubble absorbers (Lee et al., 2002; Donnellan et al., 2014). Kang et al. (2000) compared the falling-film and bubble modes of absorption and found that absorption rates in the bubble mode are higher, resulting in compact absorbers. Depending on the mass flow rates of the refrigerant vapor and absorbent solution, different flow regimes are observed. In upward flow, the most commonly observed flow regimes are shown in Figure 3.1. The flow regimes that are of interest to bubble absorbers can be identified by using a flow regime map. In this study, the flow regime map of Taitel et al. (1980) is used because it has been shown in the literature that two-phase flow transitions in the presence of surfactants are consistent with it (Rozenblit et al., 2006).

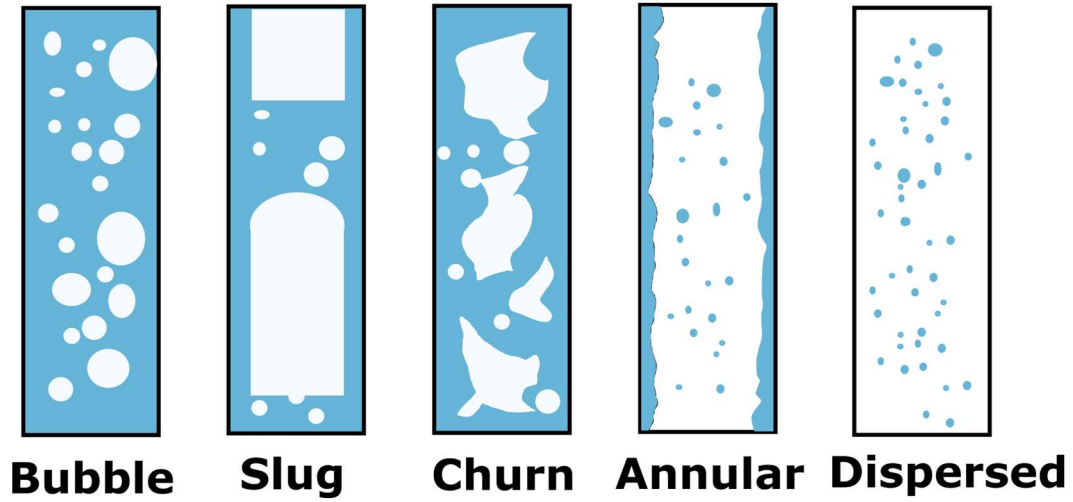


Figure 3.1: Flow regimes in upward flow

The relationship between the refrigerant and absorbent solution flow rates is determined by studying the variation of circulation ratio. Circulation ratio is an important control parameter in absorption systems and is defined as shown in Eq. (3.1)

$$CR = \frac{\dot{m}_{abs,sol} + \dot{m}_{ref}}{\dot{m}_{ref}} \quad (3.1)$$

A thermodynamic cycle model for a 10.5 kW cooling capacity absorption heat pump was developed as shown in Kini et al. (2020). The model was used to study the range of variation of the circulation ratio. Figure 3.2 shows that the circulation ratio ranges between 2 – 4.5 in the operation of a typical absorption heat pump. A design constraint in bubble absorbers is to maintain the absorbent flow rate such that the Reynolds number (Re_L) remains below 400 to allow for sufficient residence time for the absorption of vapor to be

completed (Cerezo et al., 2009). Using the Re constraint and circulation ratio range, the flow regimes found in a bubble absorber are determined (Figure 3.3). At the entrance of the absorber, the flow is expected to be in the churn/slug flow regime. Along the height of the absorber, the refrigerant gets absorbed, and the flow transitions to slug flow, and eventually to bubbly flow. In this study, the hydrodynamics of two-phase flow was studied by conducting adiabatic experiments using air and water. Air-water mixture can be used as a substitute for ammonia-water for simulating hydrodynamics because the thermophysical properties and important dimensionless numbers can be matched for the two fluid pairs (Staedter et al., 2018). Ten data points were considered, as shown in Figure 3.4, with superficial velocities ranging from $0.05 \text{ m s}^{-1} < j_l < 0.1 \text{ m s}^{-1}$ and $0.1 \text{ m s}^{-1} < j_g < 2.5 \text{ m s}^{-1}$. For each data point, experiments were performed with and without surfactants.

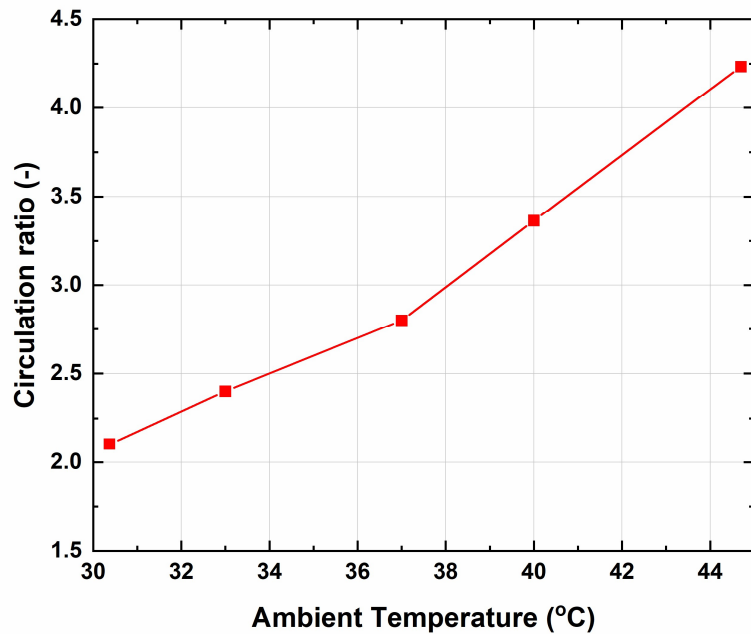


Figure 3.2: Variation of circulation ratio

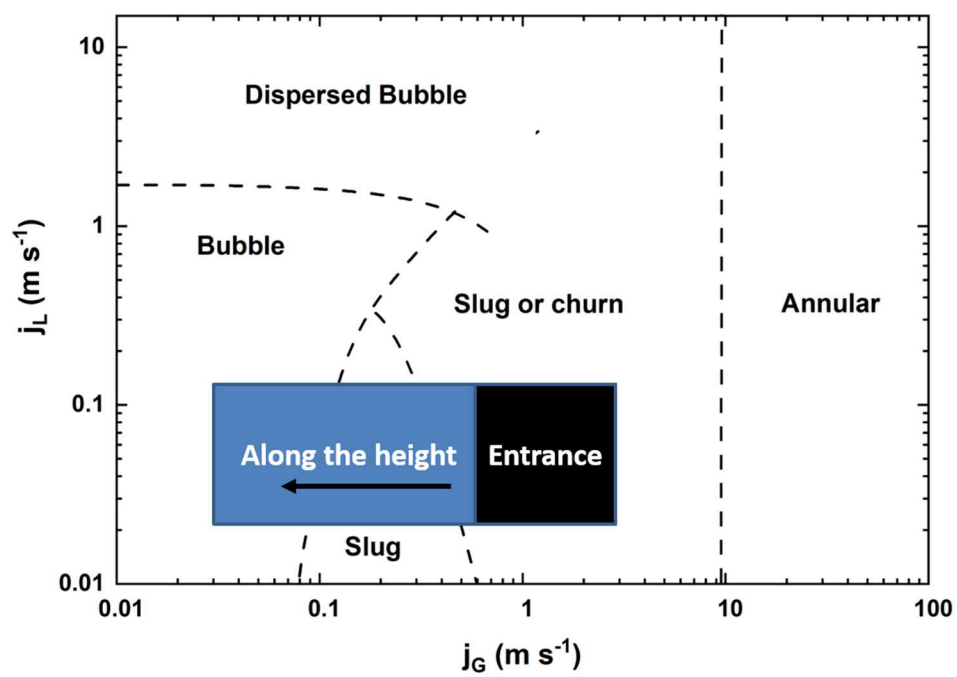


Figure 3.3: Region of interest for bubble absorbers

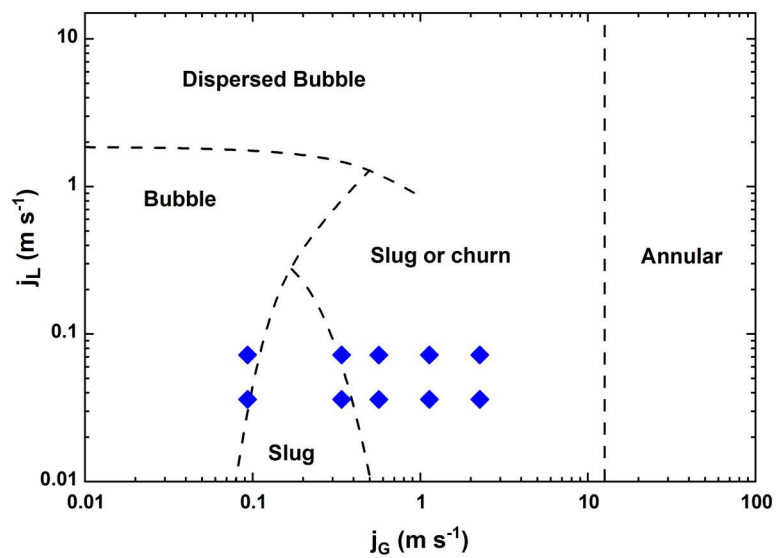


Figure 3.4: Test matrix

3.3 Experimental Facility

A test facility for air-liquid experiments was designed and constructed to simulate the hydrodynamic behavior expected in a bubble absorber. Figure 3.5a shows the experimental facility, which uses compressed air and distilled water. A pressurized tank provides liquid flow to the test section. Vapor and liquid flow rates are controlled to target values with metering valves. Rotameters with an uncertainty of $\pm 4\%$ of full scale are used to measure the flow rates of both the streams. The test section is fabricated using plexiglass and consists of a 12.7-mm outer diameter tube and a 3.175-mm inner tube for vapor to enter (Figure 3.5b). The air and water streams enter the test section from the bottom and leave from the top. Flow visualization is conducted by recording videos at $L/D_h = 10$. A high-speed camera (Photron FASTCAM Ultima 1024 with a Nikon Micro-NIKKOR 105 mm lens) was used, and recordings were taken at 3600 frames per second with a resolution of 720×540 pixels. A recording duration of 4 s was used to appropriately capture all hydrodynamic features. Three videos were recorded for each data point.

3.4 Data analysis methodology

This section first describes the pre-processing steps for each video followed by the details of calculations for interfacial area and velocity.

3.4.1 Pre-processing

For each data point, in addition to two-phase flow videos with air and water, a calibration video with only water flow is recorded (Figure 3.7a and 3.6b). This video is used to remove noise and any background effects from the flow video. Each video is

analyzed on a frame-by-frame analysis using the MATLAB image processing toolbox (MATLAB, 2017). For each frame, the outer tube walls are located using the Laplacian of the calibration image. The pixel distance between the outer walls and the scaling due to mismatch in refractive indices are taken into account to determine the overall pixel-to-mm conversion factor as shown in Figure 3.6. Additional details for calculating the scaling factor due to refractive indices mismatch is described in Milkie (2014). Next, the difference between the flow and calibration grayscale images is calculated using the *imabsdiff* function (Figure 3.7c). The resulting image does not have any noise and shadows created by artificial lighting. The image is then converted to grayscale using the *rgb2gray* function. It is beneficial to work with grayscale images especially when there are two phases that must be distinguished.

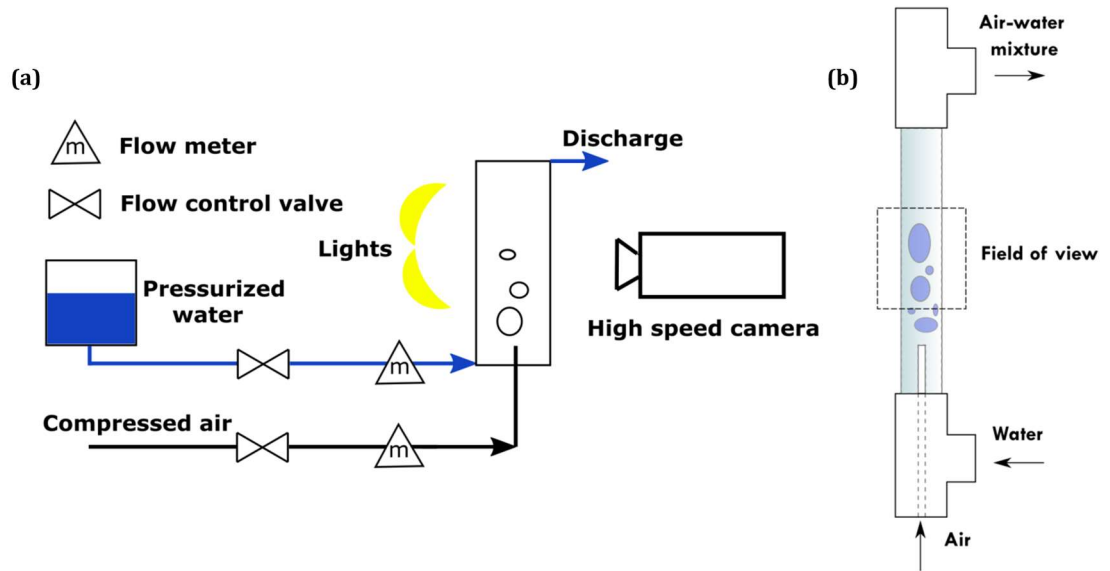


Figure 3.5: (a) Experimental facility (b) Test section

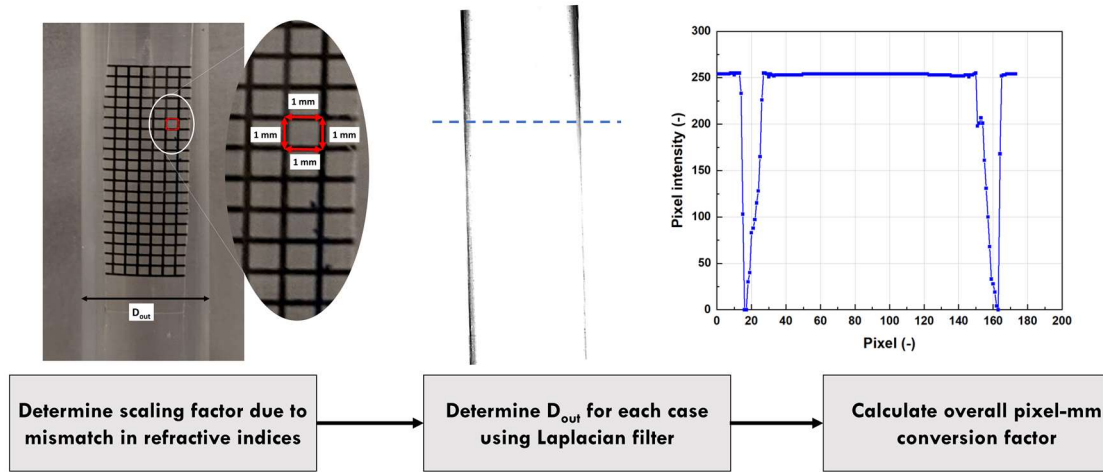


Figure 3.6: Determination of pixel-to-mm conversion

The next step is to convert the images to binary representation where liquid is represented by black pixels and air is represented by white pixels. To achieve this, the interface between the two phases should be detected using a process called image segmentation. Several edge detection techniques are available among which Canny (Hoysall et al., 2018) and Sobel (Murai et al., 2010) algorithms have been successfully applied to two-phase studies. Both the algorithms were tested in this study and it was found that the Sobel operator was consistent at detecting the interface. This results in a binary gradient mask as shown in Figure 3.7d. If the lighting conditions change between different videos, the threshold value of the Sobel operator can be accordingly changed. The binary gradient mask shows lines of high contrast in the image. These lines do not quite delineate the outline of the interface. Compared to the original image, there are gaps in the lines surrounding the object in the gradient mask. These linear gaps disappear if the Sobel image

is dilated using linear structuring elements from the *strel* function. The dilated gradient mask shows the outline of the interface correctly, but there are still holes in the interior of the air phase. These holes are filled using the *imfill* function. The resulting image where both the air and water regions have been distinguished is shown in Figure 3.7e.

3.4.2 Interfacial area

In two-phase flows, interfacial area plays a significant role in heat and mass transfer. Many two-phase flow models require accurate estimation of interfacial area to close the mathematical formulations for model solution (Wang et al., 2021). Although there are a few databases that are available for forced convective bubbly and slug flows, very few reliable data exist that cover a wide range of flow conditions and flow regimes (Ozar et al., 2012). Most studies in the literature used a four sensor conductivity probe to measure interfacial area. The probe is inserted at various radial and axial locations of the tube making it an intrusive method of measurement. In addition, the interfacial area is not directly measured and is derived using a mathematical transformation of the measured void fraction and bubble interface velocity. Some of the methods make assumptions about the shape of the bubbles and slugs to compute the interfacial area.

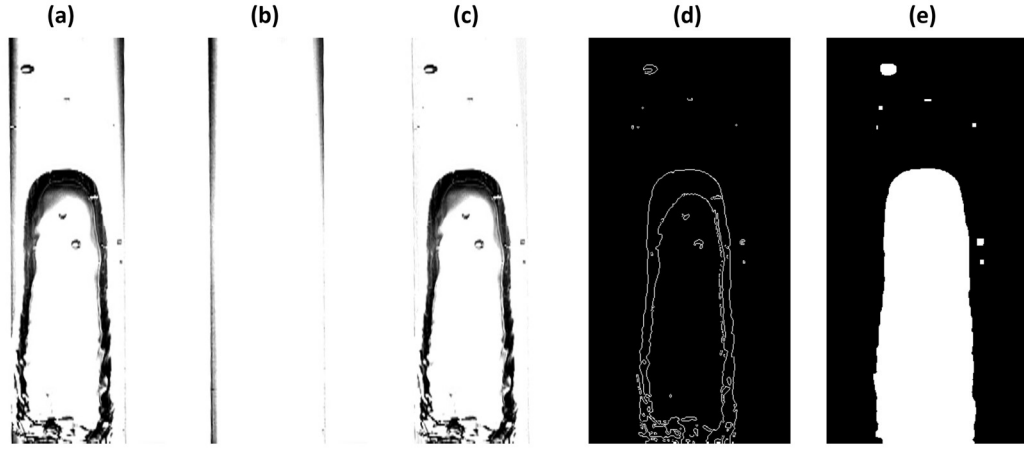


Figure 3.7: Flow visualization steps (a) flow image (b) calibration image (c) de-noised image (d) Edge detection (e) final image

In this study, a non-intrusive method to measure interfacial area for bubbly, slug, and churn flow is presented. The two-group approach for categorizing bubbles first formulated by Ishii and Mishima (1984) is used. Group 1 consists of spherical and distorted bubbles, whereas Group 2 consists of cap bubbles, Taylor bubbles, and irregular shaped bubbles characteristic of churn flow. The total interfacial area is estimated by individually calculating Group 1 and Group 2 interfacial areas (IA_1 and IA_2). A robust classification algorithm should be developed to distinguish Group 1 and Group 2 bubbles. The *regionprops* function in MATLAB is used to identify different objects in each frame and measure properties including area and perimeter. Once the objects are identified, the *area* function calculates the actual number of pixels in the region for each object and returns it as a scalar value (A_o). The equivalent diameter is calculated for each object using Eq. (3.2)

$$D_{eqv} = \sqrt{\frac{4A_o}{\pi}} \quad (3.2)$$

The Laplace length is determined next using Eq. (3.3), and is used to classify bubbles into Group 1 and 2.

$$Lo = \sqrt{\frac{\sigma}{g\Delta\rho}} \quad (3.3)$$

Group 1 objects are those with an equivalent diameter smaller than the Laplace length. For each object in Group 1, the bubble shape is determined by first obtaining the length of major and minor axes, a and b , respectively. If $a/b \leq 1.2$, the bubble is considered a sphere and the associated interfacial area is calculated. Bubbles with $a/b > 1.2$ are considered oblate spheroids and their area is calculated using Eq. (3.4)

$$A_{ob} = 2\pi \left(a^2 + \frac{b^2}{\sin \alpha} \ln \left(\frac{1 + \sin \theta}{\cos \theta} \right) \right) \quad (3.4)$$

where θ is angular eccentricity calculated using Eq. (3.5)

$$\theta = \cos^{-1} \left(\frac{a}{b} \right) \quad (3.5)$$

The interfacial area contribution from Group 1 (IA_1) bubbles is obtained by summation of individual areas. For Group 2 bubbles, the interfacial area is calculated by dividing the bubble into thin segments, each of 1 pixel height. The diameter of each section is measured, and the interfacial area is calculated as shown in Eq. (3.6)

$$IA_2 = \pi dy \sum_{i=0}^H D_i \quad (3.6)$$

The total interfacial area is obtained by adding Group 1 and 2 interfacial areas. To maintain consistency with the literature, the interfacial area per unit volume, also known as interfacial area concentration (IAC) shown in (Eq. (3.7)) is used.

$$IAC = \frac{IA_1 + IA_2}{Vol} \quad (3.7)$$

A summary of the algorithm used to calculate interfacial area is shown in Figure 3.8.

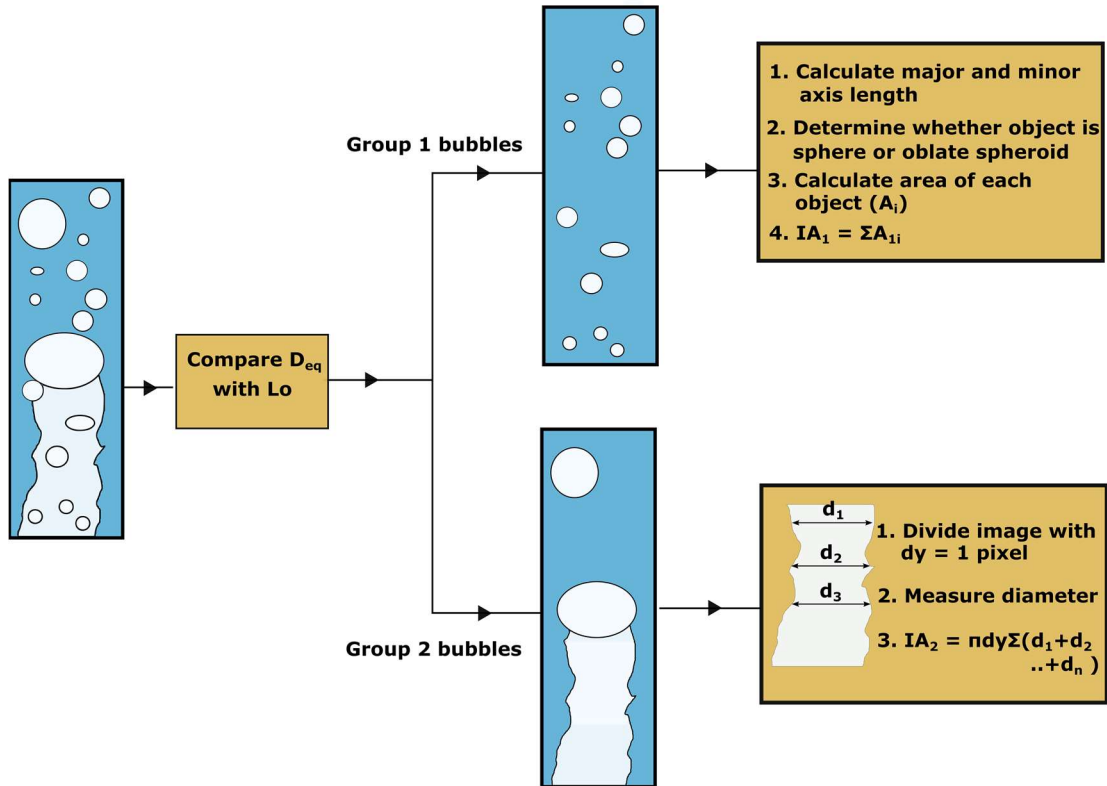


Figure 3.8: Algorithm to calculate interfacial area

3.4.3 Velocity

Image-based velocimetry has become more attractive and accessible because of the advancement in computational power. Integral techniques such as the well-established particle image velocimetry (PIV) were successfully applied to many flows (Hassan and Dominguez-Ontiveros, 2008). A modified technique that use bubbles as tracer particles under ordinary lighting conditions called bubble image velocimetry (BIV) has been demonstrated (Leandro et al., 2014). In contrast to PIV/BIV approaches, the optical flow method is not very well known to the two-phase flow community (Bung and Valero, 2016). Optical flow estimation is known from computer vision where it is used to determine obstacle movements through a sequence of images following an assumption of brightness conservation. This is mathematically shown by Eq. (3.8)

$$I(x, y, t) = I(x + dx, y + dy, t + dt) \quad (3.8)$$

where I is intensity of the pixel, and x and y are image plane co-ordinates. Using Taylor series approximation, this can be written as

$$I(x + dx, y + dy, t + dt) = I(x, y, t) + \frac{\partial I}{\partial x} dx + \frac{\partial I}{\partial y} dy + \frac{\partial I}{\partial t} dt + \dots \quad (3.9)$$

$$\Rightarrow \frac{\partial I}{\partial x} dx + \frac{\partial I}{\partial y} dy + \frac{\partial I}{\partial t} dt = 0 \quad (3.10)$$

Dividing Eq. (3.10) by dt , we get the optical flow equation.

$$\frac{\partial I}{\partial x} u + \frac{\partial I}{\partial y} v + \frac{\partial I}{\partial t} = 0 \quad (3.11)$$

where u and v are x and y velocities. The two-variable equation is solved to obtain the velocities. The solution to the optical flow equation can be implemented in two ways – sparse and dense. Sparse optical flow gives the flow vectors of some interesting features (e.g., the edges or corners of an object) within the frame, while Dense optical flow solves the flow vectors of all the pixels - up to one flow vector per pixel. Due to the high computational cost of dense solution, the present study employs the sparse implementation with the Lucas-Kanade algorithm using an open-source implementation in OpenCV 3.1.0 (Bradski and Kaehler, 2008).

The algorithm for particle identification presented by Shindler et al. (2012) is used in this study. It is based on the solution of the optical flow equation using sum-of-squared-difference (SSD) of the pixel intensity levels between interrogation windows in two consecutive frames. The corners are detected using the *good features to track* algorithm (Shi, 1994). Only the corners where image intensity gradients are not null in two orthogonal directions are considered. This makes it possible to identify low intensity and overlapped particles. Furthermore, the solution of the optical flow equation through the Lucas–Kanade algorithm enables the calculation of the local velocity vector that can be used as a predictor for the successive step of the particle, thus, reducing the computational time significantly.

3.5 Results

The results of flow visualization in air-water two-phase flow in the presence of surfactants are discussed in this section. The effect of a small amount of 1-octanol on flow patterns, interfacial area, and bubble velocity is described.

3.5.1 Flow patterns

The different flow patterns are identified by both direct visual observation during the experiments as well as the recorded video data. Three different flow patterns were observed in these experiments with and without surfactants – bubbly, slug, and churn flow. Figure 3.9 shows the effect of 1-octanol on flow patterns with increasing air flow rate. The data in Figure 3.9 were recorded at a fixed superficial liquid velocity of 0.036 m s^{-1} . Increasing the superficial liquid velocity to 0.072 m s^{-1} did not change the flow patterns. It was also observed that although the addition of surfactants did not change the transition of flow patterns, it had a significant impact on the detailed configuration within the flow pattern. These changes can be primarily attributed to the reduction of surface tension from 0.072 N m^{-1} to 0.028 N m^{-1} (Kini and Garimella, 2021).

At low mass flow rates of the air, discrete air bubbles are dispersed into the liquid continuum. This is known as bubbly flow regime. The surfactant additive reduces the tendency of air bubbles to coalesce. The bubbles are thus smaller in size and larger in number when compared to the pure air-water mixture. This is consistent with the observations of Rozenblit et al. (2006). Surfactants make the bubbles accumulate in the flow, thereby decreasing liquid holdup in bubbly flows as shown in the data presented by Liu et al. (2014). Another interesting observation is that the shapes of bubbles in pure air-water mixture are oblate spheres whereas the addition of surfactant leads to distortion of their shapes.










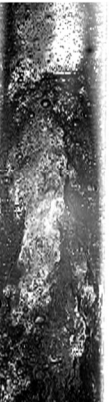
No surfactant					
500 PPM 1-octanol					
$j_g \text{ (m s}^{-1}\text{)}$	0.09	0.34	0.56	1.13	2.26

Figure 3.9: Effect of surfactant on flow patterns

An increase in air flow rate causes some bubbles to coalesce resulting in the formation of bullet-shaped Taylor bubbles, separated by liquid slugs containing small air bubbles. This flow regime is known as slug flow. The effect of surfactants in slug flow can be observed in Figure 3.10. The length of the Taylor bubble decreases with the addition of surfactants. A larger number of tiny bubbles are observed in the liquid slug region, thus

maintaining the overall mass balance. The presence of these smaller bubbles results in a larger interfacial area, improving heat and mass transfer.

As the air flow rate increases, the flow transitions to chaotic flow structures, which is characteristic of churn flow. In contrast to bubbly and slug flow regimes, both of which have a well-defined structure, churn flow appears unstable and is one of the least understood gas-liquid flow regimes (Ghiaasiaan, 2007). Although all these points demonstrate churn flow behavior, there are distinct differences even within churn flow that necessitate the development of sub-categories of discrete churn and dispersed churn flow. At superficial air velocities of $< 1.5 \text{ m s}^{-1}$, flows with and without surfactant are in discrete churn flow. However, the addition of surfactant results in the formation of small bubbles that are not observed in the baseline flow (Figure 3.9). At the highest air flow rate investigated, corresponding to a superficial air velocity of 2.26 m s^{-1} , a different phenomenon is observed in the presence of surfactant. The density of small bubbles is so high that too much light is deflected, which leads to a dark image, and it becomes difficult to identify the slugs. This is identified as dispersed churn flow. Such a phenomenon was also observed by Wang et al. (2021) where it was reported that these small bubbles exist in the thin liquid film without contacting the slug interface. This flow regime was observed at superficial velocities $> 10 \text{ m s}^{-1}$ by Wang et al. (2021). The presence of 1-octanol can thus achieve this flow regime at much lower velocities ($< 2.5 \text{ m s}^{-1}$). The high density of small bubbles augments the available interfacial area.

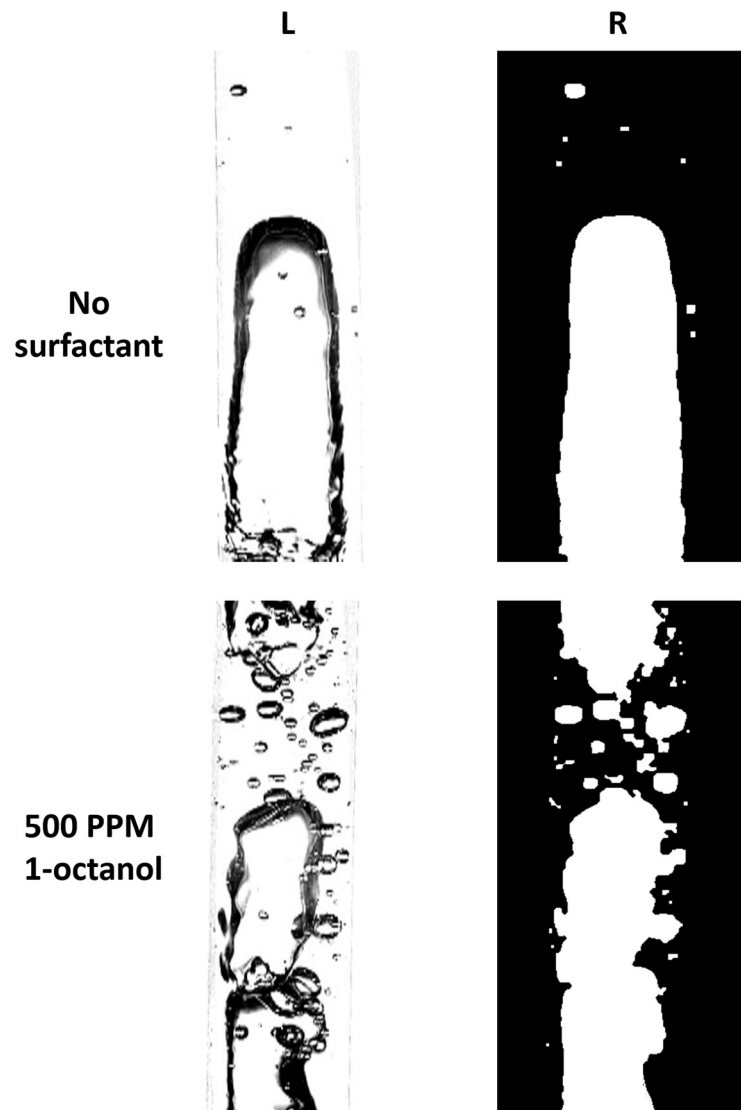


Figure 3.10: Comparison of slug flow in the presence of surfactant

3.5.2 *Interfacial area*

The interfacial area is measured as detailed in Section 3.4.2. The results are presented as interfacial area per unit volume or interfacial area concentration (IAC) to aid

comparison with the literature. Multiple videos are recorded for each data point and the mean and standard deviation of IAC are calculated. The mean values are plotted with the standard deviation as the uncertainty. It is observed that as the flow transitions from bubbly to slug flow, the IAC decreases due to the formation of large Taylor bubbles from the coalescence of smaller bubbles (Figure 3.11). Further increase in superficial air velocity results in an increase in IAC due to the breakup of large slugs and the chaotic flow structures formed in churn flow. This trend of a decrease followed by an increase in IAC as the flow transitions from bubbly to slug to eventually churn is not affected by the superficial liquid velocity. In all cases, the addition of surfactant enhances interfacial area. However, the magnitude of enhancement can vary depending on the flow regime. For bubbly flow, the enhancement is in the order of $\sim 12\%$, mainly due to the decrease in surface tension leading to smaller diameter bubbles. For slug and churn flow, the average enhancement in IAC is $\sim 54\%$ in the presence of surfactant. The primary reason for this enhancement is the breakup of large Taylor and irregular shaped bubbles to form higher number of Group 1 bubbles. The distribution of Group 1 bubbles in two cases of churn flow is shown in Figure 3.12. While the number of bubbles > 1 mm is not affected by the presence of surfactant, it has a significant impact on the number of small diameter bubbles. The population of bubbles < 0.5 mm is 3-5 times higher in the presence of 1-octanol, leading to the increase in interfacial area. The superficial air velocity can also impact IAC in churn flow, with an increase in velocity leading to higher density of smaller bubbles. It is observed that at $j_G = 0.56 \text{ m s}^{-1}$, the number of bubbles with diameters less than 0.5 mm and in the 0.5 – 1.0 mm range is similar, whereas at $j_G = 1.13 \text{ m s}^{-1}$, bubbles with diameter smaller than 0.5 mm vastly outnumber bubbles with diameters in the 0.5 – 1.0 mm range.

The Laplace length for the cases with 1-octanol is 1.7 mm. Thus, there are no Group 1 bubbles above 2 mm. It must be noted that the methodology presented in this work cannot be applied to dispersed churn flow. The images in this flow regime appear dark due to the reflection of light by the small bubbles that completely cover the circumference of the tube, thus preventing the detection of irregular shaped bubbles at the center of the tube.

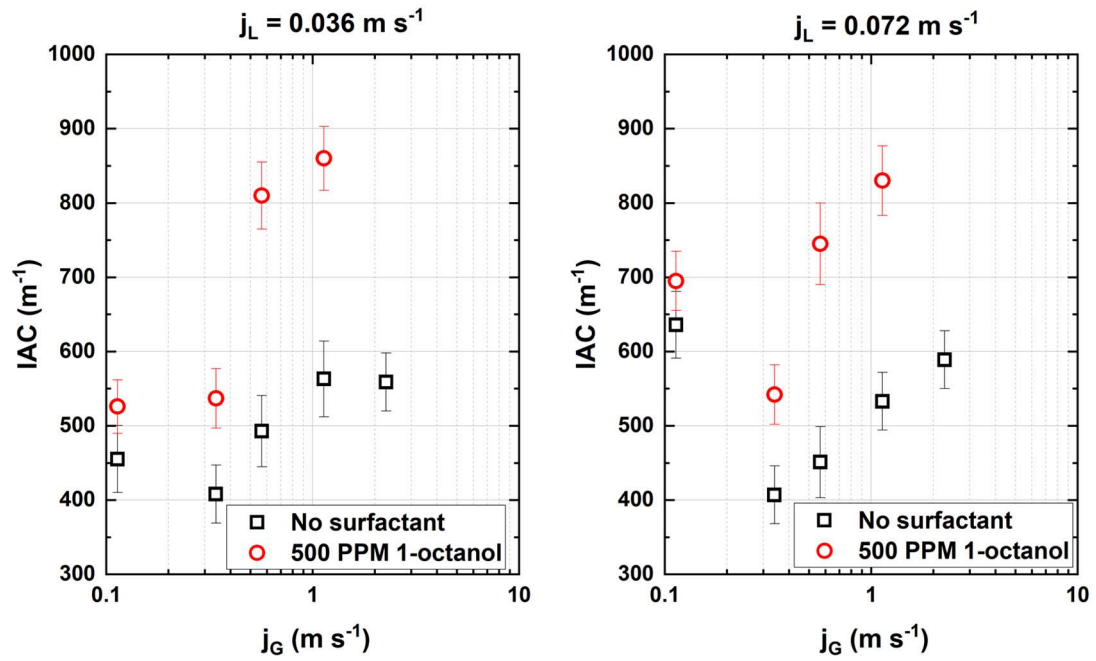


Figure 3.11: Variation of interfacial area concentration with superficial velocities

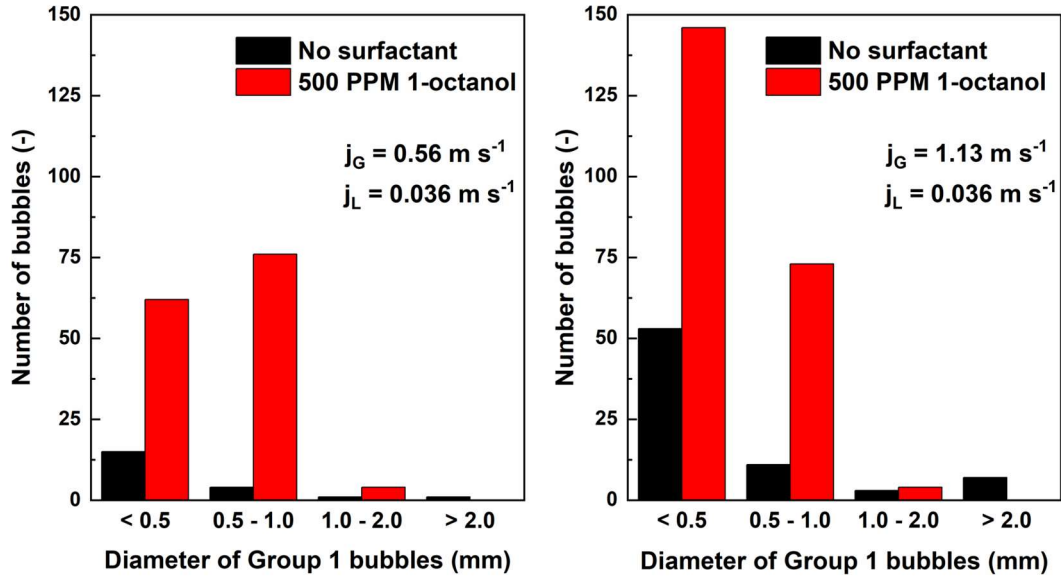


Figure 3.12: Group 1 bubble density variation

The measured values of IAC in this study are compared with the most commonly used models from the literature, by Dejesus and Kawaji (1990), Spore et al. (1993), and Ozar et al. (2012). Dejesus and Kawaji (1990) presented an empirical model by correlating interfacial area to superficial liquid and gas velocities. While it is one of the simplest models, the prediction of IAC for the conditions of the present study is very poor, sometimes by an order of magnitude. This can be attributed to the simple correlation, which does not account for flow morphology or physical properties and was developed using a database of air-NaOH solution and therefore, is unsuitable for other fluids.

Both the Spore et al. (1993) and Ozar et al. (2012) models are based on the two-group approach of Ishii and Mishima (1980), who developed the following relation using simple geometric considerations

$$IAC = \frac{4.5C_t}{D_H} \frac{\alpha - \alpha_{gs}}{1 - \alpha_{gs}} + \frac{6\alpha_{gs}}{D_{sm}} \frac{1 - \alpha}{1 - \alpha_{gs}} \quad (3.12)$$

The first term on the right hand side of Eq. (3.12) is the contribution of Group 2 bubbles, while the second term is the contribution of Group 1 bubbles. In this equation, α_{gs} is the average void fraction in the liquid slug and film.

The key difference between these two models is the treatment of the Group 1 contribution, specifically the calculation of mean diameter of small bubbles D_{sm} . In the Spore et al. (1993) model, which was developed by Los Alamos National Laboratory primarily for simulating nuclear power plant operation in the Transient Reactor Analysis Code (TRAC), the bubble size is estimated using the Laplace length scale such that

$$D_{sm} = 2Lo \quad (3.13)$$

Where the Laplace length scale Lo , is given as

$$Lo = \sqrt{\frac{\sigma}{g\Delta\rho}} \quad (3.14)$$

The effect of surface tension is accounted for by Lo . In the presence of surfactant, a reduction of surface tension leads to a lower Lo , which in turn decreases the D_{sm} . A smaller D_{sm} leads to higher IAC according to Eq. (3.12). Ozar et al. (2012) developed an empirical correlation Eq. (3.15)

$$\frac{D_{sm}}{Lo} = 1.99 \left(\frac{Lo}{D_H} \right)^{-0.335} \left(\frac{\varepsilon^{1/3} Lo^{4/3}}{v_L} \right)^{-0.239} \quad (3.15)$$

where ε is energy dissipation rate per unit mass. It is the sum of energy dissipation due to bubble expansion and due to wall friction, and is calculated using the method presented by Hibiki and Ishii (2002). The IAC predictions using both these models are compared with the measured values from this study (Figure 3.13). The Spore et al. (1993) model underpredicts all data with an average deviation of -26%. The Ozar et al. (2012) model performs better, with an average absolute deviation of 21%. Specifically, this model overpredicts the data in the absence of surfactants and underpredicts the data when the surface tension is reduced. While the model accounts for changes to the diameters of the Group 1 bubbles, it does not account for changes to the length of Taylor and other Group 2 bubbles in the presence of surfactants, leading to this underprediction.

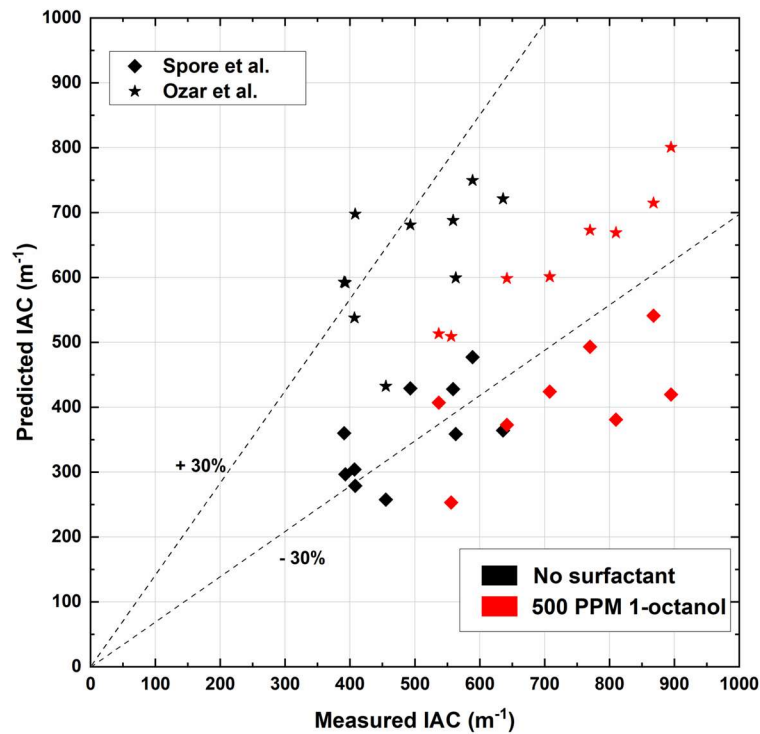


Figure 3.13: Measured versus predicted IAC

3.5.3 Velocity

The results of the optical flow method for velocity estimation are discussed in this section. To visualize the operation of this algorithm, 25 tracer particles are used to plot the movement of bubbles at timesteps of 0.067 s (Figure 3.14). The *good features to track* algorithm is to identify the best positions to start tracking these particles. The density of tracer particles can affect the results of this method. This can be understood as analogous to grid independence in computational methods in heat transfer and fluid flow. Many tracer particles must be used such that the results are independent of the number of particles. This ensures that all features of the flow are captured. According to Figure 3.15, increasing the number of tracer particles beyond 150 does not affect the results. In this study, 250 tracer particles are used for every data point with each having a size of 3 pixels.

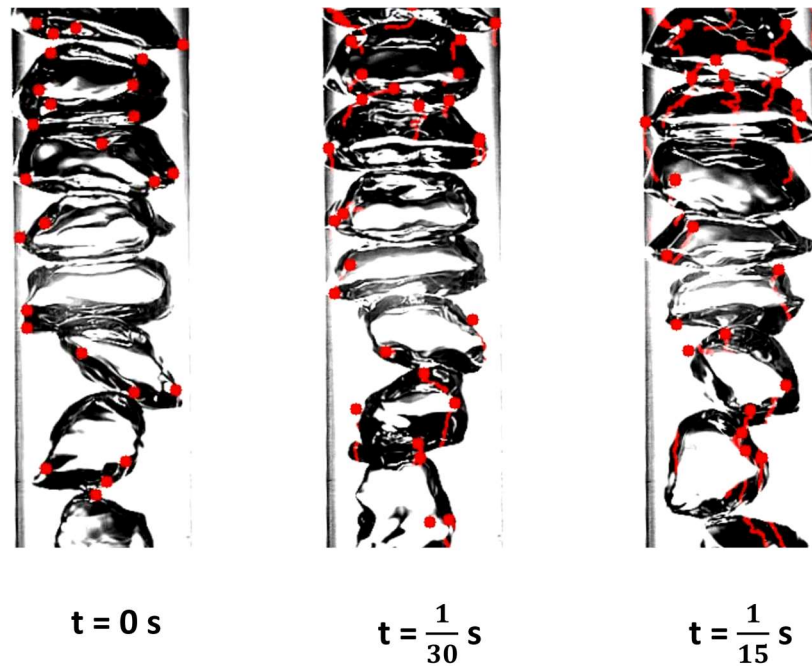


Figure 3.14: Visualization of optical flow algorithm

Figure 3.16 shows the bubble velocity in pure water and surfactant solution as a function of air Reynolds number (Re_{air}). At a fixed Re_{air} , the bubble velocity increases with increasing liquid Reynolds number. Similarly, there is a linear dependence of velocity on air Reynolds number when the liquid Reynolds number remains constant. The addition of 1-octanol leads to a reduction of bubble velocity in all cases, typically ranging from 4-8%. As a bubble rises in surfactant solution, surfactant molecules are adsorbed on the surface of the bubble and are typically swept off the front part and accumulate in the rear half of the bubble. This leads to a variation of surface tension along the bubble surface, which causes tangential shear stress on the surface. This shear stress results in an increase in drag, which causes the reduction of the rising velocity.

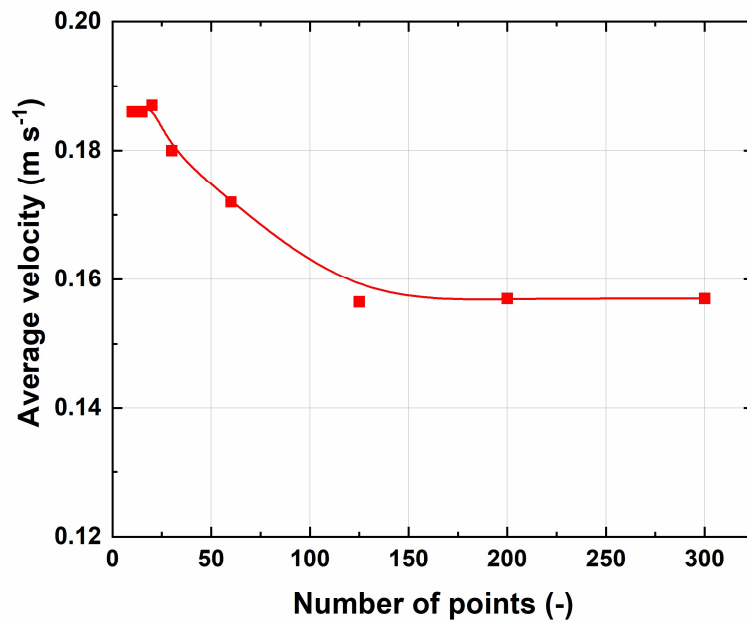


Figure 3.15: Tracer independence for optical flow

In addition, surfactants can affect the lateral movement of bubbles (Takagi et al., 2008; Takagi and Matsumoto, 2011). The optical flow method can track the motion of bubbles as they travel along the height of the tube. It is observed that in the presence of 1-octanol, the bubbles exhibit a zig-zag path as shown in Figure 3.17. This is also a result of unequal shear forces acting on the bubble surface due to the non-uniform adsorption of surfactant molecules. The combined effect of reduced velocity and zig-zag motion is an increase in residence times between the gas and liquid, leading to higher rates of heat and mass transfer in several multiphase processes.

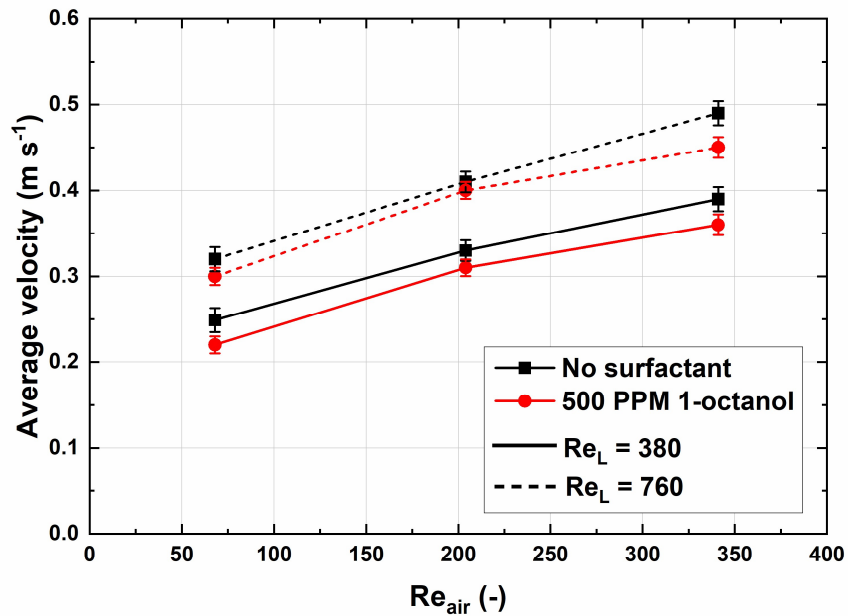


Figure 3.16: Velocity results

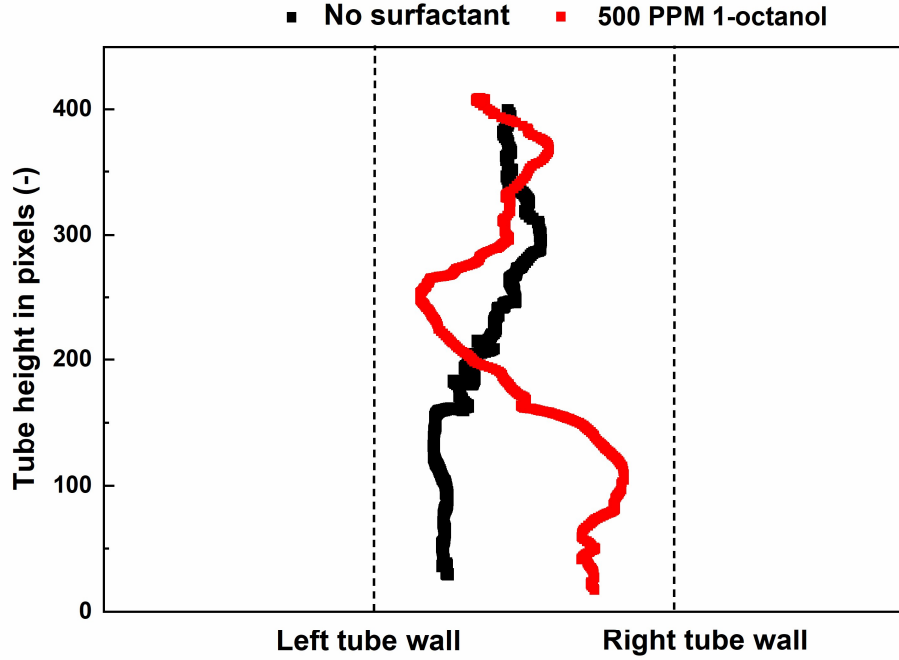


Figure 3.17: Effect of surfactant on bubble path

3.6 Conclusions

Vertical gas-liquid two-phase flow is experimentally investigated in a 12.7-mm diameter tube in the bubbly, slug, and churn flow regimes. The effect of adding 1-octanol, a surfactant, is studied using high-speed videography. Interfacial areas and bubble velocities are estimated using non-intrusive computer vision based methods. Although surfactants do not affect the transition of flow regimes, they had a significant impact on the detailed configuration of flow structures within each flow regime. These changes to the flow structures resulted in enhancement in interfacial areas by up to 37%. The highest enhancements were observed in slug and churn flows. Measured values of interfacial area are compared with predictions from correlations in the literature, and the Ozar et al. (2012)

model performed the best with an AAD of 21%. The optical flow method is used to track the bubble path and measure velocity. In the presence of surfactants, residence time increases due to lower velocity and zig-zag path traversed by bubbles. The combined effect on interfacial areas and velocities can lead to appreciable enhancement of heat and mass transfer rates in various industrial processes.

CHAPTER 4. EFFECT OF SURFACTANTS ON THE PERFORMANCE OF BUBBLE ABSORBERS

This chapter presents an investigation on the effects of surfactants on the performance of a bubble absorber. Experiments are performed in a single-pressure facility. A heat and mass transfer model is developed and validated using experimental data.

4.1 Introduction

A key deterrent to the widespread adoption of vapor absorption heat pumps is the larger system footprint compared to that of vapor compression systems. The absorber, where the refrigerant vapor mixes with the absorbent in a coupled heat and mass transfer process, is typically the largest component, and can often dictate the overall size of the system (Kini et al., 2020). The absorber also greatly affects the overall performance of the heat pump and is considered as the primary bottleneck in these systems (Sözen, 2001). Absorbers can be classified into three categories depending on the mode of operation – falling-film, spray, and bubble absorbers (Sehgal et al., 2021). The mode of absorption can significantly impact the performance of the absorber as shown by many studies that compare these different modes (Kang et al., 2000; Lee et al., 2002; Castro et al., 2009).

Researchers have used passive heat and mass transfer intensification techniques to enhance absorption rates that would yield a more compact absorber, or to reduce the driving heat input temperature (Amaris et al., 2018). Passive intensification techniques include the use of rough or extended surfaces, or the inclusion of small quantities of additives or

nanocomposites to the base working fluids. A detailed review of all experimental studies that demonstrate passive intensification in absorbers is presented in Amaris et al. (2018).

Surface-active agents or surfactants are chemicals that can be added to change the surface tension of the base fluid. When surfactants are introduced in an absorber, they induce surface tension gradients in the solution and vapor, causing the Marangoni effect and resulting in higher heat and mass transfer coefficients (Bergles and Manglik, 2013). Surfactants have been widely used in falling-film absorbers, especially with water-LiBr as the working fluid (Hihara and Saito, 1993; Nakoryakov et al., 2008; Fu Lin and Shigang, 2011). In addition to Marangoni convection, the reduction in surface tension typically improves the wettability of the falling films and provides a larger surface area for heat and mass transfer. Higher wetting can also lead to thinner films, further enhancing heat transfer coefficients (Kini et al., 2021).

Bubble absorbers are preferred for ammonia-water absorption systems because of the high heat and mass transfer coefficients and the ease in designing vapor distribution systems as compared to liquid distributors required for falling-film absorption (Kang et al., 1998; Cerezo et al., 2011). Yet there are a limited number of studies that consider the effects of surfactants in bubble absorbers. A numerical study showed that absorber size can be reduced by as much as 60% by adding surfactants (Kim et al., 2007a). However, the results were not experimentally validated. Kim et al. (2006) performed bubble absorption experiments using ammonia-water to understand the effect of surfactants. They reported that absorption performance can be enhanced by up to 4.81 times in the presence of surfactants. Although their results highlight the significance of adding surfactants, the experiments were adiabatic and were performed in the absence of cooling fluid and

associated heat transfer. This is not representative of the coupled heat and mass transfer processes in a typical absorber. In addition, Fernández-Seara et al. (2005) showed that the dominant flow regime in absorbers is churn and slug flow whereas the study of Kim et al. (2006) considered only the bubble flow regime.

The objectives of the present study are to analyze the combined heat and mass transfer processes in a bubble absorber in the presence of surfactants at representative conditions. An experimental facility is constructed, and bubble absorption experiments are performed at various flow rates, coupling fluid temperatures and surfactant concentrations. A heat and mass transfer model is developed to predict the performance of the absorber and the results are interpreted.

4.2 Experimental test section and facility

The bubble absorber considered in this study is a vertical tube-in-tube heat exchanger as shown in Figure 4.1. The ammonia-water mixture flows upward in the inner tube, while the coupling fluid flows downward in the annulus region. Ammonia enters the test section through a single orifice tube. This design configuration is commonly used in shell-and-tube (Fernández-Seara et al., 2005) and plate-type absorbers (Cerezo et al., 2009). A 0.05-m adiabatic mixing section is included at the entrance of the test section as shown in Figure 4.1b. The temperature of the two-phase mixture exiting the adiabatic mixer is measured using an inline thermocouple (Figure 4.1b). The tube-in-tube heat and mass exchanger is fabricated using 304 Stainless Steel, with a 0.0127-m OD inner tube and 0.019-m OD outer tube. The wall thickness of both tubes is 8.89×10^{-4} m. The total length of the component, including the adiabatic mixing section, is 0.30-m.

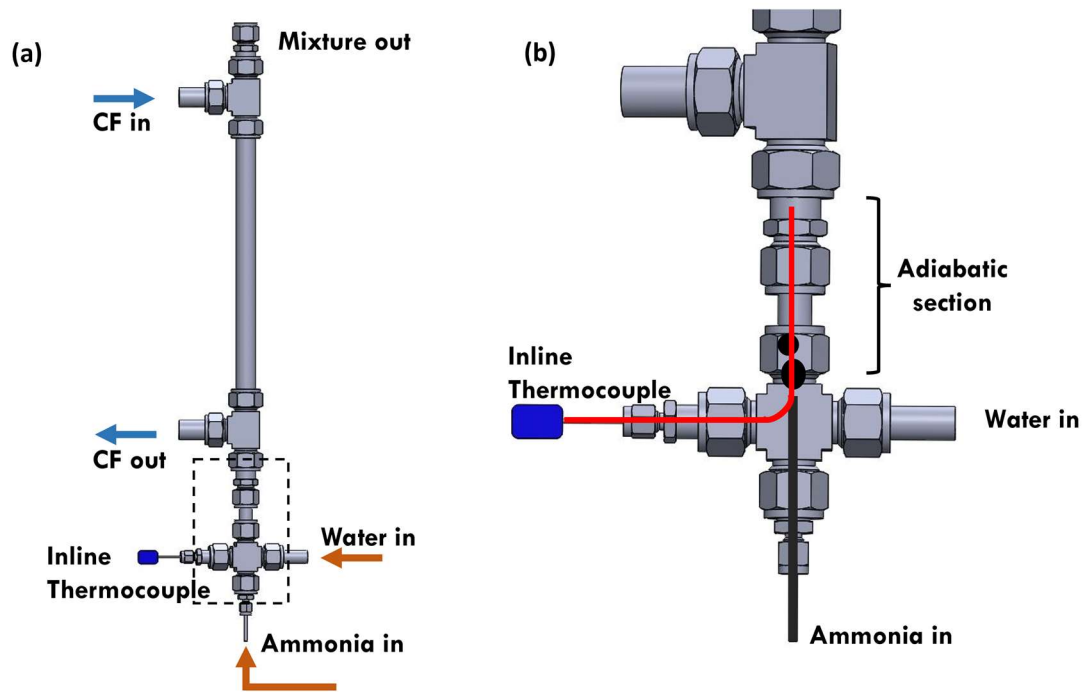


Figure 4.1: (a) Test section schematic (b) Detailed view of adiabatic mixing section

An experimental facility consisting of an open ammonia-water loop and a closed coupling fluid loop is designed and fabricated (Figure 4.2). An ammonia reservoir is used to supply ammonia vapor with a purity of 0.999. A pressurized water tank is used to supply distilled water to the absorber. High precision needle valves (Ideal valve model 54-1-11) are used to control the flow rate of both ammonia and water independently. The valve can control the flow rates of each fluid with a precision of $2 \times 10^{-5} \text{ kg s}^{-1}$. Electric tape heaters (500 W) with variable load controllers are used to pre-condition the water and ammonia streams to the required test conditions. The ammonia is absorbed along the height of the absorber and exits as a single-phase concentrated solution into a discharge tank. A sight glass is provided at the exit to verify that absorption is complete. The coupling fluid

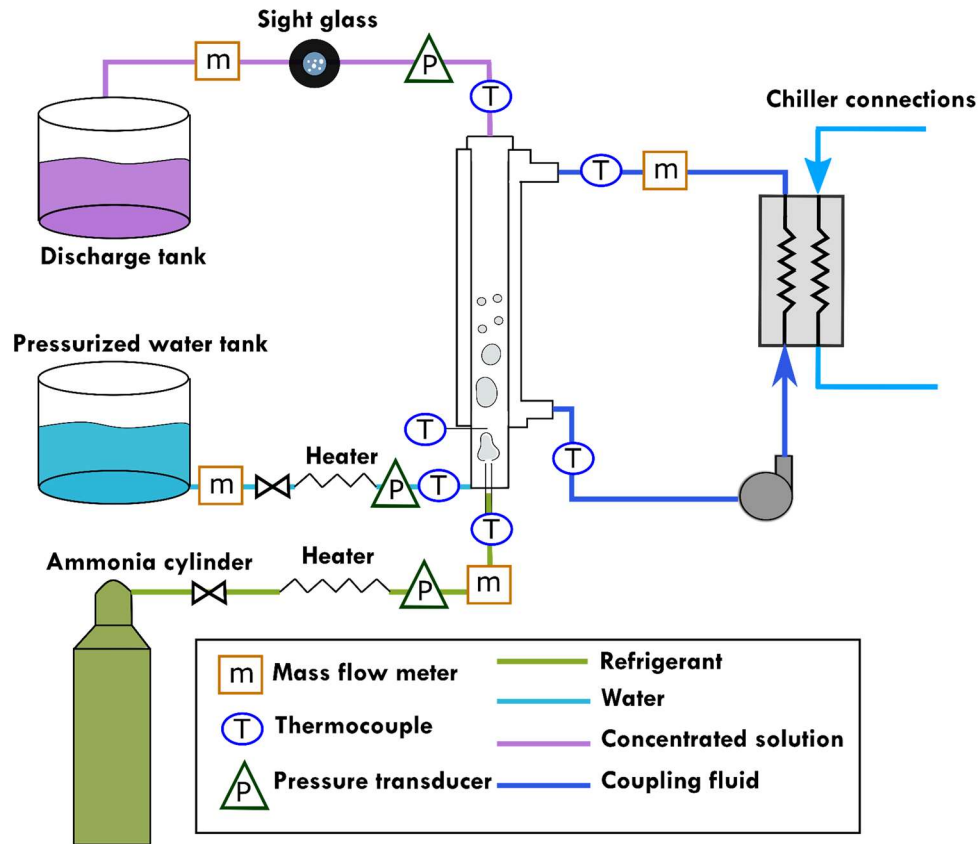


Figure 4.2: Schematic of experimental facility

(distilled water) enters the absorber from the top and flows in counter-current direction to remove the heat generated during absorption. This heat is then rejected to an external chiller to maintain the desired coupling fluid temperature. A photograph of the test facility is shown in Figure 4.3.

4.2.1 Measurements and instrumentation

Micro Motion Coriolis-type meters (CMFS010; Error: $\pm 0.1\%$) are used to measure the mass flow rates of water at the inlet, concentrated solution at the exit of the absorber, and the coupling fluid. A low flow Coriolis-type meter (Emersion LF3M) is used to

measure the flow rate of ammonia. WIKA model S-10 pressure transducers are used to measure the pressure of each fluid stream with an uncertainty of $\pm 0.25\%$. T-type thermocouples are used for all temperature measurements. National Instrument compact-RIO based data acquisition system is used to record all measurements. Table 4.1 summarizes the instrumentation and corresponding uncertainties.

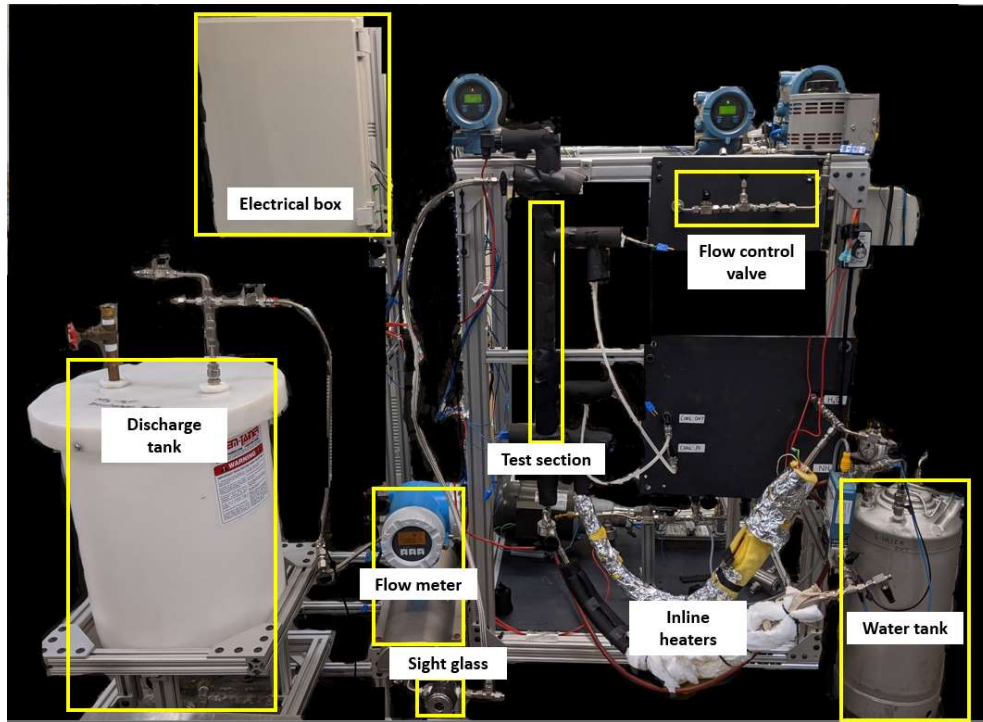


Figure 4.3: Photograph of test facility

The bubble absorber is tested at four water flow rates between $0.6 - 1.2 \times 10^{-3} \text{ kg s}^{-1}$, two ammonia flow rates ($0.05 - 0.1 \times 10^{-3} \text{ kg s}^{-1}$), and three coupling fluid temperatures (15°C , 20°C , 25°C) as shown in Table 4.2. In addition, the effects of coupling fluid flow rate and system pressure are studied. The experiments begin by circulating the coupling

fluid at the desired temperature. The valve on the water stream is then opened carefully to set the water flow rate as desired. The ammonia stream valve is opened and the PID controllers that manage the tape heaters are switched on. The sight glass is then visually inspected to determine if absorption is complete. The presence of any vapor bubbles indicates incomplete absorption. For each point, data are collected for 15 minutes to mitigate effects from transient perturbations. The effect of surfactants on bubble absorption is studied by performing the above experiments after adding surfactants to the pressurized water tank. 1-octanol is the surfactant used in this study based on the findings of Chapter 2. After 1-octanol is added to the tank, it is stirred with water to ensure it is mixed thoroughly.

Table 4.1: Instrumentation and uncertainties

Variable	Instrument/sensor	Range	Uncertainty
Fluid temperature	Omega TMQSS-125G	0 to 315°C	$\pm 0.25^{\circ}\text{C}$
Pressure	WIKA S-10	0 to 689 kPa	$\pm 0.25\%$ of full span
Mass flow rate (Solution and coupling fluid)	Micro Motion CMFS010	0-0.03 kg s ⁻¹	$\pm 0.1\%$ of reading
Mass flow rate (ammonia vapor)	Micro Motion LF3M	0-0.4 kg h ⁻¹	$\pm 0.5\%$ of reading

Table 4.2: Bubble absorber test matrix

$\dot{m}_{wat} (\times 10^{-3} \text{ kg s}^{-1})$	0.6		0.8		1.0		1.2	
$\dot{m}_{am} (\times 10^{-3} \text{ kg s}^{-1})$	0.05	0.1	0.05	0.1	0.05	0.1	0.05	0.1
$T_{CF} = 15^\circ\text{C}$	×	×	×	×	×	×	×	×
$T_{CF} = 20^\circ\text{C}$	×	×	×	×	×	×	×	×
$T_{CF} = 25^\circ\text{C}$	×	×	×	×	×	×	×	×

4.3 Data reduction

This section describes the data reduction methodology used for analyzing and interpreting the results from the experiments. The key parameter to be measured in the experiments is the heat duty of the absorber. The heat duty is measured using both the coupling fluid side and working fluid (ammonia-water) side. For the coupling fluid, heat duty is calculated using

$$\dot{Q}_{abs,CF} = (\dot{m}c_p)_{CF} (T_{CF,out} - T_{CF,in}) \quad (4.1)$$

On the working fluid side, the inlet enthalpies of both the ammonia vapor and solution stream are calculated using the measured temperature and pressure at the inlet of the test section. The outlet enthalpy is calculated using the measured temperature and pressure, and the calculated concentration of the solution (Eq. (4.2)).

$$x_{conc,out} = \frac{\dot{m}_{vap,in}}{\dot{m}_{vap,in} + \dot{m}_{dil,in}} \quad (4.2)$$

The vapor flow rate can also be calculated from the difference between the concentrated and dilute solution flow rates, thus providing a redundant measurement for each data point.

The heat duty of the absorber on the working fluid side is calculated using

$$\begin{aligned} \dot{Q}_{abs,WF} = & \dot{m}_{vap,in} h_{vap,in} (T_{vap,in}, P_{vap,in}) + \dot{m}_{dil,in} h_{dil,in} (T_{dil,in}, P_{dil,in}) - \\ & \dot{m}_{conc,out} h_{conc,out} (T_{conc,out}, P_{conc,out}, x_{conc,out}) \end{aligned} \quad (4.3)$$

To quantify the absorber heat exchanger performance, the UA-LMTD method is employed, where the LMTD is calculated using the driving temperature differences at the inlet and the outlet. For the heat transfer section, the appropriate characteristic temperature for the working fluid at the inlet is the measured mixture temperature at the end of the adiabatic section. The difference between this measured temperature and the coupling fluid outlet temperature provides the driving force for heat transfer at the inlet of the absorber. Eqs. (4.4) and (4.5) are used to estimate the UA of the absorber.

$$LMTD_{abs} = \frac{(T_{mix,in} - T_{CF,out}) - (T_{conc,out} - T_{CF,in})}{\ln \left[\frac{(T_{mix,in} - T_{CF,out})}{(T_{conc,out} - T_{CF,in})} \right]} \quad (4.4)$$

$$UA_{abs} = \frac{\dot{Q}_{abs,CF}}{LMTD_{abs}} \quad (4.5)$$

The thermal resistance network in the absorber is comprised of three resistances as shown in Figure 4.4. The coupling fluid-side thermal resistance is calculated by Eq.(4.6) using the

correlation for heat transfer coefficient for flow in annulus developed by Garimella and Christensen (1995). The wall and solution-side resistances are determined as shown in Eqs. (4.7) and (4.8), respectively.

$$R_{CF} = \frac{1}{\alpha_{CF} \cdot A_{CF}} \quad (4.6)$$

$$R_{wall} = \frac{\ln(d_{out} / d_{in})}{2 \cdot \pi \cdot k_{SS} \cdot L} \quad (4.7)$$

$$R_{sol} = \frac{1}{UA_{abs}} - R_{CF} - R_{wall} \quad (4.8)$$

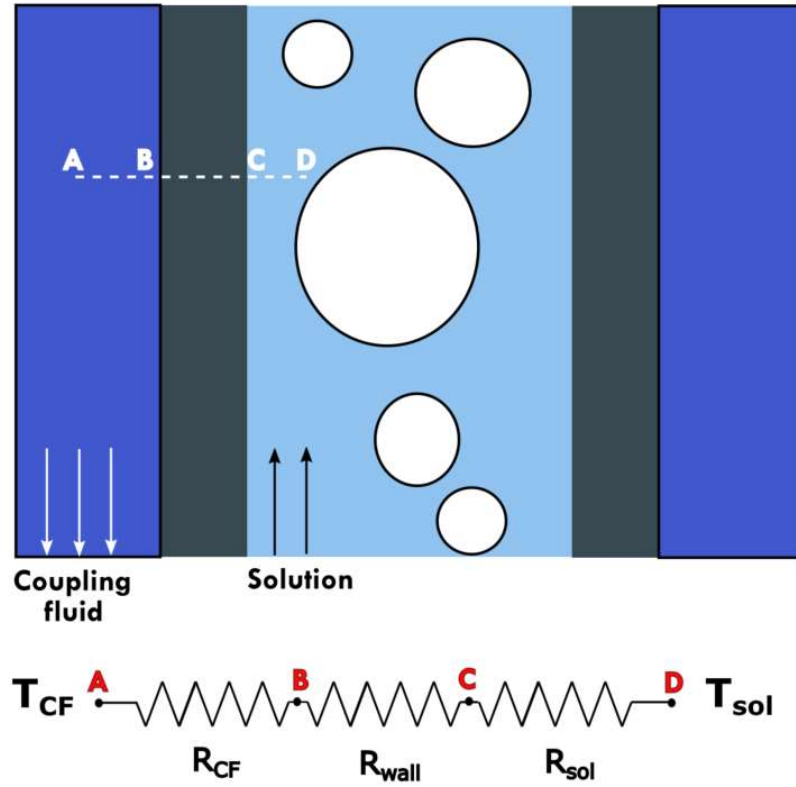


Figure 4.4: Heat transfer resistance network

Ammonia-water mixture is zeotropic, and its condensation involves a combination of heat and mass transfer. It must be noted that the resistance calculated from Eq. (4.8) will yield an apparent heat transfer coefficient (Eq. (4.9)), which is an aggregate of the coupled heat and mass transfer resistances. The apparent heat transfer coefficient has been demonstrated to be a useful metric in illustrating absorber performance (Fronk and Garimella, 2016).

$$R_{sol} = \frac{1}{\alpha_{sol,app} \cdot A_{sol}} \quad (4.9)$$

An uncertainty analysis is conducted to propagate the measurement uncertainties of sensors to estimate uncertainties in the reported parameters using the method suggested by Taylor and Kuyatt (1994). Appendix A presents detailed calculations for a sample data point.

4.4 Experimental results

The results of ammonia-water absorption experiments with and without the addition of surfactants are discussed in this section.

4.4.1 Energy balance

Figure 4.5 compares the heat duty of the absorber calculated using the measurements on the coupling fluid side with that of the working fluid side. The coupling fluid heat duties of more than 80% of the cases are within 5% of working fluid heat duties. The close agreement between calculated and measured heat duties demonstrates the validity of the measurements and assumptions of the data reduction model. It is also noted that the absolute average deviation (AAD) for the cases with surfactant is 5.4% while the

AAD increases to 8.1% for cases without surfactants. This can be attributed to some cases at higher vapor flow rates when absorption of ammonia is not completed. The heat transfer rates calculated from the working fluid side are higher than those calculated on the coupling fluid side. This deviation indicates that a two-phase mixture of sub-cooled ammonia-water solution and ammonia vapor exits the absorber. This is verified visually using the sight glass where bubbles of ammonia vapor are observed. This indicates that the absorber could be limited by liquid-side mass transfer resistance (Hoysall and Garimella, 2018). This is primarily a result of the low diffusivity of ammonia in liquid ($D_{aw,l} \sim 10^{-9}$) as compared to the diffusivity of ammonia in the vapor phase ($D_{aw,v} \sim 10^{-6}$).

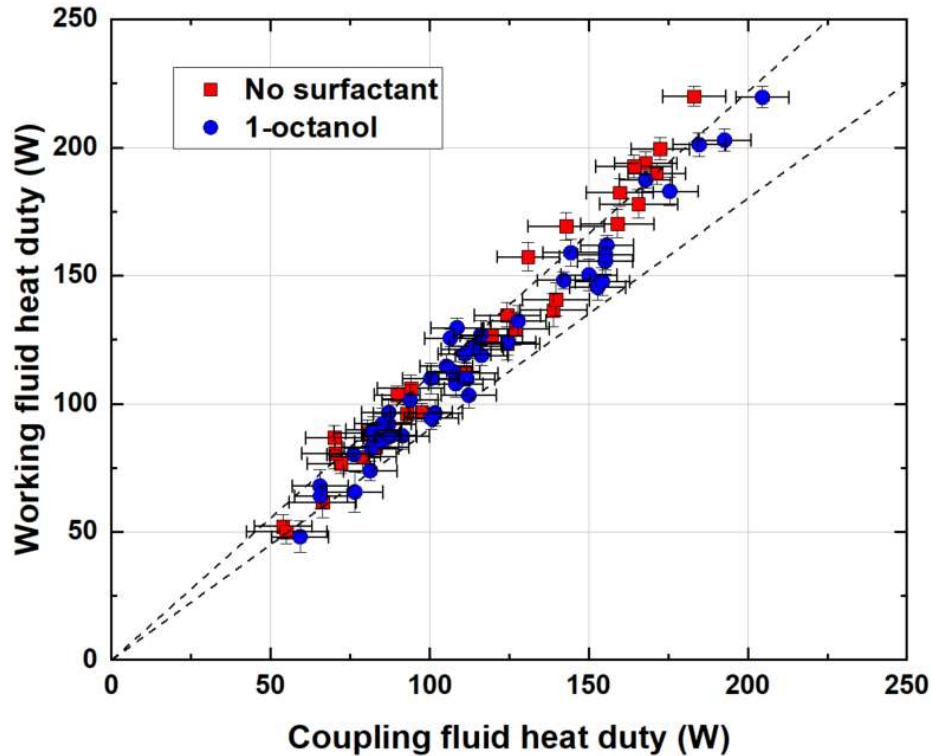


Figure 4.5: Energy balance of all data points

4.4.2 Effect of coupling fluid flow rate

The impact of varying the coupling fluid flow rate on the solution-side resistance is shown in Figure 4.6. For all the cases, the coupling fluid is in the laminar flow regime, and therefore, the heat transfer coefficient and associated coupling fluid thermal resistance (R_{CF}) remain constant. Any increase in the flow rate would yield a lower temperature difference in the coupling fluid between the inlet and outlet of the absorber. This would increase the uncertainty in the calculated parameters, including the solution side resistance (R_{sol}) and apparent solution heat transfer coefficient (α_{sol}). Therefore, all the tests are performed at the lowest possible flow rate that could be achieved with the given coupling fluid pump resulting in uncertainties of 15% or lower.

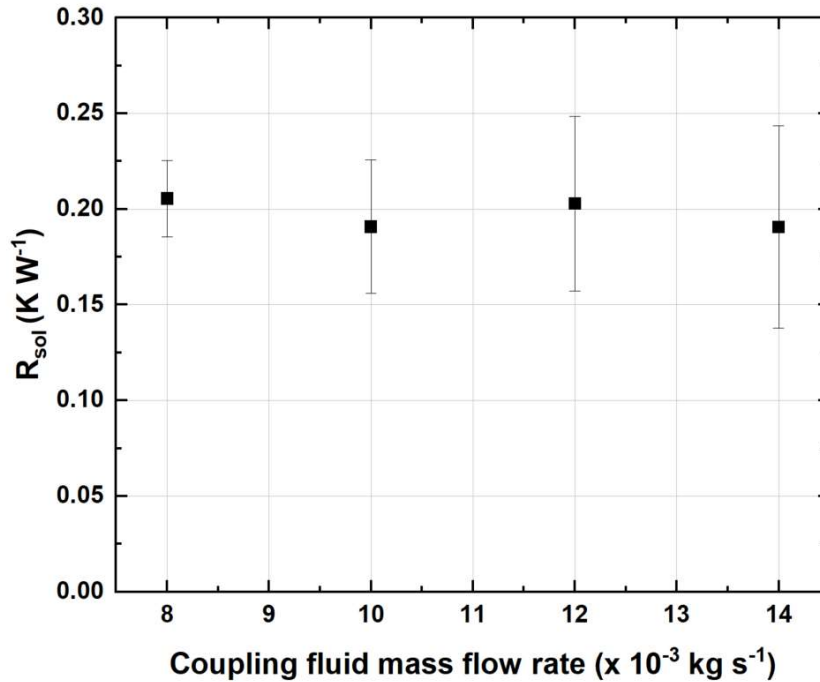


Figure 4.6: Effect of coupling fluid flow rate

4.4.3 *Effect of surfactant concentration*

The performance of the absorber as a function of surfactant concentration at a fixed working fluid flow rate is shown in Figure 4.7. The addition of surfactant results in increased mass transfer coefficient due to interfacial turbulence (Kim et al., 2006). A lower value of surface tension also affects bubble diameter and bubble density and yields a much higher interfacial area, which plays a significant role in both heat and mass transfer in ammonia-water mixtures. Even a small amount of surfactant (25 PPM) leads to a reduction in the solution-side resistance. Concentrations of 300 PPM and 500 PPM demonstrate the highest enhancement of 35%. The surface tension of ammonia-water solution with surfactant plateaus at 500 PPM of 1-octanol, with any addition beyond 500 PPM not leading to further reduction in surface tension. It was anticipated that there would be no further reduction of the solution-side resistance beyond 500 PPM. Instead, the resistance increased significantly at 2000 PPM of 1-octanol, performing worse than the case without any surfactants. This is due to a reduction in mass transfer because of the “barrier” effect (Agble and Mendes-Tatsis, 2000). At high concentrations, surfactant molecules will accumulate at the interface forming ordered or layered structures and reducing the available area for transport. The combined effect of the two competing phenomena – Marangoni convection and barrier effect dictates the overall performance of adding surfactants (Zhang et al., 2013).

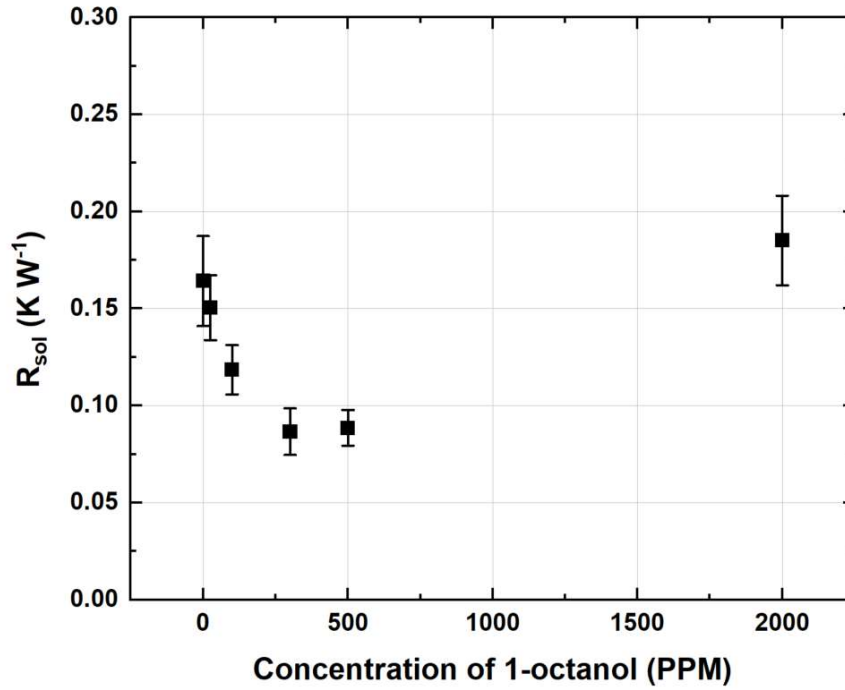


Figure 4.7: Effect of surfactant concentration

4.4.4 Thermal resistance

Figure 4.8 plots the apparent heat transfer coefficient with vapor Reynolds number. The Reynolds number increases with an increase in the mass flow rate of ammonia. At low Reynolds numbers, all the ammonia vapor is completely absorbed into the solution and the presence of 1-octanol does not have a large impact on the performance. An enhancement of ~5% is observed in these cases due to a larger portion of the heat exchanger area being available for subcooling in the presence of surfactants. At high vapor Reynolds numbers, enhancements of up to 35% are observed. These are due to cases when the addition of surfactants results in complete absorption as compared to incomplete absorption in cases without surfactant. Although surfactants directly impact the mass transfer performance,

the apparent heat transfer coefficient accounts for both heat and mass transfer and can be used as a surrogate parameter to study the effect of surfactants. The importance of this can be understood from Figure 4.9, which shows the solution-side resistance as a fraction of the overall resistance. At high ammonia flow rates, the solution-side resistance can decrease from 65% of the overall resistance to less than 50%. The dominant resistance can move from the working fluid-side to the coupling fluid-side.

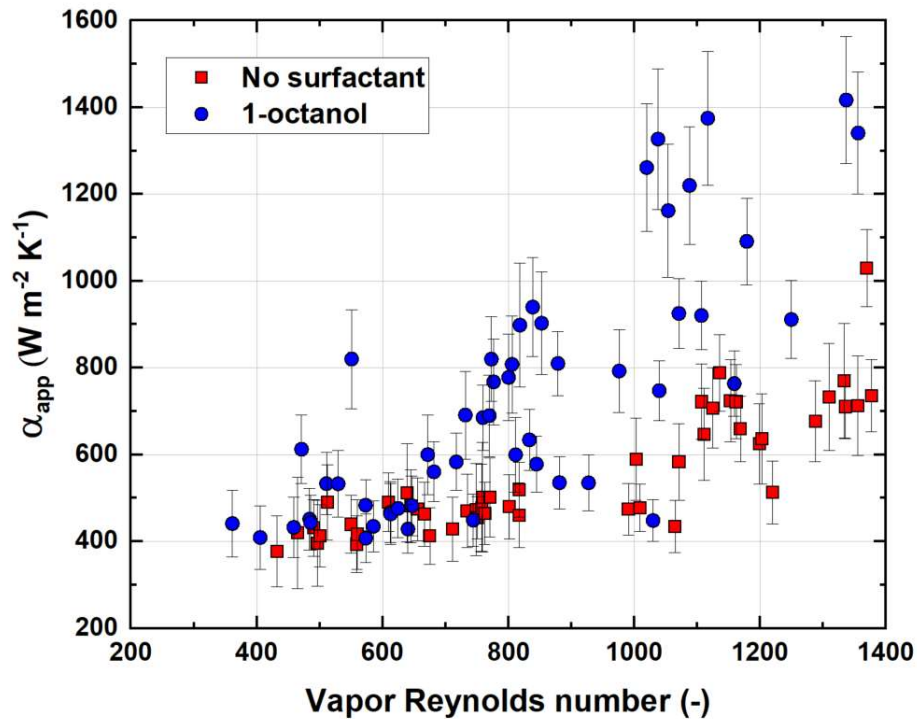


Figure 4.8: Variation of apparent heat transfer coefficient with the addition of 1-octanol

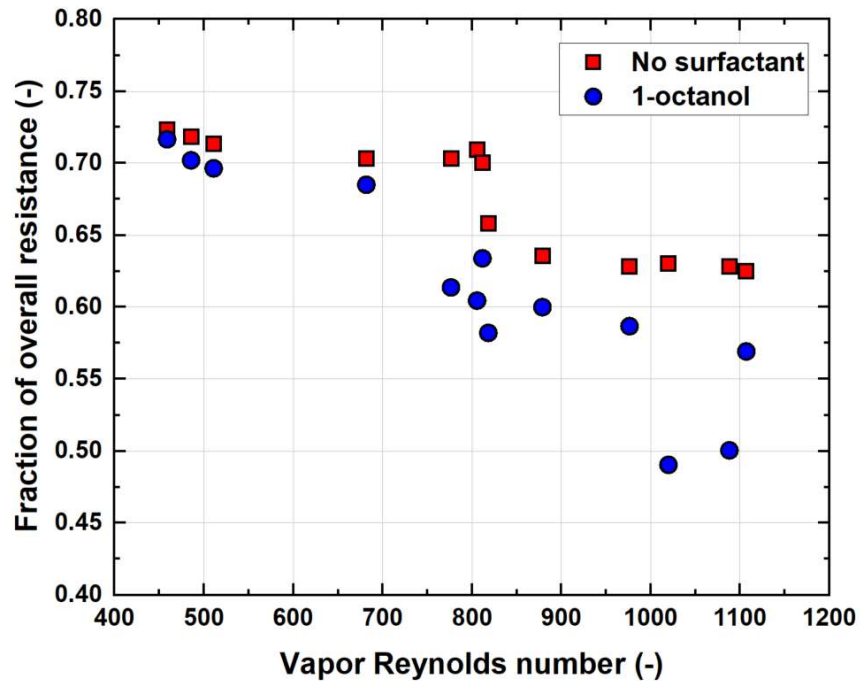


Figure 4.9: Solution resistance as a fraction of the overall resistance

The effect of system operating pressure on the solution-side resistance is shown in Figure 4.10. When all other parameters are held constant, the change in absorber pressure does not lead to any appreciable change in absorber performance. At lower pressure, the ammonia-water mixture has a higher vapor specific volume and results in higher bubble and slug velocities. This yields higher heat and mass transfer coefficients. However, this is balanced by the reduced concentration at the interface at lower pressures leading to a reduction in the driving concentration difference. The effect of surfactants is not significantly impacted by the change in system pressure.

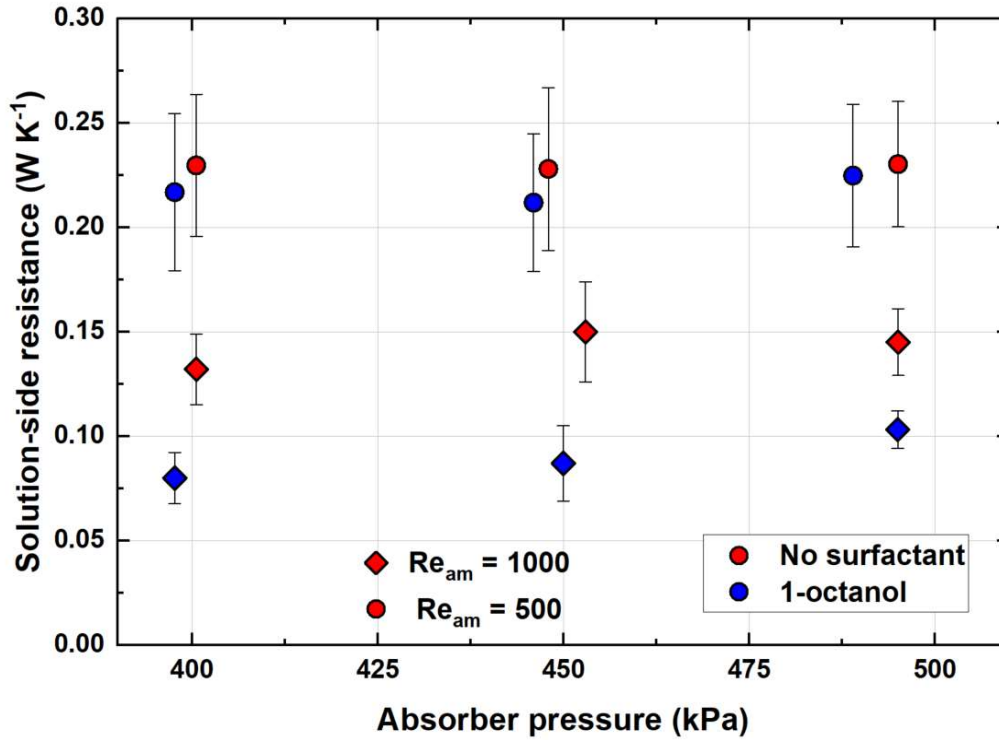


Figure 4.10: Variation of absorber performance with system pressure

4.5 Model development

To further interpret the results observed in the experiments and enable the development of compact, high-performance bubble absorbers, a heat and mass transfer model is developed based on the underlying phenomena and discussed in this section.

Ammonia-water absorption can be modeled as condensation of a zeotropic mixture. Two approaches are commonly used – the equilibrium method and the non-equilibrium method. In the equilibrium approach presented by Silver (1947) and Bell and Ghaly (1973), the pure component heat transfer coefficient is corrected to account for the degradation due

to mass transfer. This approach is computationally inexpensive and can be used when the Lewis number is less than 1. In the present study, the Lewis number is always greater than 25, which makes the equilibrium approach not applicable. In the non-equilibrium approach first presented by Colburn and Drew (1937) and later adapted by Price and Bell (1974), vapor and liquid are assumed to be at equilibrium at the interface, and the resistances for heat and mass transfer from the interface to the individual phases are analyzed individually. This non-equilibrium approach has been shown to provide the best agreement for ammonia-water absorption (Chandrasekaran et al., 2020). Therefore, in the present study, the non-equilibrium approach is used for model development.

The modeling is performed by discretizing the absorber into small segments along the length of the absorber, in which the solution and vapor flow up in a co-current direction while the coupling fluid flows down in the annulus in counter-flow direction (Figure 4.11). The model assumes that the process is in steady-state and there is no direct heat transfer between the vapor and the coupling fluid. The resistance network for heat and mass transfer is shown in Figure 4.12. As discussed in Section 2, there is a 0.05-m mixing section at the entrance of the absorber. Most studies in the literature assume that the two-phase mixture exiting the adiabatic mixing section is in equilibrium (Hoysall and Garimella, 2018). However, it is noted that for all conditions in this study, the mixture is sub-cooled at the exit of the adiabatic mixer. The equilibrium assumption is thus, not valid. Therefore, a non-equilibrium approach is used to model the mixture behavior in the mixing section.

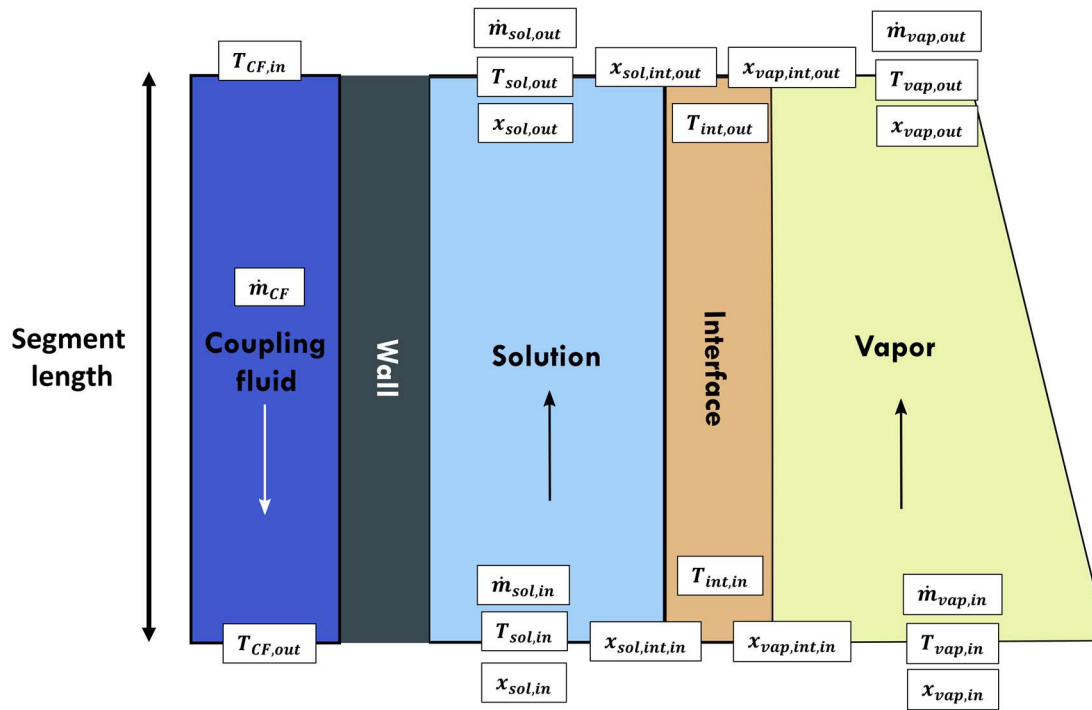


Figure 4.11: Representative segment for the heat and mass transfer

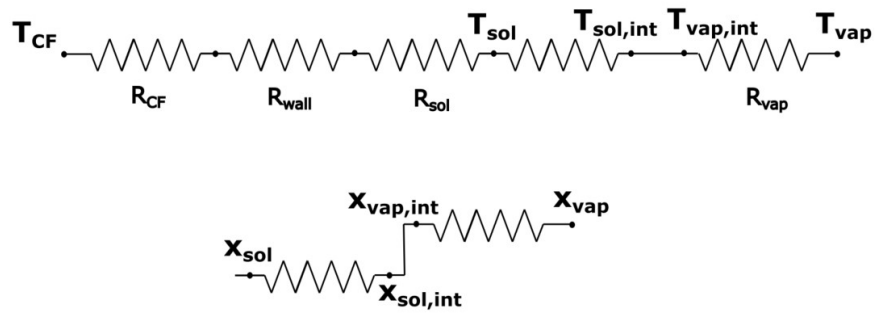


Figure 4.12: Heat and mass transfer resistances for bubble absorber model

The inlet conditions of each segment are determined from the outlet conditions of the previous segment. These include the vapor and solution mass flow rate, temperature, concentration, and pressure. In addition, the interface temperature and concentration for both vapor and solution are determined from the outlet of the previous segment. In each segment, the molar flux of the mass being absorbed is given by

$$\dot{n}_T'' = \beta_{vap} \times C_{vap,T} \times \ln \left(\frac{\tilde{z} - \tilde{x}_{vap,int}}{\tilde{z} - \tilde{x}_{vap,bulk}} \right) \quad (4.10)$$

$$\dot{n}_T'' = \beta_{sol} \times C_{sol,T} \times \ln \left(\frac{\tilde{z} - \tilde{x}_{sol,bulk}}{\tilde{z} - \tilde{x}_{sol,int}} \right) \quad (4.11)$$

where β_{vap} and β_{sol} are the vapor and solution mass transfer coefficients. The third term in Eqs. (4.10) and (4.11) is the driving molar concentration difference, which is a function of the molar concentration of the condensing flux, \tilde{z} , and the molar concentrations of the bulk and interface in each phase. The molar concentration of the condensing flux, z , can be calculated using the expression in Eq. (4.12).

$$\tilde{z} = \frac{\dot{n}_A''}{\dot{n}_A'' + \dot{n}_W''} \quad (4.12)$$

The mass transfer coefficient is calculated using the correlation developed by Akita and Yoshida (1974) shown in Eq. (4.13)

$$\beta_{sol} = \frac{0.5 D_{aw,sol}}{d_B} \left(\frac{\mu_{sol}}{\rho_{sol} D_{aw,sol}} \right)^{0.5} \left(\frac{g d_B^3 \rho_{sol}^2}{\mu_{sol}^2} \right)^{0.25} \left(\frac{g d_B^2 \rho_{sol}}{\sigma} \right)^{\frac{3}{8}} \quad (4.13)$$

This correlation predicted bubble absorber performance well according to a recent study by Ben Jaballah et al. (2019). The vapor-side mass transfer coefficient is determined using the vapor Sherwood number (Sh), which is calculated using the heat and mass transfer analogy. The individual molar fluxes of condensing ammonia and water are calculated using

$$\dot{n}_A'' = \tilde{z} \times \dot{n}_T'' \quad (4.14)$$

$$\dot{n}_A'' = (1 - \tilde{z}) \dot{n}_T'' \quad (4.15)$$

The molecular masses of ammonia (M_A) and water (M_W) are used to calculate the mass of ammonia and water absorbed in each segment.

$$\dot{m}_{abs,A} = \dot{n}_A'' \cdot A_{int} \cdot M_A \quad (4.16)$$

$$\dot{m}_{abs,W} = \dot{n}_W'' \cdot A_{int} \cdot M_W \quad (4.17)$$

Interfacial area (A_{int}) plays a significant role in determining the overall performance of the absorber. The Ozar et al. (2012) correlation, which predicts the interfacial area in upward churn, slug and bubbly flow regimes while accounting for the effect of surface tension is used in this model. The mass and concentration of the vapor at the outlet of the segment are then calculated using Eqs. (4.18) and (4.19)

$$\dot{m}_{vap,out} = \dot{m}_{vap,in} - \dot{m}_{abs,A} - \dot{m}_{abs,W} \quad (4.18)$$

$$x_{vap,out} = \frac{\dot{m}_{vap,in} \cdot x_{vap,in} - \dot{m}_{abs,A}}{\dot{m}_{vap,out}} \quad (4.19)$$

A similar mass and species balance is used to compute the mass flow rate and concentration of the solution at the exit of the segment. The total absorption heat duty is calculated using an energy balance between the solution and vapor streams.

$$\dot{Q}_{abs,seg} = \dot{m}_{vap,in} h_{vap,in} + \dot{m}_{sol,in} h_{sol,in} - \dot{m}_{vap,out} h_{vap,out} - \dot{m}_{sol,out} h_{sol,out} \quad (4.20)$$

Eq. (4.20) accounts for both latent heat of absorption and the sensible cooling of the two streams. The vapor outlet enthalpy is determined from the sensible heat transfer between the interface and the vapor bulk, as shown in Eq. (4.21).

$$\dot{Q}_{vap} = \alpha_{vap} \left(\frac{\phi_T}{1 - e^{-\phi_T}} \right) A_{int} LMTD_{vap} \quad (4.21)$$

The second term in the above equation is the Ackermann factor, which accounts for heat transfer in the presence of mass transfer. The logarithmic mean temperature difference is calculated between the temperatures at the vapor bulk and the interface. The sensible heat transfer calculated here is used to determine the temperature of the vapor at the exit of the segment.

$$\dot{Q}_{vap} = \dot{m}_{vap} c_{p,vap} (T_{vap,in} - T_{vap,out}) \quad (4.22)$$

The total absorption heat duty can also be expressed using Eqs. (4.23) and (4.24), which are used to calculate the coupling fluid outlet and solution outlet temperatures.

$$\dot{Q}_{abs,seg} = \dot{m}_{CF} c_{p,CF} (T_{CF,seg,out} - T_{CF,seg,in}) \quad (4.23)$$

$$\dot{Q}_{abs,seg} = (UA_{abs})_{seg} LMTD_{seg} \quad (4.24)$$

The LMTD is calculated between the solution bulk and coupling fluid temperatures. The UA of the segment is determined using the resistance network shown in Figure 11.

$$(UA_{abs})_{seg} = \frac{1}{R_{tot,seg}} = \frac{1}{R_{sol,seg} + R_{CF,seg} + R_{wall,seg}} \quad (4.25)$$

The coupling fluid and wall segmental resistances are calculated as shown in Section 3, using the appropriate segment length. The solution resistance, $R_{sol,seg}$, is determined using Eq. (4.26)

$$R_{sol,seg} = \frac{1}{\alpha_{sol} A_{seg}} \quad (4.26)$$

where α_{sol} is the solution heat transfer coefficient. For condensation in upward flow, Lips and Meyer (2012) conducted experiments and compared their results with the predictions from existing correlations. Their results showed that the correlation of Shah (1979) is most suitable for upward condensing flows. Therefore, in this study, the solution heat transfer coefficient is determined using the correlation of Shah (1979).

The solution outlet temperature is determined as the average of the wall temperature and the interface temperature.

$$T_{sol,out} = \frac{T_{wall,out} + T_{int,out}}{2} \quad (4.27)$$

The wall temperatures can be estimated by using the resistance network as shown in Fig and evaluating the $LMTDs$ between the solution and the wall ($LMTD_{sol}$), and the wall and the coupling fluid ($LMTD_{CF}$) (Nagavarapu, 2012).

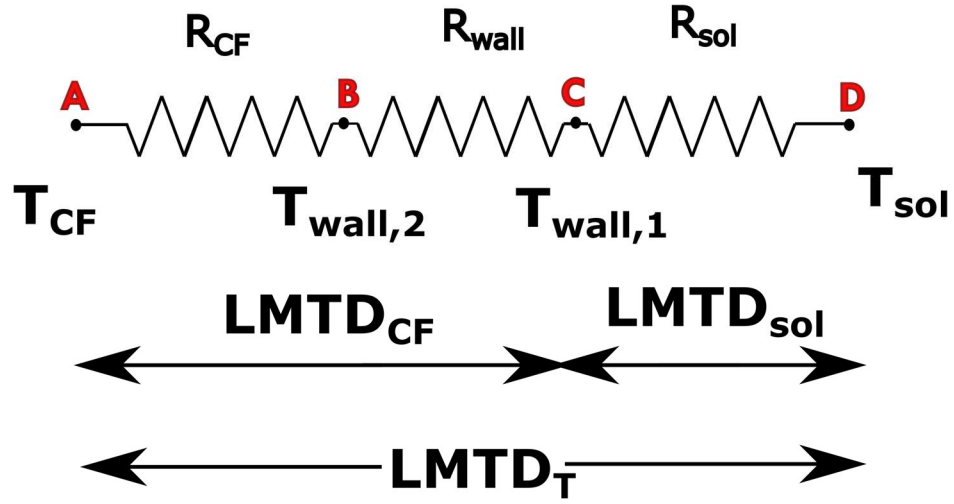


Figure 4.13: Resistance network for determining wall temperatures

The absorber heat duty can also be calculated using these LMTDs as

$$\dot{Q}_{abs,seg} = \alpha_{sol} A_{seg} LMTD_{sol} \quad (4.28)$$

$$\dot{Q}_{abs,seg} = (U_{CF-wall}) A_{seg} LMTD_{CF} \quad (4.29)$$

where $LMTD_{sol}$ and $LMTD_{CF}$ are defined as shown in (4.30) and (4.31), respectively.

$$LMTD_{sol} = \frac{(T_{sol,in} - T_{wall,1,in}) - (T_{sol,out} - T_{wall,1,out})}{\ln \left[\frac{(T_{sol,in} - T_{wall,1,in})}{(T_{sol,out} - T_{wall,1,out})} \right]} \quad (4.30)$$

$$LMTD_{CF} = \frac{(T_{wall,2,in} - T_{CF,out,seg}) - (T_{wall,2,out} - T_{CF,in,seg})}{\ln \left[\frac{(T_{wall,2,in} - T_{CF,out,seg})}{(T_{wall,2,out} - T_{CF,in,seg})} \right]} \quad (4.31)$$

The governing equations for one segment are now defined. The solution to this system of equations provides all the outlet properties and flow rates for the solution and the vapor, and the inlet temperature of the coupling fluid. Engineering Equation Solver (Klein, 2018) is used to iteratively solve this system of equations for each segment. In the mixing section, the heat transfer coefficient of the coupling fluid (α_{CF}) is set to zero, because this section is adiabatic. It must be noted that once the value of vapor flow rate is close to zero near the outlet of the absorber, the model switches to a single-phase heat exchanger configuration to compute the sensible cooling of the concentrated solution by the coupling fluid. The ϵ -NTU method is then used to obtain the exit temperature (Incropera et al., 1996).

When surfactants are introduced in the absorber, two key changes are made to the heat and mass transfer model. First, the liquid-side mass transfer coefficient is enhanced. This is calculated using the model presented by Sardeing et al. (2006).

$$\beta_{sol,surf} = 1.744K^{-0.084}\beta_{sol} \quad (4.32)$$

where K is the adsorption equilibrium constant of the surfactant. Experimental validation of the Sardeing et al. (2006) model for CO₂ absorption in aqueous solution is presented in García-Abuín et al. (2010). They also discuss the method to determine the adsorption equilibrium constant for different surfactants. The second modification made to the model is the value of surface tension. Experimental results from Kini and Garimella (2021) are used in the calculation of interfacial area. The Ozar et al. (2012) model for determining interfacial area is based on the two-group approach of Ishii and Mishima (1980) where the interfacial area is inversely proportional to the Laplace length (Lo).

$$Lo = \sqrt{\frac{\sigma}{g\Delta\rho}} \quad (4.33)$$

The addition of surfactants leads to a reduction of the surface tension (σ), resulting in reduction of Laplace length and bubble diameters. Smaller bubbles have a larger surface area, which enhances overall mass transfer. Sample calculations for a representative segment in the bubble absorber are shown in Appendix B.

4.6 Model results

4.6.1 Adiabatic section

The results from the heat and mass transfer model described in the previous section are discussed here. A representative case with water inlet temperature (T_{sol}) of 30.3°C, ammonia inlet temperature (T_{vap}) of 29.8°C, water mass flow rate (\dot{m}_{sol}) of 1.20×10^{-3} kg s⁻¹, and ammonia mass flow rate (\dot{m}_{sol}) of 0.05×10^{-3} kg s⁻¹ is considered. The inlet of the absorber consists of an adiabatic mixing section in which the solution and the vapor mix and exit this section as a two-phase mixture. A thermocouple measures the temperature of this mixture at the exit of the mixing section. As the model predicts the vapor and solution temperatures separately, the temperature measured by the thermocouple at the exit is predicted by using a volumetric average of the vapor and liquid temperatures.

$$T_{weighted} = \frac{\dot{V}_{vap}T_{vap} + \dot{V}_{sol}T_{sol}}{\dot{V}_{vap} + \dot{V}_{sol}} \quad (4.34)$$

where \dot{V} is the volumetric flow rate of individual phases. The temperature profiles of the vapor, solution, and the interface in the 0.05-m adiabatic section are shown in Figure 4.14.

Although this section is adiabatic, a small fraction of ammonia is absorbed into the solution. The latent heat released by the condensation of ammonia results in a sudden increase in the temperature of the solution as there is no heat rejected to the coupling fluid. The vapor is heated due to the temperature difference between the vapor bulk and the interface. The weighted temperature, $T_{weighted}$, closely follows the vapor temperature due to the large volumetric flow rate of the vapor. The molar concentration of the condensing flux (\tilde{z}) is always greater than 1 for all cases in the adiabatic section, indicating there is some desorption of water from the solution to the vapor bulk. An appreciable fraction of the ammonia vapor (7.3%) is absorbed in the mixing section. The difference between the measured and predicted temperatures is $< 1^\circ\text{C}$.

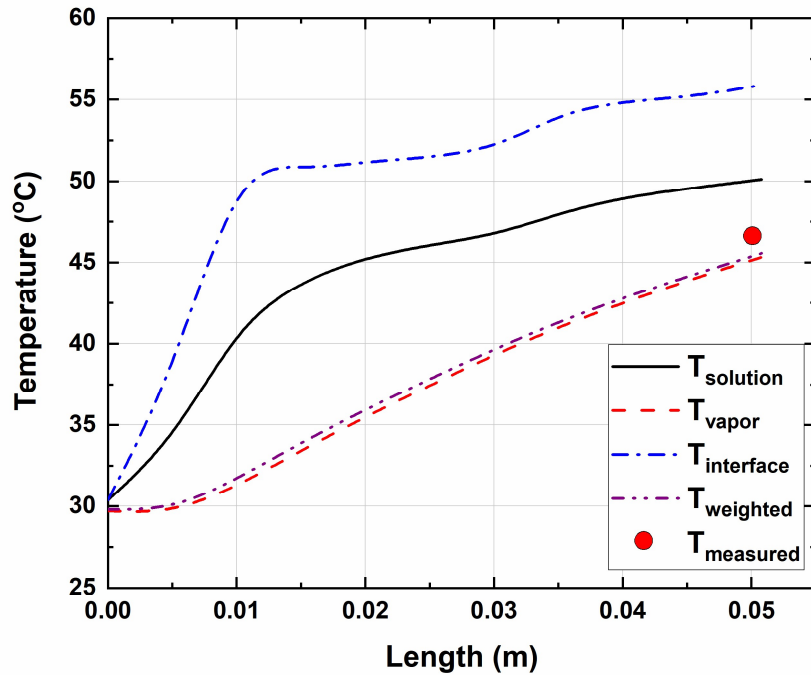


Figure 4.14: Temperature profiles in the adiabatic mixing section

4.6.2 Heat transfer section

The temperature profiles of solution, vapor, and the coupling fluid stream over the entire length of the absorber are shown in Figure 4.15. The absorption section begins at the end of the adiabatic section and is characterized by heat transfer to the coupling fluid. The solution is sensibly cooled by transferring heat to the coupling fluid while the vapor gains heat from the interface. About 70% of the absorption section is in the slug/churn flow regime and the rest is in the bubbly regime. When the ammonia vapor is completely absorbed, the program switches to the subcooling analysis using the ε -NTU method. The solution temperature decreases linearly in this section. The predicted heat duty of 76.6 W compares well with 78.3 W of heat duty measured using the coupling fluid data.

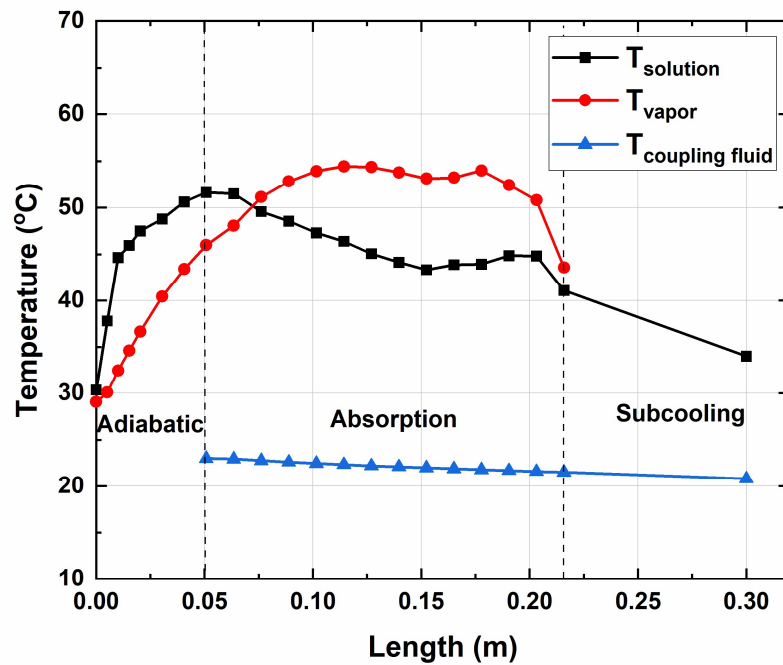


Figure 4.15: Temperature profiles along the entire length of the absorber

The impact of adding 1-octanol is discussed next. Figure 4.16 shows the temperature profiles of both the vapor and the solution along the length of the absorber. When surfactants are added, the mass transfer coefficient is enhanced by 1.15-1.8 times, and the interfacial area is enhanced by 9-26%. Figure 4.17 compares the interfacial area concentration with and without the addition of surfactants. At the inlet of the absorber, the flow is in the churn regime and the surfactants result in ~10% enhancement. As absorption progresses, the flow transitions to slug flow and the interfacial area decreases due to the reduction of Group-1 or small diameter bubbles. As the flow transitions to bubbly flow, the interfacial area increases again with the highest enhancement (~25%) due to surfactants observed in this flow regime, which leads to an overall increase in mass transfer. Finally, a drastic reduction in the interfacial area is observed due to the sharp decrease in the mass

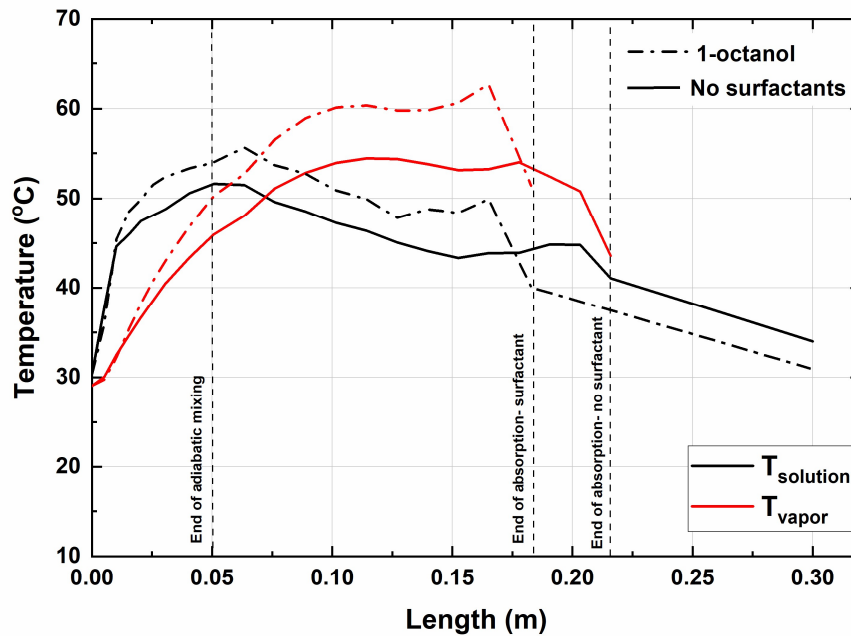


Figure 4.16: Comparison of temperature profiles with and without surfactant

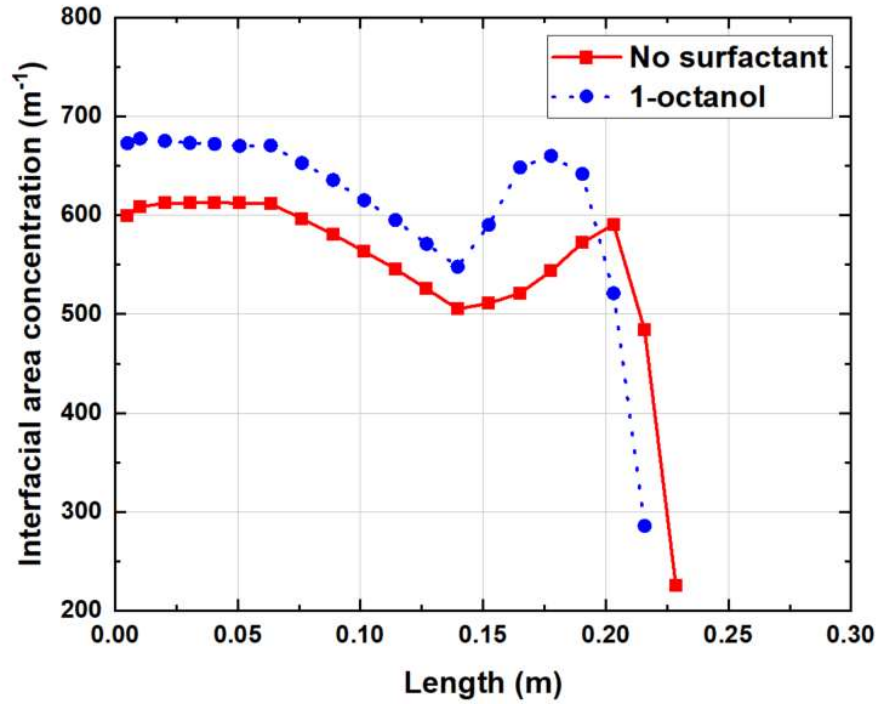


Figure 4.17: Comparison of interfacial area concentration with and without surfactant

flow rate of the vapor. In the adiabatic section, 11% of the ammonia is absorbed as compared to 7.3% in the baseline case. At the end of the adiabatic section, the solution temperature is thus higher with the addition of surfactants. This also leads to a larger temperature gradient at the inlet of the absorption section, resulting in higher heat duties in the first few segments of the absorber.

A comparison of the heat duties and mass flow rates of liquid and vapor for both the surfactant and baseline case is presented in Figure 4.18. The mass flow rate of the solution increases whereas the mass flow rate of the vapor decreases along the height of the absorber. The end of the absorption section is determined when the flow rate of vapor

is zero. When surfactants are not used, 0.22 m of the component is used for absorption and the rest is used for subcooling the solution. The addition of surfactants results in an 18% reduction of absorption length to 0.18 m. This makes a larger area available for subcooling, thus lowering the temperature of the solution at the exit of the absorber. This representative case demonstrates that the absorber size can be reduced by 18% due to the passive enhancement from the addition of surfactants. At higher flow rates of the working fluids, the reduction in absorption length is $> 25\%$.

The heat and mass transfer model is validated by comparing the total heat duty (absorption + subcooling) predicted by the model with the coupling fluid heat duty reported from experiments described in Section 4. Figure 4.19 shows a comparison between the

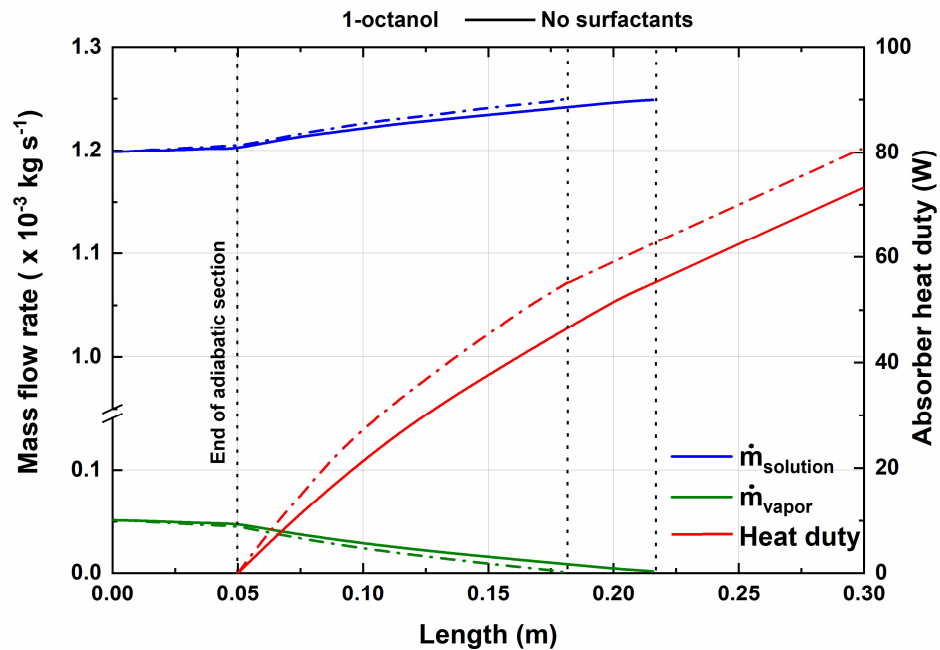


Figure 4.18: Comparison of mass flow rates and heat duty with and without surfactant

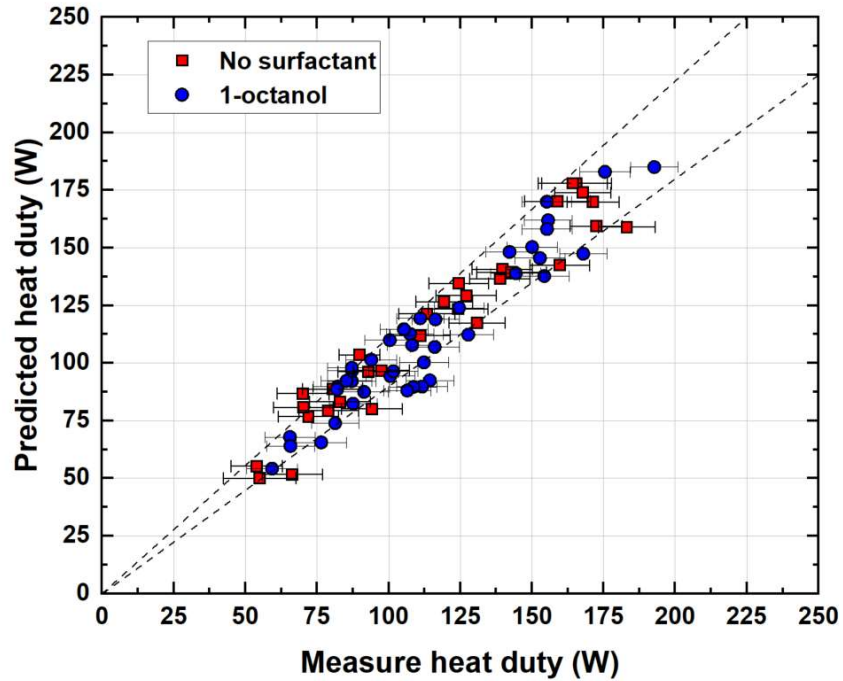


Figure 4.19: Comparison between predicted and measured absorber heat duties

measured and predicted heat duties for both cases with and without the addition of surfactants. For more than 80% of the data points, the predicted heat duties are within 10% of the experimental values. The absolute average deviation (AAD) is 8.3%, indicating good agreement between the model predictions and experimental values.

4.7 Conclusions

The effect of surfactants on ammonia-water bubble absorption is systematically investigated. An experimental facility is developed, and absorber heat duties are measured for different working fluid flow rates, coupling fluid temperatures, and surfactant concentrations. In the bubble mode, the dominant resistance is the mass transfer resistance on the liquid side due to the poor diffusivity of ammonia in the liquid phase. The addition

of surfactant improves the mass transfer coefficient and the interfacial area, both of which contribute to lowering the mass transfer resistance. It was also observed that optimal performance was achieved at surfactant concentrations between 300 PPM and 500 PPM. Further addition of surfactant diminished absorber performance due to the “barrier effect”. A segmented heat and mass transfer model based on the non-equilibrium approach is developed, and the key trends in the temperature and mass flow rate profiles are discussed. Using surfactants can lead to ~25% reduction in absorber size, thus helping reduce overall system footprint, cost, and fluid inventory. The experimental results along with the data analysis and modeling framework developed in the present study will aid the development of compact and high-heat flux heat and mass exchangers

CHAPTER 5. EFFECT OF SURFACTANTS ON PERFORMANCE OF FALLING-FILM ABSORBERS

This chapter discusses the effects of surfactants on the performance of a vertical falling-film absorber. Experiments are performed in a two-pressure facility that closely simulates an absorption heat pump. The effects of surfactants on the performance of other components in the system are also investigated².

5.1 Introduction

The use of energy for space cooling is growing faster than for any other end-use in buildings and consumes more than 2000 terawatt-hours (TWh) of electricity each year (IEA, 2018). This demand for space cooling is already putting enormous strain on existing electricity infrastructure in many countries, as well as driving up emissions. Thermally-driven vapor absorption systems are recognized as a viable alternative to electricity-driven vapor compression based systems (Xu and Wang, 2016). The ability to use low-grade thermal energy and environmentally benign working fluids is a critical feature of vapor absorption systems (Staedter and Garimella, 2018b). However, the use of these systems has been limited to large capacity installations due to their bulky footprint. Advances in compact heat and mass exchanger development have led to miniaturized absorption systems for small-capacity residential and transportation applications (Determan and Garimella, 2012; Altamirano et al., 2020). Compact absorption systems using ammonia-

² This chapter is adapted from : Kini, G., Chandrasekaran, S., Hughes, M., Garimella, S., Experimental investigation of surfactant enhanced ammonia-water absorption in a shell-and-tube absorber, International Journal of Refrigeration (2021), DOI: <https://doi.org/10.1016/j.ijrefrig.2021.04.034>

water working fluids have been demonstrated for cooling capacities ranging from 300 W to 10.5 kW (Garimella et al., 2016; Goyal et al., 2017; Jiménez-García and Rivera, 2019; Kini et al., 2020).

The key component of absorption systems is the absorber, where the ammonia refrigerant recombines with dilute solution in a coupled heat and mass transfer process (Amaris et al., 2018). The performance of the absorber often limits the performance of the overall system (Hoysall and Garimella, 2019), and can also be the largest component in the system, thereby dictating system size. Passive intensification techniques in the absorber allow for its size to be decreased and can lower the cycle driving temperature in solar or low grade thermal energy-driven applications. These techniques typically include the use of rough or extended surfaces or the inclusion of small quantities of additives or nanoparticles in the working fluids to improve the heat and mass transfer. A detailed review of advanced surface designs and mechanical treatments employed in absorbers is presented by Amaris et al. (2018).

Surface-active agents or surfactants are used to enhance heat and mass transfer in many interfacial processes by inducing interfacial turbulence at the liquid-vapor interface (Bergles and Manglik, 2013). Absorbers typically operate in either the falling-film or the bubble/forced convection configuration. While surfactants lead to an increase in the mass transfer coefficient in all cases, there are secondary effects that are dependent on the configuration. In the bubble configuration, surfactants affect the interfacial area and bubble dynamics due to the reduction in surface tension (Takagi and Matsumoto, 2011). In the falling-film configuration, surfactants improve wettability and lead to higher utilization of the available transfer area (Kang et al., 2007). The effects of surfactants can also be

dependent on the film Re of falling films. At high Re with turbulent falling films, surfactants can have a stabilizing effect on interfacial waves and reduce mass transfer coefficients. However, at typical conditions in an absorber, film Re is in the laminar regime and surfactants enhance the mass transfer coefficient by formation of rivulets in the flow (Hihara and Saito, 1993).

The enhancement caused by surfactants in absorbers was first reported by Kashiwagi (1988). Surfactants have been widely studied in water-LiBr absorption systems (Hihara and Saito, 1993; Hoffmann et al., 1996; Kim et al., 1996; Nakoryakov et al., 2008; Fu Lin and Shigang, 2011), while there are only a handful of studies that consider surfactants in ammonia-water systems. Möller and Knoche (1996) investigated the effect of surfactants on ammonia-water absorption in a falling-film offset-strip fin absorber. Kim et al. (2006) performed flow visualization during ammonia-water bubble absorption in the presence of surfactants. They showed that surfactants affect bubble size and their coalescence behavior. Kim et al. (2007b) studied the performance enhancement in an ammonia-water bubble absorber by adding surfactants and nano-particles. They concluded that both surfactants and nano-particles improve absorption performance and derived correlations for enhancement factors for different surfactants. Hoysall and Garimella (2019) investigated the effect of surfactants in microchannel absorbers and observed that the apparent heat transfer co-efficient improved by 20-40%.

All these studies were performed in a single-pressure system with pure ammonia as the refrigerant whereas in real systems, the refrigerant vapor generated has a trace amount of water that significantly affects the heat and mass transfer process in the absorber. Except for Hoysall and Garimella (2019), other investigations did not include a coupling fluid loop

to reject the heat generated during absorption. In addition to this, the concentrations of the dilute and concentrated solutions, the absorber pressure, and other operating conditions used were not representative of conditions experienced in a vapor absorption heat pump. Although the physics of absorption enhancement due to surfactants has been discussed since their introduction in the 1980s, the mechanism of action in representative geometry and conditions, and the effect of surfactants on other components of the system needs to be examined.

Chapter 2 presented a modeling approach to predict the impact of surfactants on the performance of a shell-and-tube ammonia-water absorber. In this chapter, experimental investigations are performed to understand the effect of surfactants on the performance of a shell-and-tube absorber in a two-pressure facility across a wide range of representative operating conditions. The absorber is designed for a 10.5 kW cooling capacity absorption chiller operating at elevated ambient temperatures as high as 45°C (Kini et al., 2020). In addition, the effect of surfactants on other components in the system, including the desorber, is discussed.

5.2 Experimental approach

A vertically oriented, baffled, shell-and-tube absorber with ammonia-water mixture on the shell-side and coupling fluid on the tube-side is used (Figure 5.1). The ammonia-water solution flows on the shell side to mitigate potential maldistribution associated with the two-phase flow through the tube side of the heat exchanger. The absorber is operated in the co-current flow configuration in which the dilute solution and the vapor entering the absorber are pre-mixed upstream of the absorber in a mixing section. This pre-mixed

solution/vapor mixture then enters from the top of the absorber and flows downwards. The coupling fluid on the tube side flows from the bottom to the top of the absorber. Twenty one baffles are included in the design to guide the flow of ammonia-water. Each baffle is provided with a lip to aid the accumulation of ammonia-water mixture to form a solution pool. This pool contributes to the interfacial area between the solution and vapor. The openings in these baffles through which the tubes pass is larger than the diameter of the tube. This allows for the solution from the pool to drip down as a falling-film along the length of the tubes. The small tube size also provides high heat transfer coefficients on the coupling fluid side, decreasing the overall heat transfer resistance. In addition, the tight baffle- and tube-spacing force a serpentine flow path and increase the interfacial area available for heat and mass transfer in the working fluid. The key dimensions of the absorber are shown in Table 5.1. Additional details of the absorber geometry, construction, and flow configuration are presented in Chandrasekaran et al. (2020).

Table 5.1: Absorber geometry details

Parameter	Value
Shell D_o (m)	0.152
Shell D_i (m)	0.147
Tube D_o (mm)	3.175
Tube D_i (mm)	2.159
Tube Pitch-to-Diameter Ratio (-)	1.325
Tube Count (-)	955
Baffle Count (-)	21
Nominal Baffle Spacing (mm)	38
Baffle Cut (%)	22.6
Total Length (m)	0.950
Total Shell-side Surface Area (m ²)	7.925

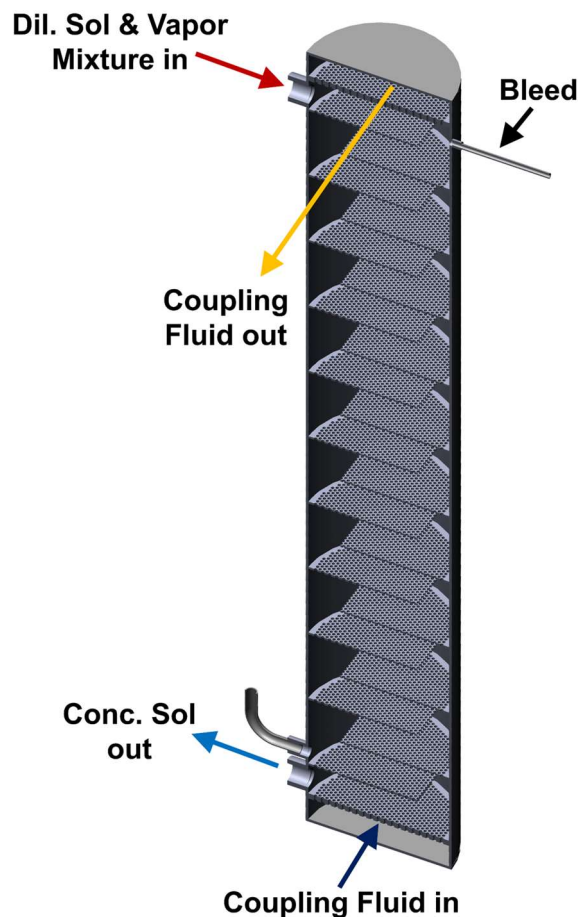


Figure 5.1: Shell-and-tube absorber schematic

A two-pressure facility consisting of a desorber, rectifier, absorber, solution heat exchanger, and valves is fabricated (Figure 5.2). Concentrated solution entering the top of the desorber and flowing downwards is heated by Paratherm NF, a heat transfer oil. A WATLOW 25 kW electric circulation heater is used in conjunction with a PID controller to provide accurate control over the temperature of oil entering the desorber. This heat addition generates vapor, which leaves through the top of the desorber. A diabatic distillation column design is used for the desorber and the desorption temperature is chosen

to optimize the thermodynamic efficiency of the component (Staedter and Garimella, 2018a). Since the vapor leaving the desorber has a sizeable mass fraction of water, the vapor is cooled in the rectifier to condense as much water out of the vapor as possible, which yields ammonia vapor mass fraction values typical of absorption chiller operation. The vapor then flows through an expansion valve, which decreases its pressure and

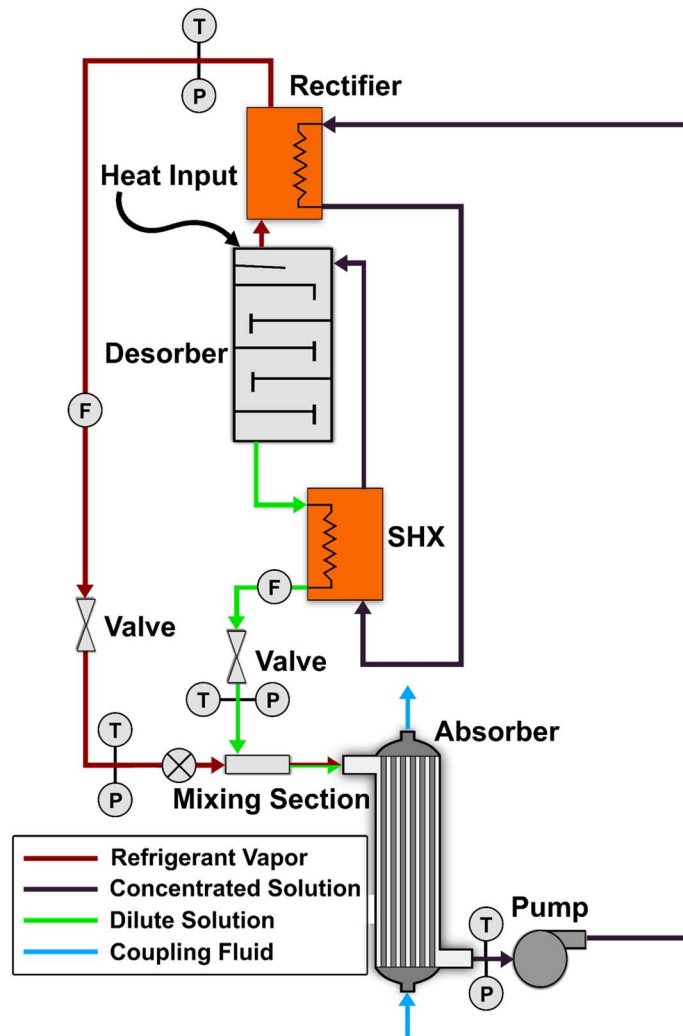


Figure 5.2: Experimental facility

temperature and enters the mixing section. In the mixing section, vapor and dilute solution from the desorber reach equilibrium before reaching the absorber. In the absorber, the zeotropic liquid-vapor mixture fully condenses and exits to the solution pump to complete the cycle. The heat of absorption is rejected to a coupling fluid loop in which the inlet volumetric flow rate and temperature are controlled. The solution heat exchanger (SHX) is a recuperative heat exchanger that pre-heats the concentrated solution, and likewise, cools the dilute solution before entering the mixing section. A photograph of the experimental facility is shown in Figure 5.3.

The valves and pump speed are adjusted during system operation to obtain the desired operating conditions. Temperature, pressure, and flow rate are measured at different points in the loop as shown in Figure 2 to determine the operating conditions. Table 5.2 lists the details of the measuring instruments in the experimental facility. The

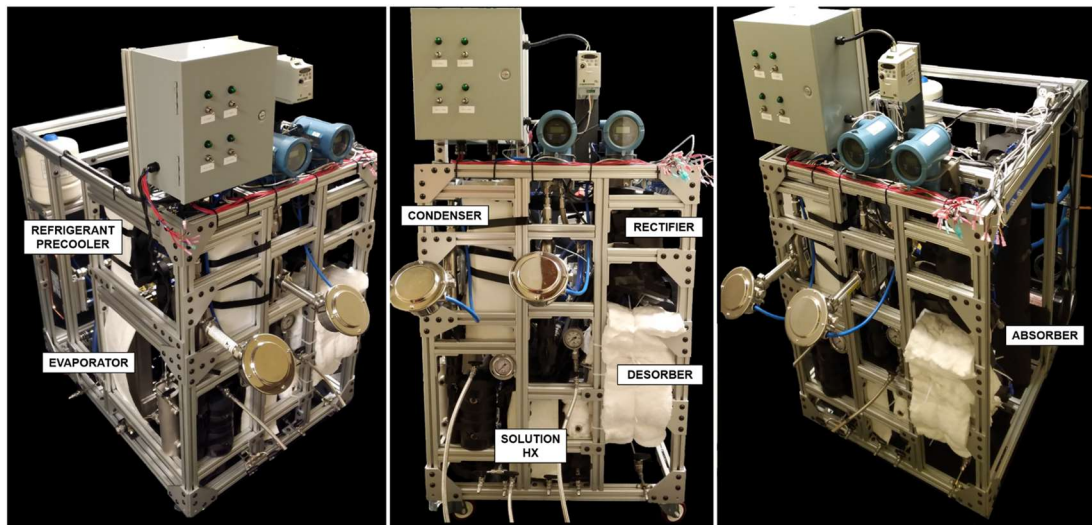


Figure 5.3: Photograph of experimental facility

key parameters affecting the absorber performance, including the solution and vapor flow rates and coupling fluid inlet temperature, are varied. The test matrix is shown in Table 5.3. The effect of surfactants is assessed by repeating the experiments with and without surfactants. For each data point in the test matrix, data are collected for 20 minutes and averaged to remove the effects of transient perturbations. Additional details of the experimental procedure followed during testing are presented in Chandrasekaran et al. (2020).

Table 5.2: Instrumentation specification in the facility

Instrument	Manufacturer/Model	Range	Accuracy
Thermocouple	Omega® T-type	-250-300 °C	±0.5 °C
Pressure Transducer	Omega® 4-20mA Output absolute	0-1034.2 kPa 0-3447.3 kPa	±0.03% of full scale
Mass flow sensor	Micromotion CMFS	0-110 kg/hr	±0.1 % of reading
Solution pump	Hydracell P200	-	-
Electronic valves	Carel E2V series	480 steps	-
Heater controller	Watlow PM series	-	-

Table 5.3: Test matrix for falling-film experiments

1-octanol concentration	Solution Flow Rate ($\times 10^{-3} \text{ kg s}^{-1}$)	Vapor Mass Fraction (-)	Coupling Fluid Flow Rate ($\times 10^{-3} \text{ m}^3 \text{ s}^{-1}$)	Coupling Fluid Inlet Temperature (°C)
0 PPM	24	0.25	0.32	35, 40, 45
	32			
500 PPM	24	0.25	0.32	35, 40, 45, 50
	32			
2000 PPM	32	0.25	0.32	35, 40, 45, 50

5.3 Data reduction

5.3.1 State point determination

Thermodynamic state point determination for this experimental facility is provided in Chandrasekaran et al. (2020). The key details of this procedure are summarized here. The thermodynamic properties of ammonia-water solution in the liquid and vapor phases are obtained from Engineering Equation Solver (Klein, 2018). The binary mixture of ammonia and water requires three independent properties to fully define its state at any point in the experimental facility. Direct measurements of temperature and pressure at several points in the loop serve as two of these three independent properties. Direct measurement of concentration is not practical due to the difficulty in obtaining samples in small capacity closed systems and the high uncertainty associated with concentration

measurement. Thus, appropriate assumptions about the expected quality at certain locations are made to fix the state points. First, the vapor leaving the rectifier is assumed to be saturated. This fixes the concentration at that point, which is the same as the concentration of the vapor entering the absorber. Second, the solution at the outlet of the absorber is assumed to be subcooled. The degree of subcooling is determined by performing an energy balance between the coupling fluid and working fluid heat duties. It is observed from Figure 5.4 that a subcooling of 2 K provides the best agreement between the working and coupling fluid heat duties.

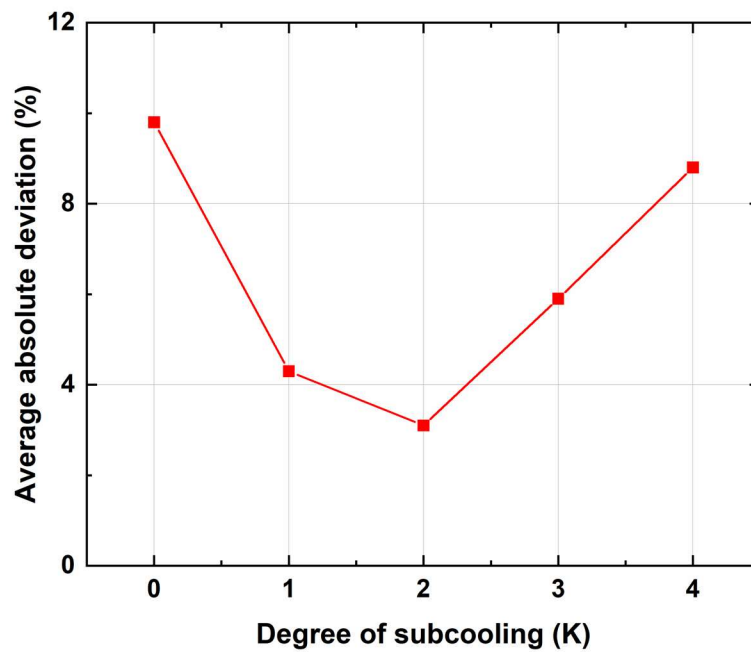


Figure 5.4: Error versus assumed degree of subcooling

The subcooling assumption at the absorber outlet and pressure and temperature measurements are used to determine the ammonia mass fraction of the concentrated solution as shown in Eq. (5.1)

$$x_{abs,conc,out} = x(T_{abs,conc,out} + \Delta T_{subcool}, P_{abs,conc,out}, q = 0) \quad (5.1)$$

Mass and species balance are conducted across the absorber to calculate the concentrated solution flow rate and the dilute solution concentration as shown in Eqs. (5.2) and (5.3), respectively.

$$\dot{m}_{conc} = \dot{m}_{vap} + \dot{m}_{dil} \quad (5.2)$$

$$x_{abs,dil,in} = \frac{x_{abs,conc,out} \dot{m}_{conc} - x_{abs,vap,in} \dot{m}_{vap}}{\dot{m}_{dil}} \quad (5.3)$$

From these calculations, the properties of the fluids entering the mixing section are fixed. The mixing section is modeled as an adiabatic control volume, which results in an equilibrium solution temperature entering the absorber using Eqs. (5.4) and (5.5). The solution pressure is taken to be an average of the pressures of the incoming streams.

$$\dot{m}_{vap} h_{abs,vap,in} + \dot{m}_{dil} h_{abs,dil,in} = \dot{m}_{conc} h_{abs,sol,in} \quad (5.4)$$

$$T_{abs,sol,in} = T(P_{abs,sol,in}, h_{abs,sol,in}, x_{abs,conc,out}) \quad (5.5)$$

The log mean temperature difference (*LMTD*) of the absorber is calculated using Eq. (5.6). The heat duty of the absorber is calculated by using the measured flow rate and temperatures of the coupling fluid as shown in Eq. (5.7)

$$LMTD_{abs} = \frac{(T_{abs,sol,in} - T_{abs,cf,out}) - (T_{abs,conc,out} + \Delta T_{subcool} - T_{abs,cf,in})}{\ln \left[\frac{(T_{abs,sol,in} - T_{abs,cf,out})}{(T_{abs,conc,out} + \Delta T_{subcool} - T_{abs,cf,in})} \right]} \quad (5.6)$$

$$\dot{Q}_{abs} = (\dot{m}c_p)_{cf} (T_{abs,cf,out} - T_{abs,cf,in}) \quad (5.7)$$

The performance of the absorber is quantified using the overall conductance (UA) of the heat exchanger. The UA - $LMTD$ method is used to determine the UA of the absorber as shown in Eq. (5.8).

$$UA_{abs} = \frac{\dot{Q}_{abs}}{LMTD_{abs}} \quad (5.8)$$

5.3.2 Heat transfer resistance network

An equivalent resistance network shown in Figure 5.5 is used to gain insights into the local transport processes. There are two key features in this network. First, most of the heat transfer occurs through the liquid films as the solution falls in the absorber. The film heat transfer coefficient in this case is calculated using the Nusselt (1916) theory. Second, partial wetting of tubes is accounted for by using the wetting ratio, ϕ . The film heat transfer coefficient and wetting ratio are calculated by solving Eqs. (5.9) and (5.10), iteratively. Due to the large number of tubes, the coupling fluid flow remains laminar for the entire range of flow rates investigated in the present study and therefore, a constant Nusselt number of 4.364 is used to calculate the heat transfer coefficient for the coupling fluid.

$$\alpha_{film} = \frac{k_{sol}}{\delta} = k_{sol} \left(\frac{g \rho_{sol} (\rho_{sol} - \rho_{vap}) \pi d_0 \phi}{3 \mu_{sol} \dot{m}_{avg}} \right) \quad (5.9)$$

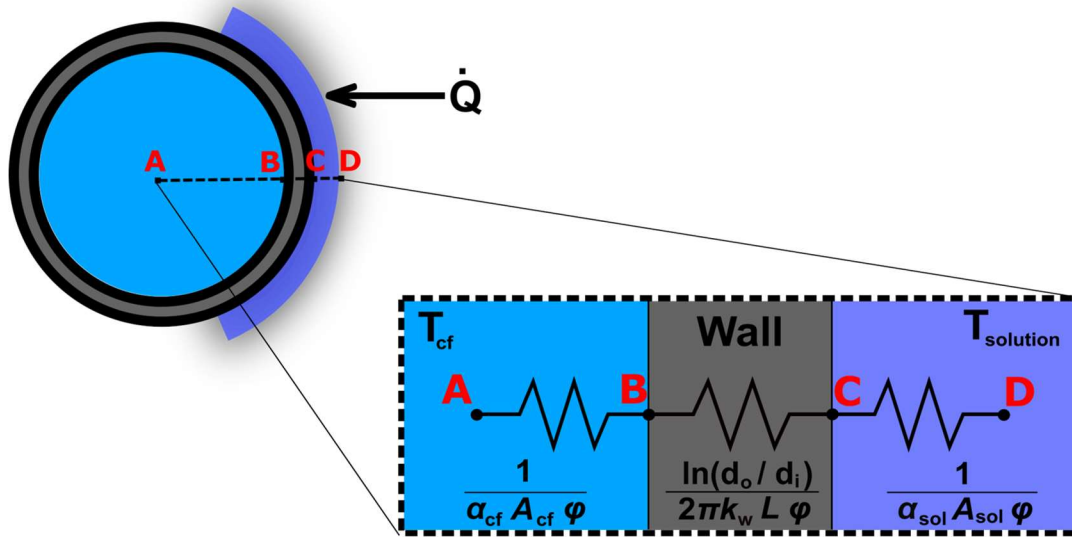


Figure 5.5: Thermal resistance network

$$\frac{1}{UA_{abs}} = \frac{1}{\alpha_{film} A_{wf, wet} \phi} + \frac{1}{\alpha_{cf} A_{cf, wet} \phi} + \frac{\ln\left(\frac{d_o}{d_i}\right)}{2\pi k_{tube} L \phi} \quad (5.10)$$

The desorber heat duty is calculated using the measured temperatures and flow rate of the Paratherm NF flowing on the coupling side.

$$\dot{Q}_{des} = (\dot{m} c_p)_{para} (T_{para, in} - T_{para, out}) \quad (5.11)$$

The overall conductance UA of the desorber is calculated as shown in Eqs. (5.12) and (5.13). The desorber UA and the normalized energy input (\tilde{E}_{des}) shown in Eq. (5.14) are used to quantify the effect of surfactants on desorber performance.

$$LMTD_{des} = \frac{(T_{cf,out} - T_{des,conc,in}) - (T_{cf,in} - T_{des,dil,out})}{\ln \left[\frac{(T_{cf,out} - T_{des,conc,in})}{(T_{cf,in} - T_{des,dil,out})} \right]} \quad (5.12)$$

The solution temperatures and coupling fluid temperatures are used to calculate the log mean temperature difference for the desorber. This definition of LMTD without including the vapor temperature is consistent with the literature (Staedter and Garimella, 2018a).

$$UA_{des} = \frac{\dot{Q}_{des}}{LMTD_{des}} \quad (5.13)$$

$$\tilde{E}_{des} = \frac{\dot{Q}_{des}}{\dot{m}_{vap}} \quad (5.14)$$

5.4 Results

Figure 5.6 compares the coupling and working fluid heat duties and it is observed that ~88% of working fluid heat duties are within 5% of the coupling fluid duties. The absolute average deviation (AAD) is 2.7%. This close agreement between the calculated and measured heat duties demonstrates the validity of the assumptions made in the data reduction procedure.

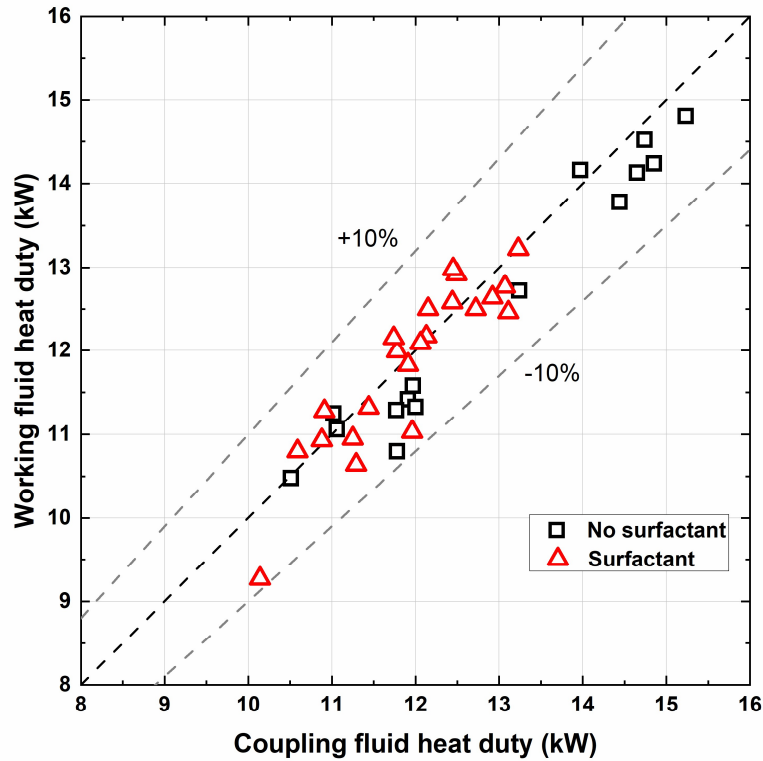


Figure 5.6: Heat duty balance between coupling and working fluids

5.4.1 Effect on absorber performance

A concentrated solution flow rate of $32 \times 10^{-3} \text{ kg s}^{-1}$ with a vapor mass fraction of 0.25 is used for all the test points in Figures 5.7-5.9. Figure 5.7 shows the variation in absorber UA at different concentrations of surfactant (no surfactant, 500 PPM, and 2000 PPM) as the coupling fluid temperature is varied. The UA is enhanced by up to 23% by the addition of surfactants. The addition of surfactants beyond 500 PPM did not produce any further enhancement as the calculated UA values are within experimental uncertainties. This validates the finding of Kini and Garimella (2019) that suggests the use of 500 PPM of hydrocarbon alcohols at which the surface tension value plateaus, and there is no

reduction in surface tension beyond 500 PPM of surfactant. This surface tension reduction initiates interfacial turbulence and leads to an increase in mass transfer at the interface. While improved mass transfer is the leading cause for enhancement in absorption, the increase in heat and mass transfer area due to improved wetting in the absorber results in additional enhancement. The model developed in Chapter 2 predicted UA enhancement in the range of 26-33% by the addition of 500 PPM of 1-octanol due to these two effects. The overprediction by the model compared to experimental results obtained in this study can be attributed to assuming ammonia vapor is pure, neglecting mass transfer resistance on the vapor side, and the use of much lower coupling fluid temperature in the model.

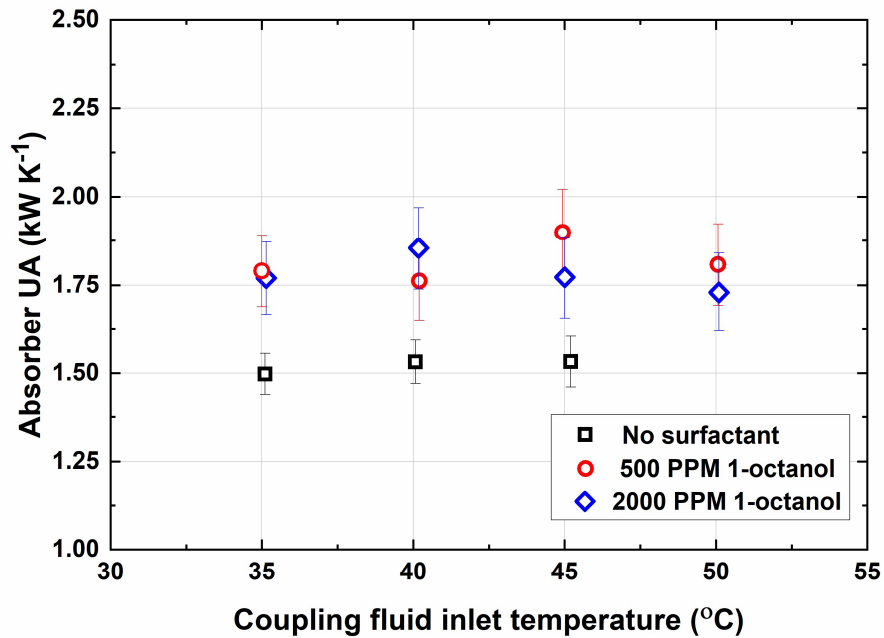


Figure 5.7: Variation of absorber UA with coupling fluid inlet temperature

Figure 5.8 shows the effect of adding surfactants on the average shell-side heat transfer coefficient. The addition of 1-octanol leads to an increase in heat transfer coefficient by 150-300 $\text{W m}^{-2} \text{K}^{-1}$ in the film Reynolds number range considered. The enhancement caused by 1-octanol increases at higher film Reynolds number. The reduction of surface tension improves wettability and increases the heat transfer area. This increased utilization of heat transfer area leads to much thinner films, thereby, leading to higher heat transfer coefficients. The absorber UA is dependent on thermal resistances of the coupling fluid, wall conduction and the working fluid. The coupling fluid resistance accounts for 22.8% of the total resistance and remains unchanged with the addition of surfactants. The working fluid thermal resistance decreases by 37% in the presence of surfactants (Figure 5.9).

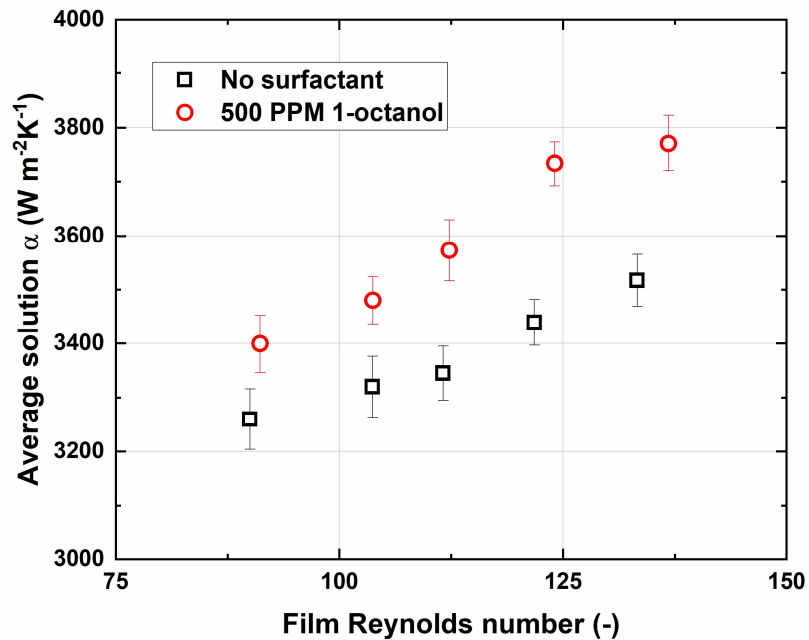


Figure 5.8: Variation of solution heat transfer coefficient

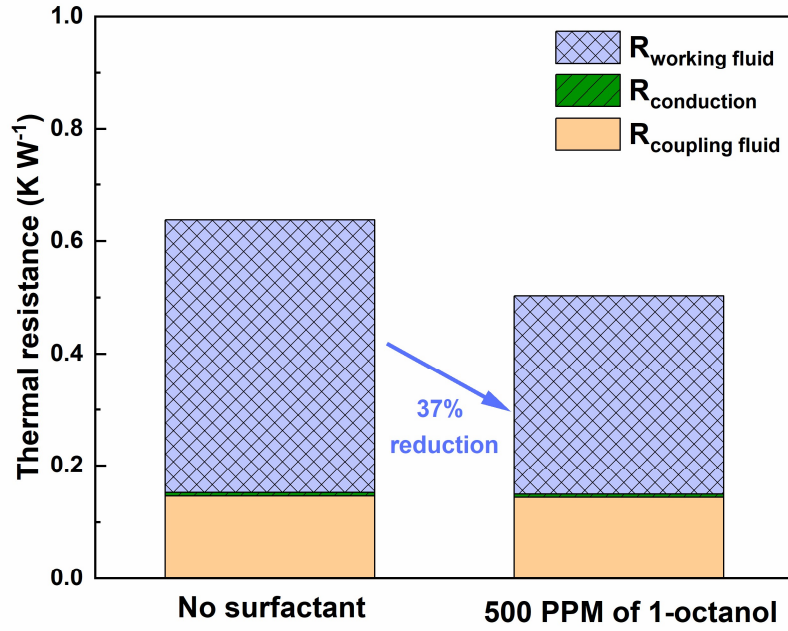


Figure 5.9: Thermal resistance of a single tube in the absorber

Figure 5.10 shows the closest approach temperature (CAT) at the exit of the absorber during steady-state operation and is defined by Eq. (5.15)

$$CAT_{abs} = T_{abs,conc,out} - T_{abs,cf,in} \quad (5.15)$$

A lower CAT indicates better heat and mass transfer in the absorber. The measurement uncertainties of the thermocouples are also shown in the plot. The CAT in the absence of surfactants is ~ 2 K while it decreases to ~ 0.25 K with the addition of 1-octanol, demonstrating the effectiveness of adding surfactants. While single-phase heat transfer post absorption in the subcooling section is not impacted by the presence of surfactants,

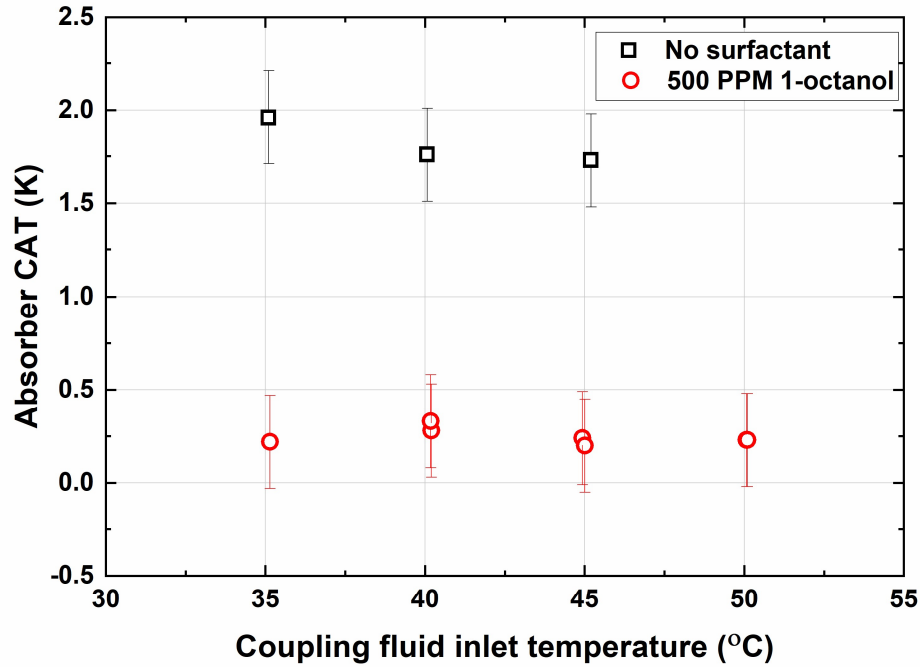


Figure 5.10: Absorber closest approach temperature (*CAT*)

the enhancements in mass transfer and wettability result in improved absorption. This leads to completion of absorption in smaller overall area within the absorber, resulting in more area for the subcooling of the ammonia-water mixture in the presence of 1-octanol.

Figure 5.11 shows the variation of absorber UA with coupling fluid temperatures for a concentrated solution flow rate of $24 \times 10^{-3} \text{ kg s}^{-1}$ with a vapor mass fraction of 0.25. The addition of 1-octanol leads to an increase in absorber UA by 10%, which is significantly lower than the 23% enhancement observed at the higher $32 \times 10^{-3} \text{ kg s}^{-1}$ solution flow rate. The absorber under consideration is designed for a larger flow rate and capacity and is thus significantly oversized when operating at these lower flow rates. The absorber CAT at this reduced flow rate is $\sim 0.2 \text{ K}$ both in the presence and absence of 1-

octanol. The oversized absorber thus results in complete absorption and sub-cooling of the ammonia-water mixture even in the absence of surfactants. The addition of surfactants and the subsequent enhancements are not remarkable when the absorber is oversized for the specified operating conditions. This can be captured by the wetting area ratio (ϕ) shown in Figure 5.12. At low solution flow rate of $24 \times 10^{-3} \text{ kg s}^{-1}$, the wetting area ratio increases from 26.8% to 29.1% by adding surfactants. The wetting area ratio, however, changes from 29.8% to 35.1% when surfactants are added at higher solution flow rate of $32 \times 10^{-3} \text{ kg s}^{-1}$. These modified wetting area ratios can be used for the prediction of surfactant enhanced absorber performance using the modeling framework developed in Chandrasekaran et al. (2020).

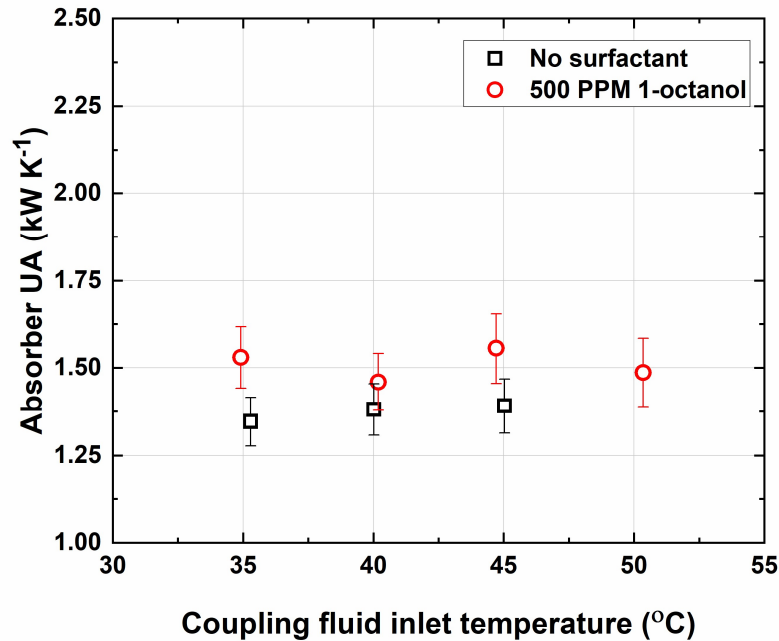


Figure 5.11: Absorber UA at lower solution flow rate $\dot{m}_{conc} = 24 \times 10^{-3} \text{ kg s}^{-1}$

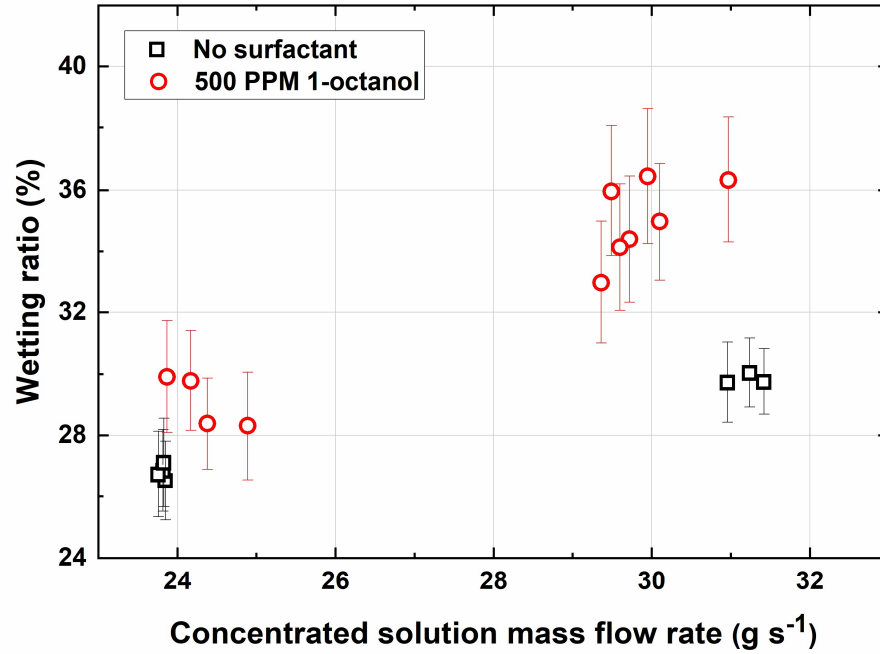


Figure 5.12: Variation of wetting area ratio

5.4.2 System level effects

The absorber pressure during steady-state operation in the two-pressure facility is shown in Figure 5.13. In the presence of surfactants, it is observed that the absorber pressure is reduced by ~50 kPa when compared to operating the system without surfactants when all other conditions are kept constant. It must be noted that the high-side pressure did not change with the addition of surfactants. This lowering of low-side pressure results in a reduction in the saturation temperature of the working fluid and a lower approach temperature that enhances absorber performance. Typical absorbers that employ microscale geometries are rated to pressures of ~900 kPa (Forinash, 2015; Garimella et al., 2020). This practically limits the operation of microchannel absorption heat pumps to

ambient temperatures $\sim 45^{\circ}\text{C}$. However, much higher ambient temperatures are experienced in many parts of the world. The addition of surfactants and the eventual reduction in absorber pressure can allow for operation at temperatures $>50^{\circ}\text{C}$. Due to this reason, the absorber was operated in the presence of 1-octanol at coupling fluid temperatures even above 50°C as seen in Figures 5.6-5.9. The absorber pressure dictates the low-side pressure in the system and therefore, affects the evaporator pressure. Potential benefits of this include delivering cooling at a lower evaporator temperature, increasing cooling duty, or lowering of source temperature to drive the vapor absorption cycle.

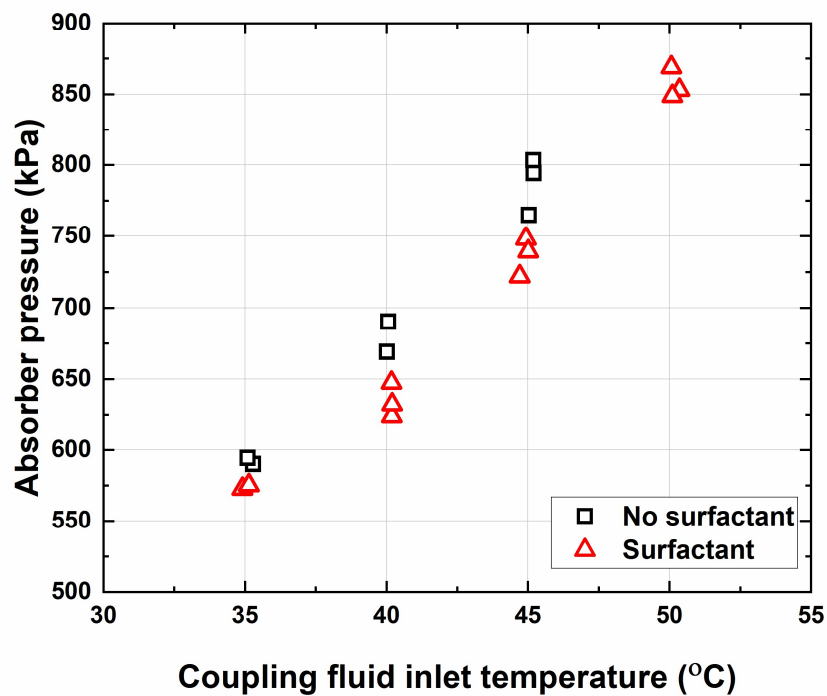


Figure 5.13: Steady state absorber pressure

The desorber uses heat input to separate ammonia vapor from the ammonia-water solution by boiling. While there are no studies in the literature that consider ammonia-water mixture boiling in the presence of surfactants, many researchers have studied surfactant-enhanced pool boiling in water (Wasekar and Manglik, 1999; Cheng et al., 2007; Kumar et al., 2018), water-LiBr mixture (Wu et al., 1998), water-ethanol mixture (Inoue et al., 2004). Surfactants affect bubble dynamics including the bubble diameters and departure frequencies and thus, influence the nucleate boiling process. Passive enhancement in the pool boiling of water with surfactants has been demonstrated. However, the surfactants that have produced the highest enhancement are sodium dodecyl sulfate and Triton X-100. Wu et al. (1998) performed pool boiling experiments with 1-octanol using water-LiBr and concluded that 1-octanol produced no effect on boiling heat transfer. In this study, the effect of 1-octanol on overall desorber performance is evaluated. Figure 5.14 shows the desorber UA as a function of the ammonia vapor generation rate. The desorber UA is not affected by the addition of 1-octanol. The normalized energy input (\tilde{E}_{des}) is not altered in the presence of 1-octanol (Figure 5.15). Thus, the amount of energy required to generate unit mass of ammonia remains unchanged by the addition of 1-octanol. This is attributed to several competing effects at play during the boiling of ammonia-water in the presence of surfactants, including the enhancement in the pool boiling phenomenon due to changes in nucleation density and bubble dynamics, and the suppression of mass transfer due to the barrier effect (Kim et al., 2006). The use of a diabatic distillation column based desorber design with both pool boiling and partial purification within each tray further adds to the complexity. While these experiments may not provide detailed insights into the effect of 1-octanol on the pool boiling process of ammonia-water mixture, it is

evident that the desorber characteristics do not change from the perspective of heat and mass transfer area and the energy required for vapor generation. The combined effect of unchanged desorber performance and suppressed low-side pressure due to the addition of surfactants will lead to an increase in evaporator heat duty at given ambient conditions or allow for operation at more adverse conditions. This will lead to an overall enhancement in the *COP* of the system.

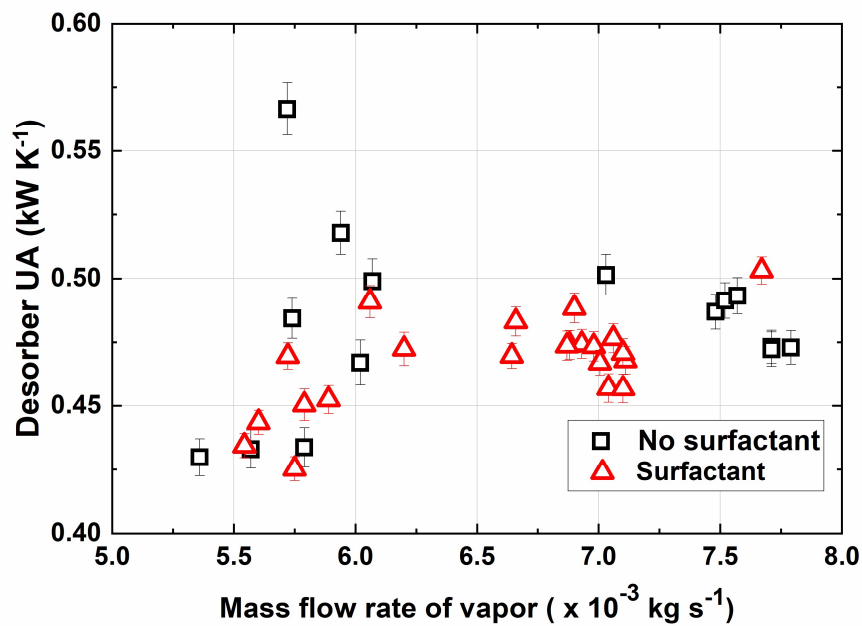


Figure 5.14: Effect of 1-octanol on desorber *UA*

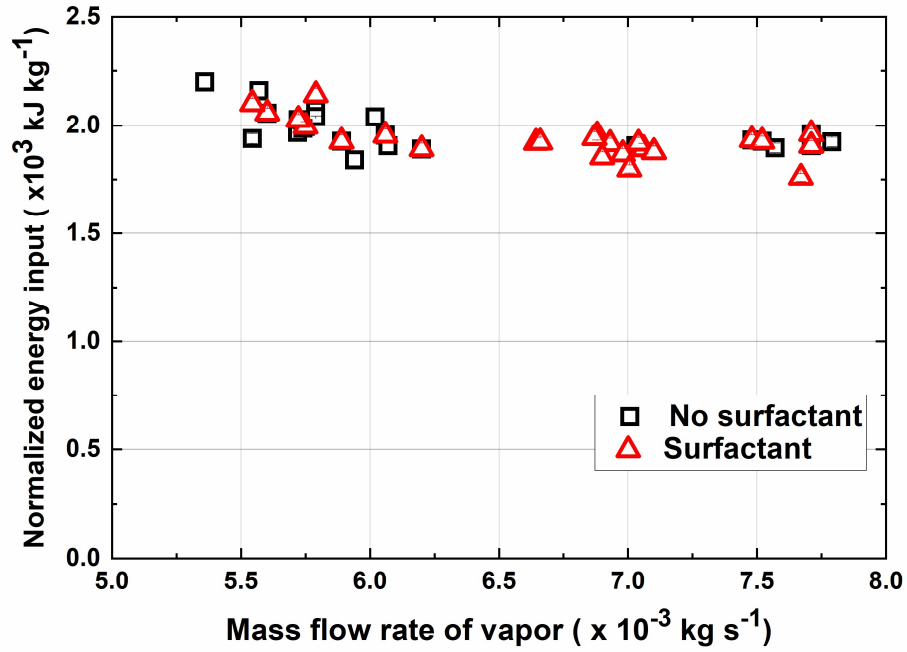


Figure 5.15: Effect of 1-octanol on desorber normalized energy input

5.5 Conclusions

The effect of surfactants on the performance of a compact, shell-and-tube absorber with microscale geometrical features for an ammonia-water mixture is investigated in an experimental facility that closely simulates the operating conditions in an absorption chiller. Absorber heat duties are measured for different solution flow rates and coupling fluid inlet temperatures. Passive enhancement of absorber performance due to the addition of 1-octanol is demonstrated at all conditions. Absorber UA is improved by 10-23% with the highest improvement observed at the largest solution flow rates. The UA enhancement is specifically due to a reduction in working fluid thermal resistance by up to 37%, while the coupling fluid resistance remains unchanged. 500 PPM of 1-octanol is determined to

be the optimal concentration of the additive with no further enhancement observed with additional quantities of the surfactant. This study demonstrates that the reduction in surface tension due to the addition of 1-octanol results in improved mass transfer due to interfacial turbulence and improved wettability. The effect of surfactants on system behavior and other components is also evaluated to understand the overall impact of surfactants on system performance. The suppression of low-side pressure due to surfactants can result in higher evaporator cooling duty and has other benefits, including the ability of the system to operate at higher ambient temperatures and lowering the heat source temperature. The heat and mass transfer processes in the desorber are not affected by the presence of 1-octanol. The combined effect of unchanged desorber performance and reduced low-side pressure leads to an improvement in the *COP* of the system.

CHAPTER 6. COMPARISON OF BUBBLE AND FALLING-FILM MODES OF ABSORPTION

6.1 Introduction

Two absorption modes are investigated in the present study: bubble absorption in vertical tubes and falling-film absorption along vertical tubes. A 50-200 W ammonia-water bubble absorber was experimentally investigated in a single-pressure facility over a wide range of operating conditions in Chapter 4. A coupled heat and mass transfer model was developed to analyze the bubble absorption process, including the effects of surfactants. A complementary study on surfactant-enhanced falling-film absorption in a two-pressure facility that replicated a single-effect ammonia-water absorption chiller was presented in Chapter 5. Absorption duties in the range of 8-16 kW were achieved and the effect of surfactants on the wetting ratio was experimentally determined.

The analyses on the two absorption modes were conducted over significantly different component sizes and duties. It was also observed that the effects of surfactants on absorber performance were different for the two modes because the mechanisms for enhancement are different based on the geometry and mode of absorption. For a valid comparison between the two modes of absorption, their performance must be assessed at similar operating conditions. Under such conditions, a comparison can be made between the two surfactant-enhanced absorption modes in terms of heat and mass transfer rates, temperature and concentration profiles, overall component size and weight, and fabrication aspects.

6.2 Operating conditions

The operating conditions under consideration here are determined from a system-level thermodynamic model developed for an absorption heat pump with a cooling capacity of 10.5 kW. The Air-Conditioning, Heating, and Refrigeration Institute (AHRI) conditions are used for the evaporator and heat rejection temperatures (AHRI, 2008). The evaporator coupling fluid enters at a temperature of 12.78°C and exits at a temperature of 7.21°C. The condenser and absorber are hydronically cooled with distilled water at 35°C. The corresponding absorber duty is calculated to be 16.2 kW. Table 6.1 shows a summary of the operating conditions for the absorber. The pressure drop within the absorber is an important consideration for the component and overall cycle performance. A high pressure drop results in a decrease in the solution saturation temperature, which reduces the driving temperature differences between the solution and coupling fluid. The lower driving temperature differences require increased area to transfer the same absorption duty, resulting in a larger component. Thus, a nominal pressure drop of 20 kPa is budgeted in the cycle model.

6.3 Absorber geometry

Shell-and-tube heat exchangers are the most widely used heat exchangers in the process industry because of their relatively simple manufacturing and their adaptability to different operating conditions (Patel and Rao, 2010). In this comparative assessment, a shell-and-tube heat and mass exchanger framework is adapted for both the falling-film and bubble modes of absorption. The shell size is limited to 0.15 m due to the restrictions of the ASME boiler and pressure vessel code (ASME, 2021).

Table 6.1: Operating conditions of the absorber

Variable	Value
Inlet solution flow rate, $\dot{m}_{sol,in}$	0.027 kg s^{-1}
Inlet refrigerant flow rate, $\dot{m}_{ref,in}$	0.0092 kg s^{-1}
Inlet solution temperature, $T_{sol,in}$	75.2°C
Inlet refrigerant temperature, $T_{ref,in}$	54.8°C
Inlet solution concentration, $x_{sol,in}$	0.384
Inlet refrigerant concentration, $x_{ref,in}$	0.997
Inlet absorber pressure, $P_{abs,in}$	520 kPa
Inlet coupling fluid temperature, $T_{CF,in}$	35°C
Coupling fluid flow rate, \dot{m}_{CF}	0.31 kg s^{-1}

6.3.1 *Falling-film absorber*

A vertically-oriented, baffled, shell-and-tube absorber (Figure 1.1) with working fluid (ammonia-water mixture) on the shell-side and coupling fluid (water) on the tube-side is considered in this study. The shell-side is chosen for the working fluid to mitigate the potential maldistribution issues associated with the two-phase flow through the tube-side of the heat exchanger. A lip is provided in each of the baffles to accumulate solution and form solution pools. The solution flows through both the baffle cut in the window region, as well as through the gaps between the tube and the baffle. The dilute solution and the vapor entering the absorber are pre-mixed upstream of the absorber in a mixing section. This pre-mixed solution/vapor mixture then enters from the top of the absorber and flows

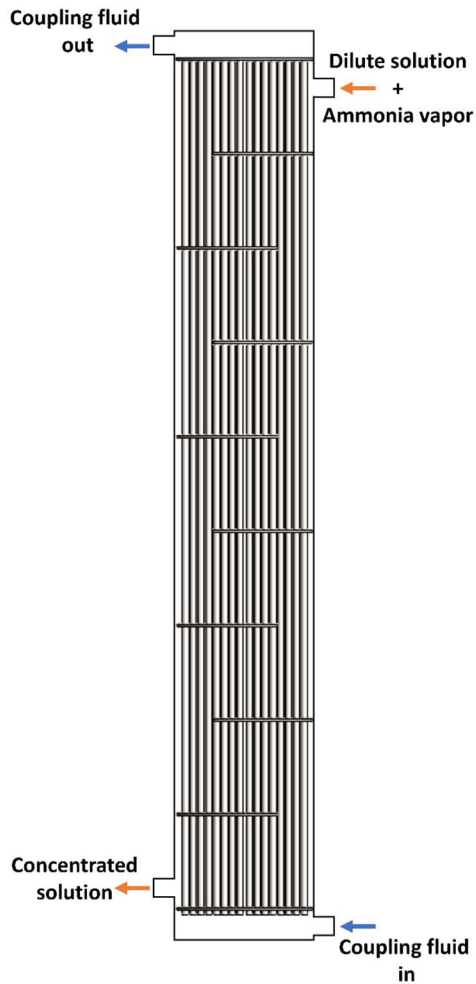


Figure 6.1: Schematic of falling-film absorber

downwards. The coupling fluid on the tube side flows from the bottom to the top of the absorber.

Two falling-film absorber designs are considered in this study with different tube diameters. The number of tubes that can be accommodated is dependent on the tube diameter. Using small diameter tubes enables a very high density of tubes. The high tube density increases the surface area available for heat and mass transfer. In addition, the

serpentine flow path forced by the tight baffle spacing in combination with the tight tube spacing enables increased mixing between the solution and vapor, thereby increasing the interfacial area and absorber performance. However, there are some disadvantages of high-density tube bundles, such as the large material costs and weight of the component, and fabrication challenges associated with a large number of tube welds or braze joints. It was also observed from the study of Chandrasekaran et al. (2020) that a significant fraction of the small diameter tubes were not in contact with the working fluid, resulting in lower wetting ratios. In the second design, 6.35-mm OD tubes are used in the same overall component envelope. The key dimensions of the two falling-film absorber designs are shown in Table 6.2.

Table 6.2: Geometry of falling-film absorbers

Parameter	Falling-film 1	Falling-film 2
Shell D_o (m)	0.15	
Shell D_i (m)	0.147	
Tube D_o (mm)	3.175	6.35
Tube D_i (mm)	2.15	4.57
Tube Pitch-to-Diameter Ratio (-)	1.325	0.85
Tube Count (-)	955	294
Baffle Count (-)	21	
Nominal Baffle Spacing (mm)	38	
Baffle Cut (%)	24	
Total Length (m)	1	

6.3.2 Bubble absorber

A schematic of the vertical tubular bubble absorber packaged in a shell-and-tube framework is shown in Figure 1.2. The ammonia vapor and dilute solution are distributed at the bottom of the absorber and flow upwards in co-current orientation inside the tubes. The vapor enters at the bottom as shown in Figure 1.3 and is distributed into the tubes through small diameter tubes (nozzles). The dilute solution enters the tubes through the free area between the tubes and nozzles. Each tube assembly is analogous to the bubble absorber design investigated in Chapter 4.

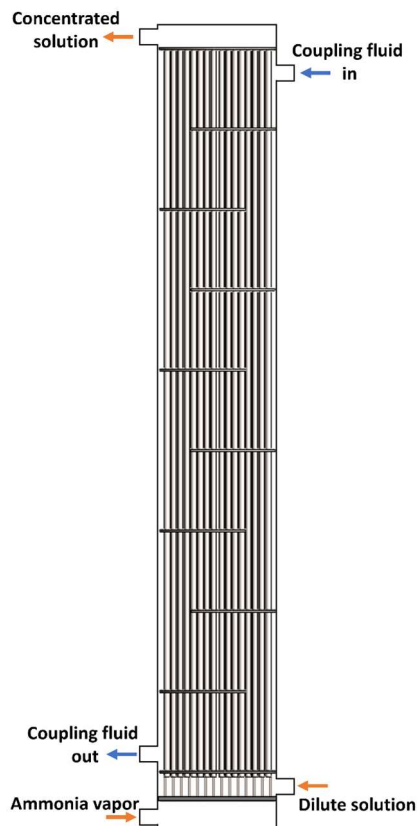


Figure 6.2: Schematic of bubble absorber

The absorption process progresses as the vapor and liquid make contact inside the tubes. The concentrated solution exits at the top of the absorber. Water serves as the coupling fluid. A set of baffles is arranged transverse to the tube bundle to drive the coolant and for structural rigidity. The water flows downwards and locally transverse to the tube bundle, in a globally counter-current direction to the liquid–vapor mixture. The key dimensions of the bubble absorber are tabulated in Table 6.3.

Table 6.3: Geometry of bubble absorber

Parameter	Value
Shell D_o (m)	0.15
Shell D_i (m)	0.147
Tube D_o (mm)	9.525
Tube D_i (mm)	7.74
Tube Count (-)	148
Baffle Count (-)	21
Baffle Cut (%)	24
Total Length (m)	1

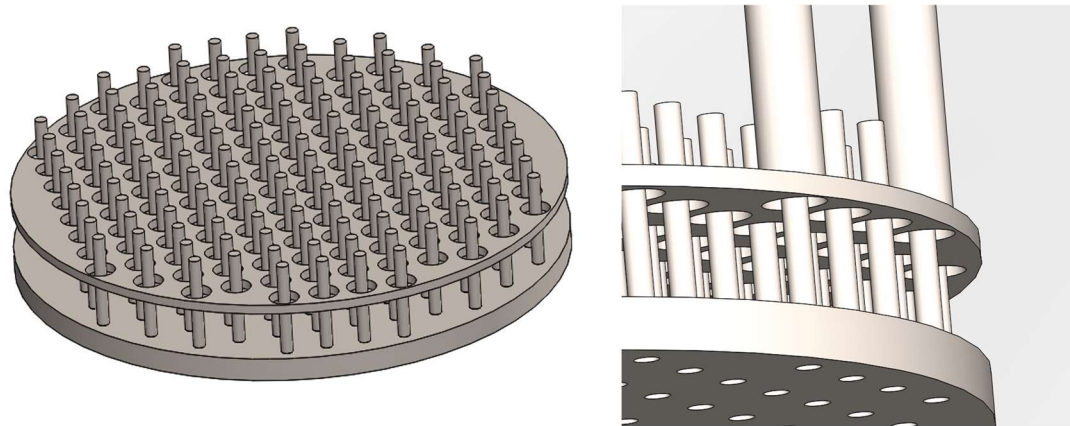


Figure 6.3: Liquid-vapor distribution at the bottom of bubble absorber

6.4 Modeling framework

A segmental heat and mass transfer model is developed for the falling-film and bubble absorber designs proposed in Section 1.3 to investigate the local variations in solution and vapor mass flow rates, concentrations, temperatures, etc., and predict the overall absorber heat duties. The model uses the approach by Price and Bell (1974), which, in turn, is based on the framework developed by Colburn and Drew (1937). The general heat and mass transfer equations using the Colburn-Drew method and the conservation equations for mass, species and energy that were discussed in Chapter 4 (Eq. 4.10 – 4.26) are used in the segmental model. The specific equations for heat and mass transfer coefficients and the individual resistances for each mode of absorption are discussed in the subsequent sections. It must be noted that the liquid film in the falling-film absorber is assumed to be well-mixed; therefore, the mass transfer resistance of the liquid film is neglected. This is consistent with falling-film absorption models developed in the literature (Price and Bell, 1974; Kang and Christensen, 1994; Garimella, 2000). However, no such assumptions can be made in the bubble mode of absorption and thus, both heat and mass transfer resistances for liquid and vapor are considered. For the segmental model, the area between two consecutive baffles is considered as one segment for both falling-film and bubble absorbers.

6.4.1 *Falling-film absorber model*

In the falling-film absorber, the shell-side flow regime is idealized as a solution film that covers a fraction of the tube circumference, while vapor contacts both the solution as well as the exposed, dry region of the tube. It must also be noted that the present model

assumes that this idealized liquid-vapor distribution is identical for all the tubes in a segment. The wetting ratio (ϕ), developed from the experimental data of Chandrasekaran et al. (2020) is used in quantifying the fraction of the tube surface that is in contact with the liquid. This is used to calculate the heat and mass transfer areas, as well as the film thickness.

$$\phi = 11.325 \dot{m}_{sol,avg} \quad (6.1)$$

The contribution to interfacial area from the liquid pools on the baffle lips is neglected, and the interfacial area is taken to be the outer surface area of the solution films partially covering the tubes in each segment as shown in Eq. (6.2)

$$A_{int} = \pi (d_0 + 2\delta_{film}) \phi L_{seg} N_{tube} \quad (6.2)$$

The film thickness, δ , is calculated from the Nusselt laminar film condensation theory, using the average mass flow rate, the wetted ratio and the thermophysical properties of the solution and vapor in the corresponding segment, as shown in Eq. (6.3).

$$\delta_{film} = \left(\frac{3\mu_{sol} \dot{m}_{sol,avg}}{g\rho_{sol} (\rho_{sol} - \rho_{vap}) \pi d_0 \phi N_{tube}} \right)^{1/3} \quad (6.3)$$

The vapor Nusselt number is calculated using the Bell-Delaware method for shell-and-tube heat exchangers (Bell et al., 1988). The ideal single-phase heat transfer coefficient calculated from a cross flow correlation is corrected to account for the effects of the flow configuration, and bypass and leakage streams associated with the shell-and tube-geometry. The general expression for Nu_{vap} is shown in Eq (6.4). The Nu_{ideal} is

calculated using the correlation for crossflow over staggered tube banks (Zukauskas, 1972; Hewitt and Barbosa, 2008). These correlations are shown in Table 6.4 for different Reynolds number ranges. The values for J_c and J_b are calculated using the correlations for the Bell-Delaware method (Hewitt et al., 1994).

$$Nu_{vap} = Nu_{ideal} J_c J_b \quad (6.4)$$

Next, the vapor mass transfer coefficient is determined using the vapor Sherwood number. The value of vapor Sherwood number is calculated using the heat and mass transfer analogy. The coupling fluid flow is always laminar, and a Nusselt number of 4.364 is used to calculate the heat transfer coefficient. The solution heat transfer resistance is calculated using Eqs. (6.5) and (6.6). Additional details of the falling-film absorber model are discussed in Chandrasekaran et al. (2020).

$$R_{sol,seg} = \frac{1}{\alpha_{film} A_{film}} \quad (6.5)$$

$$\alpha_{film} = \frac{k_{film}}{\delta_{film}} \quad (6.6)$$

Table 6.4: Heat transfer correlations for cross-flow through tube banks

Reynolds number Range	Nusselt number Correlation
$1 \times 10^0 - 5 \times 10^2$	$1.04 \cdot Re^{0.4} \cdot Pr^{0.36} \cdot (Pr/Pr_w)^{0.25}$
$5 \times 10^2 - 1 \times 10^3$	$0.71 \cdot Re^{0.5} \cdot Pr^{0.36} \cdot (Pr/Pr_w)^{0.25}$
$1 \times 10^3 - 2 \times 10^5$	$0.35 \cdot (S_L/S_T)^{0.2} \cdot Re^{0.6} \cdot Pr^{0.36} \cdot (Pr/Pr_w)^{0.25}$
$2 \times 10^5 - 2 \times 10^6$	$0.031 \cdot (S_L/S_T)^{0.2} \cdot Re^{0.8} \cdot Pr^{0.4} \cdot (Pr/Pr_w)^{0.25}$

The performance of the falling-film absorber is enhanced by the addition of surfactants as observed in Chapter 5. The specific mechanisms leading to this improved performance include the enhancement in mass transfer coefficient due to Marangoni convection and improvement in wetting ratio that leads to larger surface area and thinner films. The model accounts for the improved mass transfer coefficient by using the mass transfer enhancement factor R , introduced in Chapter 2. This enhancement factor is a function of the Marangoni number. The wetting ratio is similarly modified based on the data from Chapter 5.

$$\phi = 12.85 \dot{m}_{sol,avg} \quad (6.7)$$

6.4.2 Bubble absorber model

In the bubble absorber, the heat and mass transfer areas are different, unlike in the falling-film mode. The heat transfer primarily occurs at the inner surface of the tube between the solution and coupling fluid. The model assumes there is no direct heat transfer between the vapor and the coupling fluid. The vapor-liquid interfacial area participates in

the mass transfer process and is calculated using the Ozar et al. (2012) correlation, which was shown to best predict the interfacial area data in Chapter 3. The interfacial area per unit volume, also known as interfacial area concentration (IAC) is given by

$$IAC = \frac{4.5C_t}{D_H} \frac{\alpha - \alpha_{gs}}{1 - \alpha_{gs}} + \frac{6\alpha_{gs}}{D_{sm}} \frac{1 - \alpha}{1 - \alpha_{gs}} \quad (6.8)$$

An empirical correlation is used to predict the Sauter mean diameter (D_{sm}).

$$\frac{D_{sm}}{Lo} = 1.99 \left(\frac{Lo}{D_H} \right)^{-0.335} \left(\frac{\varepsilon^{1/3} Lo^{4/3}}{\nu_L} \right)^{-0.239} \quad (6.9)$$

where ε is energy dissipation rate per unit mass. It is the sum of energy dissipation due to bubble expansion and due to wall friction, and is calculated using the method presented by Hibiki and Ishii (2002).

The solution heat transfer resistance is calculated using the correlation of Shah for upward condensing flow. The results from Chapter 4 showed that this correlation performed well when compared with experimental data. The liquid-side mass transfer coefficient is calculated using the correlation developed by Akita and Yoshida (1974) shown in Eq. (4.13)

$$\beta_{sol} = \frac{0.5D_{aw,sol}}{d_B} \left(\frac{\mu_{sol}}{\rho_{sol}D_{aw,sol}} \right)^{0.5} \left(\frac{gd_B^3 \rho_{sol}^2}{\mu_{sol}^2} \right)^{0.25} \left(\frac{gd_B^2 \rho_{sol}}{\sigma} \right)^{\frac{3}{8}} \quad (6.10)$$

The vapor side mass transfer coefficient is determined using the vapor Sherwood number (Sh), which is calculated using the heat and mass transfer analogy.

6.5 Results

The results from the comparative assessment of falling-film and bubble absorbers are discussed in this section. The impact of surfactants on each design is first considered. Figure 6.4 shows the heat duty of the absorber for the falling-film absorber design 1 with small-diameter tubes and high-density tube packing. Complete absorption is achieved with this design regardless of the addition of surfactants. A 12.5% reduction in required absorber area and thus, length is achieved by adding surfactants. This is consistent with the results observed in Chapter 5 for the given solution flow rate.

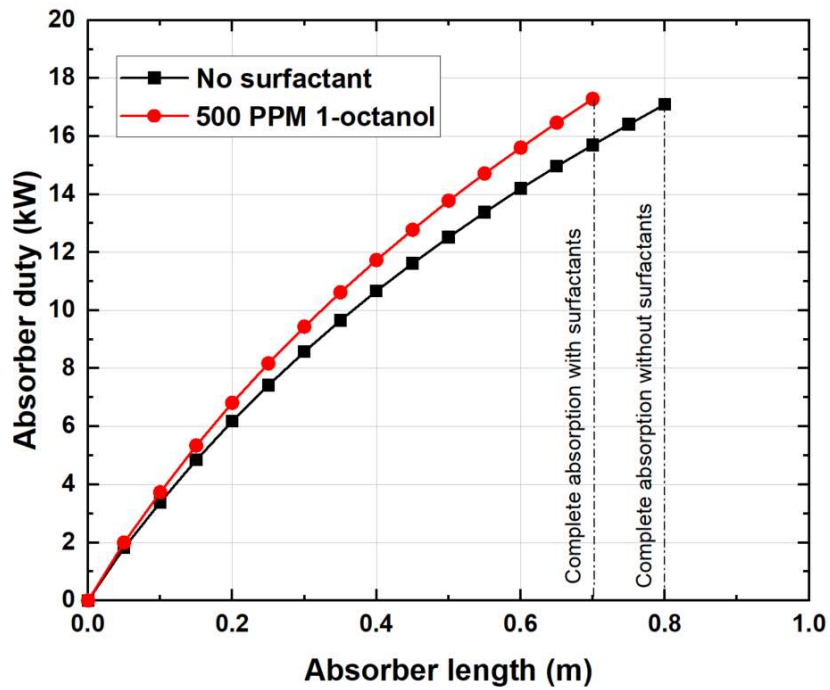


Figure 6.4: Absorber heat duty for falling-film design 1

The performance of the falling-film absorber with larger diameter tubes is discussed next. The number of tubes that can be accommodated within the same shell is only 294 as compared to 955 with the smaller tubes. This leads to a significant decrease in the overall shell-side surface area available for heat and mass transfer. Without surfactants, this design does not result in complete absorption within 1 m of length. A total of 1.2 m is required for completely absorbing all the ammonia vapor. The addition of surfactants results in a reduction of 18% in required area, thus accommodating it within 1 m of absorber length.

Figure 6.6 compares the effect of surfactants on the heat duty of the bubble absorber. Much higher duties are observed at the inlet of the bubble absorber as compared to falling-film designs due to the favorable concentration differences between the solution and the refrigerant and the high degree of mixing achieved by churn flow, which result in

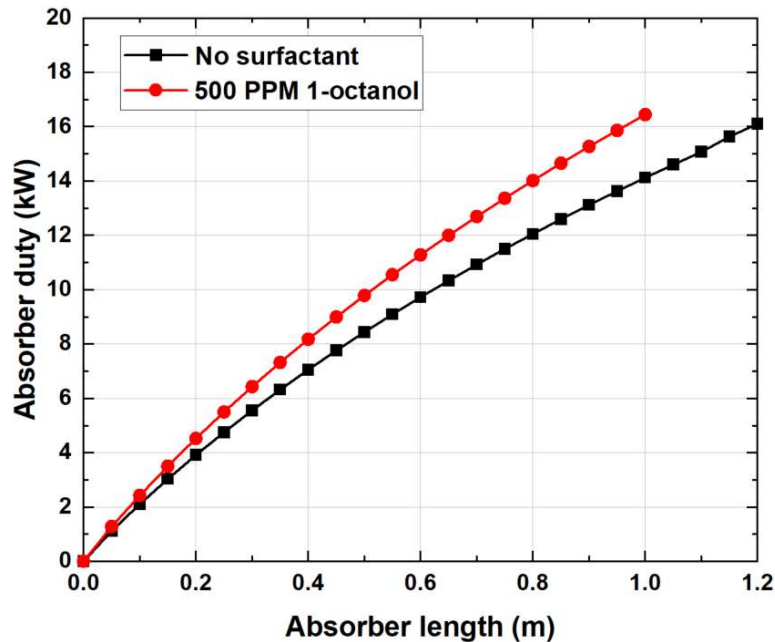


Figure 6.5: Absorber heat duty for falling-film design 2

higher driving temperature differences and thus, higher duties. A total absorber length of 1.3 m is required for complete absorption without surfactants. However, in the presence of surfactants significant enhancement is observed, especially in the middle sections where slug flow prevails. The surfactants aid in breaking up large slugs into smaller bubbles, resulting in higher interfacial area and mass transfer. Overall, the addition of 1-octanol leads to a 23% reduction in absorber size with the ammonia vapor being completely absorbed within 1 m. The pressure drop model accounts for hydrostatic pressure drop, fluid acceleration, and frictional pressure changes. A maximum pressure drop of 6.4 kPa is seen with the contribution from the hydrostatic head accounting for 72% of the total.

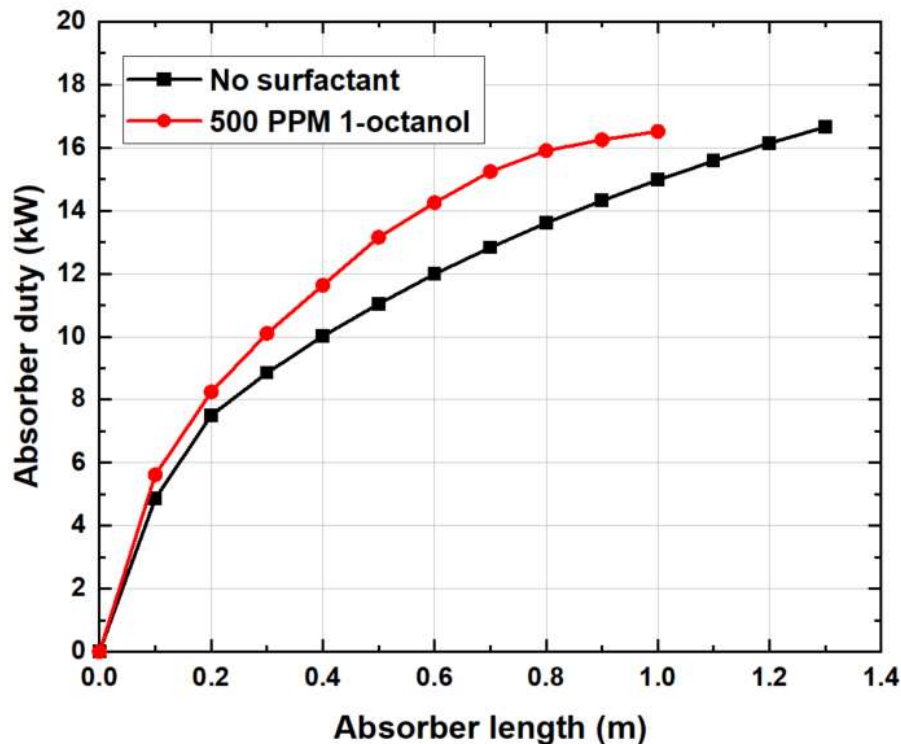


Figure 6.6: Absorber duty for bubble mode

From the above discussion, it is evident that surfactants enhance absorber performance in both falling-film and bubble modes. The shell-and-tube design can be used for a ~ 16 kW heat duty absorber, with the length of the absorber not exceeding 1 m in both modes. Figure 6.7 compares the heat duties of the three absorber designs investigated in this study with the addition of 1-octanol. As noted before, the bubble absorber has very high heat transfer rates at the inlet. However, the absorption rate in the bubble absorber decreases dramatically towards the latter part of the absorber, indicating that the heat and mass transfer resistance to absorption is higher than the corresponding resistance to absorption in the falling-film absorber. A similar trend was reported by Nagavarapu (2012).

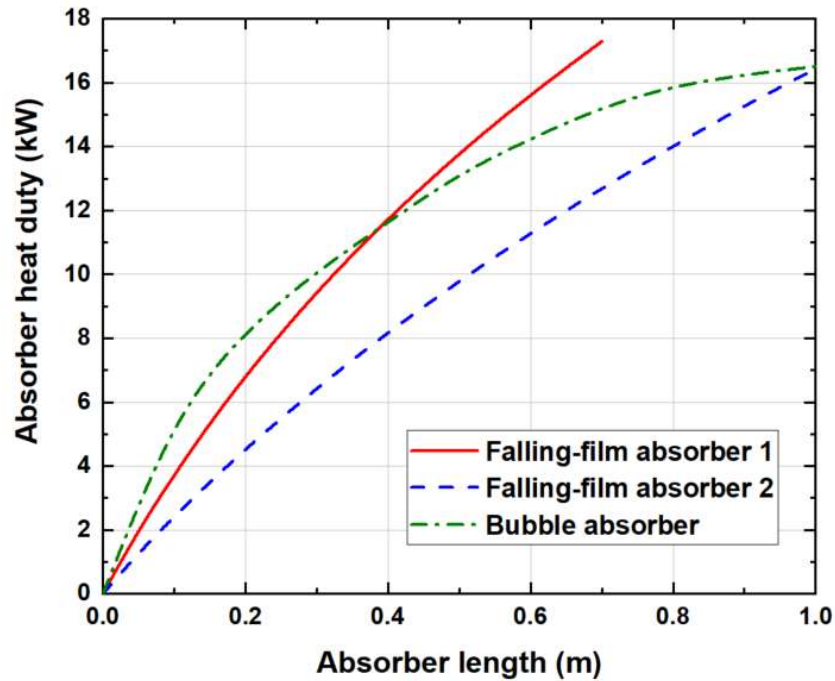


Figure 6.7: Comparison of absorber duties in the presence of surfactants

Although the overall footprint of the heat exchanger remains similar for all three designs considered, the total material costs and weight of the components differ substantially. The mass of the tube bundle and the overall surface area available in each design is shown in Figure 6.8. For the falling-film design 1, only the required length of 0.7 m is used in this calculation. For the bubble absorber configuration, a 30.6% reduction in mass of the tube bundle is seen. The mass of the shell and the end caps are not included in these values as they are not expected to change between the different geometries. A typical shell with a thickness of 2.2 mm would have a mass of 7.8 kg. Furthermore, the use of a lower number of larger diameter tubes in the bubble absorber contributes to the ease of manufacturability due to a reduction in the number of welding/braze joints.

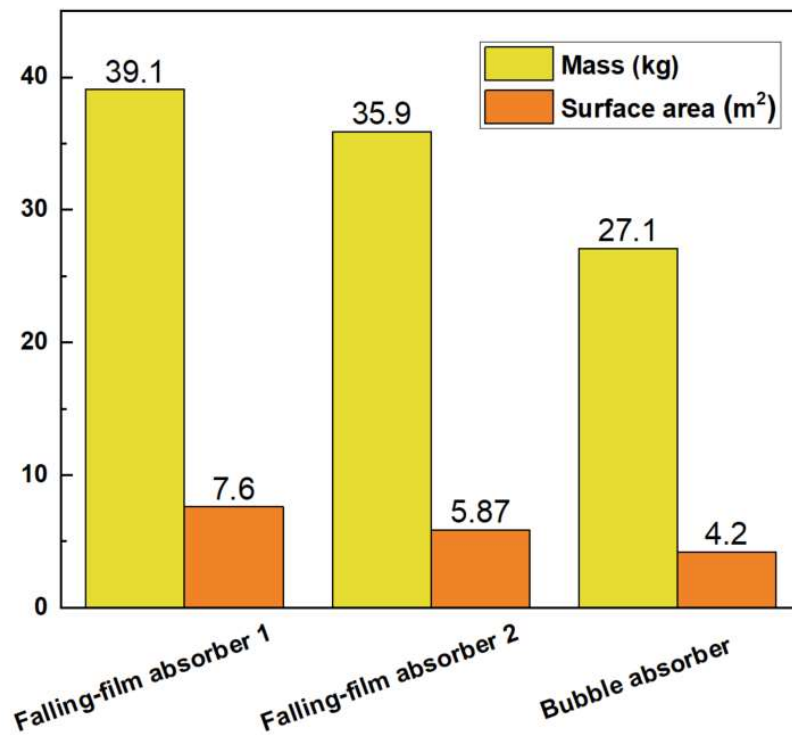


Figure 6.8: Comparison of absorber mass and surface area

6.6 Conclusions

A comparative assessment of the two absorption modes, falling-film absorption and bubble absorption, was conducted in this chapter. The heat and mass transfer models developed in the previous chapters were applied to design an absorber for a 10.5 kW cooling capacity chiller for residential applications. Optimal designs were identified for each mode based on design and operational constraints. Surfactants improved the absorber performance in both falling-film and bubble modes. The falling-film absorber with small diameter tubes required the shortest length for completing absorption. However, the large number of tubes in this design increased the component mass appreciably. The bubble absorber was found to be favorable overall due to its performance, low cost, and simpler manufacturing process.

CHAPTER 7. CONCLUSIONS AND RECOMMENDATIONS

A detailed investigation of ammonia-water absorption in the presence of surfactants was conducted. The underlying mechanisms that result in enhancements in heat and mass transfer are identified and a screening of surfactants was conducted. The existence of a critical Marangoni number required to initial interfacial turbulence was discussed. This explained the anomalous behavior reported by several researchers in which reduction in surface tension did not result in improved performance in the absorber. A surfactant selection criterion was developed based on the plateau value of surface tension, critical concentration, and the critical Marangoni number. The pendant-drop technique, a method suitable for surfactant-based solutions, was used to determine the surface tension of ammonia-water solution in the presence of various surfactants. It was determined that 500 PPM of 1-octanol and 2-ethyl-1-hexanol are the preferred additives. A preliminary heat and mass transfer model was developed for a falling-film absorber to understand the impact of the chosen surfactant on the performance of an absorber. The results showed that the overall conductance of the absorber increased by ~30% due to passive enhancement caused by 500 PPM of 1-octanol.

The impact of 1-octanol on the performance of a bubble absorber was investigated. First, a hydrodynamic study was conducted with air-water mixtures to quantify the impact of surfactants on interfacial area, bubble size distribution and bubble velocities. High-speed videos along with novel computer vision-based methods were used to analyze and quantify the change in flow behavior. The addition of 1-octanol resulted in enhancement in interfacial area due to the prevention of bubble coalescence, leading to many small

diameter bubbles. The measured values of interfacial area were compared with several correlations proposed in the literature. Surfactants also led to a decrease in bubble velocity and increase in the residence time due to the shear stresses caused by the non-uniform concentration distribution of surfactant along the bubble surface.

Heat and mass transfer in a bubble absorber was investigated next. A single-pressure test facility was developed, and the absorber was tested over a range of solution flow rates, vapor flow rates, and coupling fluid temperatures. It was observed that the performance of the absorber was limited by the liquid-side mass transfer resistance in the absence of additives. The addition of 1-octanol led to enhancements in the liquid-side mass transfer coefficient due to interfacial turbulence. The combined effect of increased mass transfer coefficient and interfacial area due to surfactants improved mass transfer and hence, the overall performance of the bubble absorber. It was also observed that adding surfactants beyond 1000 PPM led to a significant reduction in absorber performance because of the barrier effect. A physics-based heat and mass transfer model was developed for a bubble absorber. The model was validated with experimental data, and showed that it was able to predict the absorber overall heat duty with an AAD of 8.3%.

The performance of a vertical falling-film absorber was also investigated in the presence of surfactants. A two-pressure facility that closely simulated the operating conditions of a 10.5 kW cooling capacity absorption heat pump was used for testing the absorber performance. Absorber UA was improved by 10-23%, with the highest improvement observed at the largest solution flow rates. Contrary to bubble absorbers, adding 1-octanol above 500 PPM was not detrimental to the performance of the falling-film absorber. In addition to enhancements in mass transfer coefficient, surfactants

promoted wetting, leading to more effective use of the available surface area within the heat exchanger. The effects of surfactants on system behavior and other components and the overall system were also evaluated. A suppression of low-side pressure due to surfactants was observed. This could result in higher evaporator cooling duty and other benefits, including the ability of the system to operate at higher ambient temperatures and lower heat source temperatures. The heat and mass transfer processes in the desorber were not affected by the presence of 1-octanol.

Finally, a comparative assessment between the two absorption modes was conducted. The test sections developed for falling-film absorption and bubble absorption were evaluated over different ranges of absorption duties and solution and vapor flow rates. Therefore, heat and mass transfer models developed for each configuration were used to design a representative absorber for a 10.5-kW cooling capacity chiller for residential applications within the same overall envelope. In the presence of surfactants, the bubble absorber was found to be the most optimal choice based on the performance, cost, and ease of fabrication.

Overall, the use of surfactants can lead to 10-25% reduction in absorber size, thus helping reduce overall system footprint, cost, and fluid inventory. The results presented in this work along with the modeling framework will aid the development of passively enhanced compact and high-heat flux heat and mass exchangers.

7.1 Recommendations for future work

The present study provided many insights into the mechanisms that lead to enhanced heat and mass transfer during ammonia-water absorption due to the addition of

surfactants. However, during the course of this study, several avenues for further research were revealed.

The interfacial area of two-phase flow is significantly affected by the presence of surfactants. Correlations from the literature had a prediction accuracy of at best $\pm 25\%$, which can be a source of uncertainty for the design of absorbers. There is a need to develop either correlations based on experimental data or simplified analytical solutions for predicting interfacial area in the presence of surfactants. In addition, the computer vision techniques used in the current study are not applicable at higher vapor superficial velocities. At high vapor flow rates, dispersed churn flow was observed for which visual information could not be obtained due to a high degree of reflection from the large number of bubbles at the circumference of the tubes. For such cases, methods used in this study are not suitable. There is a need to develop alternate non-intrusive methods to measure interfacial areas at high vapor flow rates.

The driving concentration and temperature gradients in each phase can vary significantly with changes in the operating conditions. In the present work, experimental data were measured at the component level and the results were interpreted accordingly. However, local temperatures and concentrations at various points within an absorber should be measured to improve the understanding of local phenomena.

In the present study, although surfactants improved absorber performance in both the falling-film and bubble absorbers, the mechanisms that led to the enhancement were different. Thus, the configuration and geometry of the absorber have a significant effect on the interactions between the surfactant and ammonia-water mixture. Further investigations

of surfactant-enhanced absorption are recommended for horizontal falling-film absorbers, plate heat exchangers as absorbers, microchannel absorbers, and bubble absorbers with spargers at vapor inlet.

The long-term stability and impact of adding surfactants to absorption heat pumps need to be determined. Prototypes should be tested in real world conditions for extended periods of time to assess the need to replenish surfactants over certain periods of time. This understanding will be critical to enable compact, efficient, and reliable absorption heat pumps.

APPENDIX A. DATA REDUCTION AND UNCERTAINTY PROPAGATION

The analysis of a representative data point from the bubble absorber heat and mass transfer experiments is described in detail in this appendix. The data reduction and propagation of experimental uncertainty calculations were performed on the Engineering Equation solver (Klein, 2018) platform. The uncertainty propagation is based on the method suggested by Taylor and Kuyatt (1994), as shown in Equation (1).

$$U_y^2 = \left(\frac{\partial y}{\partial x_1} U_{x_1} \right)^2 + \left(\frac{\partial y}{\partial x_2} U_{x_2} \right)^2 + \left(\frac{\partial y}{\partial x_3} U_{x_3} \right)^2 + \dots \quad (1)$$

where the uncertainty (U) of a calculated variable (y) is a function of the variables used in the calculation (x). The uncertainties of each flow meter and pressure transducer are individually input. The uncertainties of measurement sensors including flow meters, pressure transducers and T-type thermocouples are used based on vendor specifications and are shown in Table 4.1. An uncertainty of 25% was assigned to the estimation of the coupling-fluid thermal resistance from correlations, as seen in previous similar studies (Fronk, 2014).

A.1 Data reduction for a sample point

Inputs	Equations	Results
Coupling fluid analysis		
$P_{CF} = 103.4 \text{ kPa}$ $\dot{m}_{CF} = 8.83 \times 10^{-3} \text{ kg s}^{-1}$ $T_{CF,in} = 20.79^\circ\text{C}$ $T_{CF,out} = 22.93^\circ\text{C}$	$T_{CF,avg} = \frac{T_{CF,in} + T_{CF,out}}{2}$ $\rho_{CF} = \rho(\text{Water}, T = T_{CF,avg}, P = P_{CF})$ $C_{p,CF} = c_p(\text{Water}, T = T_{CF,avg}, P = P_{CF})$ $U_{\dot{Q}_{CF}}^2 = \left(\frac{\partial \dot{Q}_{CF}}{\partial T_{CF,out}} T_{CF,out} \right)^2 + \left(\frac{\partial \dot{Q}_{CF}}{\partial T_{CF,in}} T_{CF,in} \right)^2 + \left(\frac{\partial \dot{Q}_{CF}}{\partial \dot{m}_{CF}} \dot{m}_{CF} \right)^2$ $\dot{Q}_{cf} = \dot{m}_{CF} \cdot C_{p,CF} \cdot (T_{CF,out} - T_{CF,in})$	$T_{CF,avg} = 21.86^\circ\text{C}$ $\rho_{CF} = 998 \text{ kg m}^{-3}$ $C_{p,CF} = 4.18 \text{ kJ kg}^{-1} \text{ K}^{-1}$ $\frac{\partial \dot{Q}_{CF}}{\partial T_{CF,out}} = 36.92$ $\frac{\partial \dot{Q}_{CF}}{\partial T_{CF,in}} = -36.94$ $\frac{\partial \dot{Q}_{CF}}{\partial \dot{m}_{CF}} = 8.95$ $U_{\dot{Q}_{CF}} = 10.45$ $\dot{Q}_{cf} = 79.03 \pm 10.45 \text{ W}$
Working fluid analysis		
$\dot{m}_{wat,in} = 1.149 \text{ g s}^{-1}$ $\dot{m}_{am,in} = 0.0513 \text{ g s}^{-1}$	$x_{sol} = \frac{\dot{m}_{am,in}}{\dot{m}_{sol,out}}$	$x_{sol} = 0.04275$ $h_{wat,in} = 127.5 \text{ kJ kg}^{-1}$

A.1 Data reduction for a sample point (continued)

Inputs	Equations	Results
$\dot{m}_{sol,out} = 1.199 \text{ g s}^{-1}$ $T_{wat,in} = 30.36 \text{ }^{\circ}\text{C}$ $T_{am,in} = 29.07 \text{ }^{\circ}\text{C}$ $T_{sol,out} = 35.76 \text{ }^{\circ}\text{C}$ $P_{in} = 406.7 \text{ kPa}$ $P_{out} = 407.6 \text{ kPa}$	$h_{wat,in} = f(T_{wat,in}, P_{in})$ $h_{am,in} = f(T_{am,in}, P_{in})$ $h_{sol,out} = f(T_{sol,out}, P_{out}, x_{sol})$ $\dot{Q}_{wf1} = \dot{m}_{wat,in} h_{wat,in} + \dot{m}_{am,in} h_{am,in} - \dot{m}_{sol,out} h_{sol,out}$ $\dot{Q}_{wf2} = \dot{m}_{wat,in} h_{wat,in} + (\dot{m}_{sol,out} - \dot{m}_{wat,in}) h_{am,in} - \dot{m}_{sol,out} h_{sol,out}$	$h_{am,in} = 1543 \text{ kJ kg}^{-1}$ $h_{sol,out} = 121.9 \text{ kJ kg}^{-1}$ $\dot{Q}_{wf1} = 79.33 \text{ W}$ $\dot{Q}_{wf2} = 77.46 \text{ W}$
Annulus heat transfer coefficient		
$D_{io} = 0.01656 \text{ m}$ $D_{oi} = 0.0127 \text{ m}$ $\dot{m}_{CF} = 8.83 \times 10^{-3} \text{ kg s}^{-1}$ $T_{CF,avg} = 21.86 \text{ }^{\circ}\text{C}$ $\rho_{CF} = 998 \text{ kg m}^{-3}$	$A_a = \pi \cdot \frac{D_{io}^2 - D_{oi}^2}{4}$ $V_a = \frac{\dot{m}_{CF}}{\rho_{CF} \cdot A_a}$ $\mu_{CF} = \mu(\text{Water}, T = T_{CF,avg}, P = P_{CF})$ $k_{CF} = k(\text{Water}, T = T_{CF,avg}, P = P_{CF})$	$A_a = 8.87 \times 10^{-5} \text{ m}^2$ $V_a = 0.0997 \text{ m s}^{-1}$ $\mu_{CF} = 9.56 \times 10^{-4} \text{ kg m}^{-1} \text{ s}^{-1}$ $k_{CF} = 0.601 \text{ W m}^{-1} \text{ K}^{-1}$ $Re_a = 401.2$ $D_h = 0.00386 \text{ m}$

A.1 Data reduction for a sample point (continued)		
Inputs	Equations	Results
$D_{io} = 0.01656 \text{ m}$ $D_{oi} = 0.0127 \text{ m}$ $\dot{m}_{CF} = 8.83 \times 10^{-3} \text{ kg s}^{-1}$ $T_{CF,avg} = 21.86^\circ\text{C}$ $\rho_{CF} = 998 \text{ kg m}^{-3}$	$Re_a = \frac{\rho_{CF} \cdot V_a \cdot D_h}{\mu_{CF}}$ $D_h = D_{io} - D_{oi}$ $r_{star} = \frac{D_{oi}}{D_{io}}$ $f_a = 96 \cdot \frac{r_{star}^{0.035}}{Re_a}$ $Nu_a = \frac{1}{0.186 + 0.029 \cdot \ln(r_{star}) - 0.008 \cdot (\ln(r_{star}))^2}$ $\alpha_{CF} = Nu_a \frac{k_{CF}}{D_h}$	$r_{star} = 0.7669$ $f_a = 0.2371$ $Nu_a = 5.626$ $\alpha_{CF} = 876.2 \text{ W m}^{-2} \text{ K}^{-1}$
Thermal resistance		
$D_{io} = 0.0127 \text{ m}$ $D_{ii} = 0.01092 \text{ m}$ $k_{SS} = 14.76 \text{ W m}^{-1} \text{ K}^{-1}$	$R_{cond} = \frac{\ln(D_{io} / D_{ii})}{2 \cdot \pi \cdot k_{SS} \cdot Length}$	$R_{cond} = 0.005335 \text{ K W}^{-1}$ $LMTD = 20.58^\circ\text{C}$

Length = 0.30 m		$UA = 3.84 \text{ W K}^{-1}$
-----------------	--	------------------------------

A.1 Data reduction for a sample point (continued)

Inputs	Equations	Results
$T_{mix,in} = 50.38^\circ\text{C}$ $T_{conc,out} = 35.76^\circ\text{C}$ $T_{CF,in} = 20.79^\circ\text{C}$ $T_{CF,out} = 22.93^\circ\text{C}$	$LMTD = \frac{(T_{mix,in} - T_{CF,out}) - (T_{conc,out} - T_{CF,in})}{\ln \left[\frac{(T_{mix,in} - T_{CF,out})}{(T_{conc,out} - T_{CF,in})} \right]}$ $UA = \frac{\dot{Q}_{CF}}{LMTD}$ $A_{CF} = \pi \cdot D_{io} \cdot Length$ $R_{CF} = \frac{1}{\alpha_{CF} \cdot A_{CF}}$ $R_{sol} = \frac{1}{UA} - R_{cond} - R_{cf}$ $\alpha_{app} = \frac{1}{R_{sol} \cdot A_{sol,app}}$	$A_{CF} = 0.01586 \text{ m}^2$ $R_{CF} = 0.07197 \text{ K W}^{-1}$ $R_{sol} = 0.1831 \pm 0.034 \text{ K W}^{-1}$ $\alpha_{app} = 522.1 \pm 97.5 \text{ W m}^{-2} \text{ K}^{-1}$

APPENDIX B. MODEL SAMPLE CALCULATION

Detailed sample calculations of the segmental heat and mass transfer model for the bubble absorber are discussed here. The representative values shown here correspond to the data collected on March 2, Test # 4. The calculations shown are for the first segment in the heat transfer section. The outputs from the last segment of the adiabatic section are used as inputs in this segment.

A.2 Model sample calculations

Inputs	Equations	Results
Bulk properties		
$T_{sol,in} = 38.9^{\circ}\text{C}$ $T_{sol,out} = 51.21^{\circ}\text{C}$ $x_{sol,in} = 0.003$ $x_{sol,out} = 0.006451$ $T_{vap,in} = 43.2^{\circ}\text{C}$ $T_{vap,out} = 46.23^{\circ}\text{C}$ $x_{vap,in} = 0.9989$ $x_{vap,out} = 0.9804$	$T_{sol,bulk} = \frac{T_{sol,in} + T_{sol,out}}{2}$ $x_{sol,bulk} = \frac{x_{sol,in} + x_{sol,out}}{2}$ $T_{vap,bulk} = \frac{T_{vap,in} + T_{vap,out}}{2}$ $x_{vap,bulk} = \frac{x_{vap,in} + x_{vap,out}}{2}$	$T_{sol,bulk} = 45.05^{\circ}\text{C}$ $x_{sol,bulk} = 0.004726$ $T_{vap,bulk} = 44.71^{\circ}\text{C}$ $x_{vap,bulk} = 0.9896$
Thermophysical properties		
$T_{vap,bulk} = 44.71^{\circ}\text{C}$ $x_{vap,bulk} = 0.9896$ $P_{vap,bulk} = 307.3 \text{ kPa}$ $T_{sol,bulk} = 45.05^{\circ}\text{C}$ $x_{sol,bulk} = 0.004726$	$\mu_{vap,bulk} = f(T_{vap,bulk}, P_{vap,bulk}, x_{vap,bulk})$ $k_{vap,bulk} = f(T_{vap,bulk}, P_{vap,bulk}, x_{vap,bulk})$ $Cp_{vap,bulk} = f(T_{vap,bulk}, P_{vap,bulk}, x_{vap,bulk})$ $D_{aw,vap,bulk} = f(T_{vap,bulk}, P_{vap,bulk}, x_{vap,bulk})$ $\mu_{sol,bulk} = f(T_{sol,bulk}, x_{sol,bulk})$	$\mu_{vap,bulk} = 1.12 \times 10^{-5} \text{ kg m}^{-1} \text{ s}^{-1}$ $k_{vap,bulk} = 0.03132 \text{ W m}^{-1} \text{ K}^{-1}$ $Cp_{vap,bulk} = 2.334 \text{ kJ kg}^{-1} \text{ K}^{-1}$ $D_{aw,vap,bulk} = 1.049 \times 10^{-5} \text{ m}^2 \text{ s}^{-1}$ $\mu_{sol,bulk} = 5.885 \times 10^{-4} \text{ kg m}^{-1} \text{ s}^{-1}$

A.2 Model sample calculations

Inputs	Equations	Results
	$k_{sol,bulk} = f(T_{sol,bulk}, x_{sol,bulk})$ $Cp_{sol,bulk} = f(T_{sol,bulk}, x_{sol,bulk})$ $D_{aw,sol,bulk} = f(T_{sol,bulk}, x_{sol,bulk})$ $\sigma_{sol,bulk} = f(T_{sol,bulk}, x_{sol,bulk})$	$k_{sol,bulk} = 0.6366 \text{ W m}^{-1} \text{ K}^{-1}$ $Cp_{sol,bulk} = 4.172 \text{ kJ kg}^{-1} \text{ K}^{-1}$ $D_{aw,sol,bulk} = 3.13 \times 10^{-9} \text{ m}^2 \text{ s}^{-1}$ $\sigma_{sol,bulk} = 0.0593 \text{ N m}^{-1}$
Vapor transfer coefficients		
$D_{ii} = 0.01092 \text{ m}$ $\dot{m}_{vap} = 5.132 \times 10^{-5} \text{ kg s}^{-1}$ $\mu_{vap,bulk} = 1.12 \times 10^{-5} \text{ kg m}^{-1} \text{ s}^{-1}$ $k_{vap,bulk} = 0.03132 \text{ W m}^{-1} \text{ K}^{-1}$ $Cp_{vap,bulk} = 2.334 \text{ kJ kg}^{-1} \text{ K}^{-1}$ $D_{aw,vap,bulk} = 1.049 \times 10^{-5} \text{ m}^2 \text{ s}^{-1}$	$Pr_{vap} = \frac{\mu_{vap,bulk} \cdot Cp_{vap,bulk}}{k_{vap,bulk}}$ $Sc_{vap} = \frac{\mu_{vap,bulk}}{\rho_{vap,bulk} D_{aw,vap,bulk}}$ $G_{vap} = \frac{4\dot{m}_{vap}}{\pi D_{ii}^2}$ $Re_{vap} = G_{vap} \frac{D_{ii}}{\mu_{vap,bulk}}$ $Nu_{vap} = 4.36 \text{ (flow is laminar)}$ $\frac{Sh_{vap}}{Nu_{vap}} = \left(\frac{Sc_{vap}}{Pr_{vap}} \right)^{0.33}$	$Pr_{vap} = 0.831$ $Sc_{vap} = 0.5225$ $G_{vap} = 0.547 \text{ kg m}^{-2} \text{ s}^{-1}$ $Re_{vap} = 533.8$ $Sh_{vap} = 3.735$ $\alpha_{vap} = 12.5 \text{ W m}^{-2} \text{ K}^{-1}$ $\beta_{vap} = 0.00358 \text{ m s}^{-1}$

A.2 Model sample calculations

Inputs	Equations	Results
	$\alpha_{vap} = \frac{Nu_{vap} \cdot k_{vap,bulk}}{D_{ii}}$ $\beta_{vap} = Sh_{vap} \cdot D_{aw,vap,bulk} / D_{ii}$	
Solution transfer coefficients		
$P_{sol,bulk} = 307.3 \text{ kPa}$ $P_{crit} = 18780 \text{ kPa}$ $D_{ii} = 0.01092 \text{ m}$ $q_{avg} = 0.04275$	$Pr_{sol} = \frac{\mu_{sol,bulk} \cdot Cp_{sol,bulk}}{k_{sol,bulk}}$ $\alpha_{LO,sol} = 0.023 \cdot \frac{k_{sol,bulk}}{D_{ii}} \cdot Re_{sol}^{0.8} \cdot Pr_{sol}^{0.4}$ $\alpha_{sol} = \alpha_{LO,sol} \cdot \left((1 - q_{avg})^{0.8} + 3.8 \cdot q_{avg}^{0.76} \cdot \frac{(1 - q_{avg})^{0.04}}{(P_{sol,in} / P_{cr})^{0.38}} \right)$ $\beta_{sol} = (0.5 \cdot D_{aw,sol,bulk} / d_b) \cdot (\mu_{sol,bulk} / \rho_{sol,bulk} D_{aw,sol,bulk})^{0.5} \cdot \left(g \cdot \frac{d_b^3}{\mu_{sol,bulk}^2 \cdot \rho_{sol,bulk}^2} \right)^{0.25} \cdot \left(g \cdot \frac{d_b^2}{\sigma_{sol,in} \cdot \rho_{sol,bulk}} \right)^{3/8}$	$Pr_{sol} = 3.87$ $\alpha_{LO,sol} = 176.8 \text{ W m}^{-2} \text{ K}^{-1}$ $\alpha_{sol} = 462.4 \text{ W m}^{-2} \text{ K}^{-1}$ $\beta_{sol} = 0.0001869 \text{ m s}^{-1}$

A.2 Model sample calculations

Inputs	Equations	Results
Molar concentrations		
$x_{sol,bulk} = 0.004726$ $x_{vap,bulk} = 0.9896$ $x_{sol,int,bulk} = 0.3054$ $x_{vap,int,bulk} = 0.9423$ $M_a = 17.03 \text{ kg kmol}^{-1}$ $M_w = 18.02 \text{ kg kmol}^{-1}$	$\tilde{x} = \frac{\frac{x}{M_a}}{\left(\frac{x}{M_a}\right) + \left(\frac{1-x}{M_w}\right)}$	$\tilde{x}_{sol,bulk} = 0.00499$ $\tilde{x}_{vap,bulk} = 0.9902$ $\tilde{x}_{sol,int,bulk} = 0.3175$ $\tilde{x}_{vap,int,bulk} = 0.9453$
Mass transfer		
$\tilde{x}_{sol,bulk} = 0.00499$ $\tilde{x}_{vap,bulk} = 0.9902$ $\tilde{x}_{sol,int,bulk} = 0.3175$ $\tilde{x}_{vap,int,bulk} = 0.9453$ $\beta_{sol} = 0.0001869 \text{ m s}^{-1}$ $\beta_{vap} = 0.00358 \text{ m s}^{-1}$	$\dot{n}_T'' = \beta_{vap} \times C_{vap,T} \times \ln \left(\frac{\tilde{z} - \tilde{x}_{vap,int,bulk}}{\tilde{z} - \tilde{x}_{vap,bulk}} \right)$ $\dot{n}_T'' = \beta_{sol} \times C_{sol,T} \times \ln \left(\frac{\tilde{z} - \tilde{x}_{sol,bulk}}{\tilde{z} - \tilde{x}_{sol,int}} \right)$ $\dot{n}_A'' = \tilde{z} \times \dot{n}_T''$ $\dot{n}_W'' = (1 - \tilde{z}) \dot{n}_T''$	$\dot{n}_T'' = 6.298 \times 10^{-5} \text{ kmol m}^{-2} \text{ s}^{-1}$ $\tilde{z} = 1.267 \text{ (solved iteratively)}$ $\dot{n}_A'' = 7.98 \times 10^{-5} \text{ kmol m}^{-2} \text{ s}^{-1}$ $\dot{n}_W'' = -1.68 \times 10^{-5} \text{ kmol m}^{-2} \text{ s}^{-1}$

A.2 Model sample calculations

Inputs	Equations	Results
Interfacial area		
$\rho_{sol,bulk} = 994.5 \text{ kg m}^{-3}$ $\rho_{vap,bulk} = 2.045 \text{ kg m}^{-3}$ $q_{avg} = 0.04275$ $g = 9.8 \text{ m s}^{-2}$ $j_f = 0.0123 \text{ m s}^{-1}$ $D_{ii} = 0.01092 \text{ m}$	$S_{zivi} = (\rho_{sol,bulk} / \rho_{vap,bulk})^{1/3}$ $\Delta\rho = \rho_{sol,bulk} - \rho_{vap,bulk}$ $\alpha = \frac{1}{1 + \left(\frac{1 - q_{avg}}{q_{avg}} \right) \cdot \frac{\rho_{vap,bulk}}{\rho_{sol,bulk}} \cdot S_{zivi}}$ $j_f^* = \frac{j_f}{\left(\sigma_{sol} \cdot g \cdot \frac{\Delta\rho}{\rho_{sol,bulk}^2} \right)^{0.25}}$ $\alpha_{1,max} = 0.235 + 0.011 \cdot j_f^*$ $\alpha_{1,crit} = 0.511 + 0.006 \cdot j_f^*$ $\alpha_{1,base} = 0.099 - 0.009 \cdot j_f^*$ $\alpha_1 = \alpha_{1,max} + \frac{\alpha_{1,max} - \alpha_{1,base}}{\alpha_{1,max} - \alpha_{1,crit}} \cdot (\alpha - \alpha_{1,max})$ $1 - \alpha_{GS} = \frac{1 - \alpha}{1 - \alpha + \alpha_1}$	$S_{zivi} = 7.86$ $\Delta\rho = 992.5 \text{ kg m}^{-3}$ $\alpha = 0.7342$ $j_f^* = 0.079$ $\alpha_{1,max} = 0.2359$ $\alpha_{1,crit} = 0.5115$ $\alpha_{1,base} = 0.09829$ $\alpha_1 = 0.09829$ $\alpha_{GS} = 0.27$ $Lo = 0.00247 \text{ m}$ $Y_{MS} = 0.5035$ $\phi_{LO} = 0.9439$ $\varepsilon = 2.298 \text{ m}^2 \text{ s}^{-3}$ $N_{Re} = 744.6$

A.2 Model sample calculations

Inputs	Equations	Results
	$Lo = \sqrt{\frac{\sigma_l}{g \cdot \Delta \rho}}$ $Y_{MS} = \frac{\left(\frac{dP}{dx}\right)_{GO}}{\left(\frac{dP}{dx}\right)_{LO}}$ $\phi_{LO} = q_{avg}^3 \cdot Y_{MS} + (1 - q_{avg})^{0.33} \cdot (1 + 2 \cdot q_{avg} \cdot (Y_{MS} - 1))$ $\varepsilon = \varepsilon_B \cdot \exp(-A \cdot Re_l) + \varepsilon_F \cdot (1 - \exp(-A \cdot Re_l))$ $N_{Re} = \varepsilon^{1/3} \cdot \frac{Lo^{4/3}}{v_l}$ $N_{Lo} = \frac{Lo}{D_{ii}}$ $N_D = 1.99 \cdot N_{Lo}^{-0.335} \cdot N_{Re}^{-0.239}$ $D_{sm,o} = N_D \cdot Lo$ $IAC = 4.5 \cdot \frac{C_t}{D_{ii}} \cdot \left(\frac{\alpha - \alpha_{GS}}{1 - \alpha_{GS}}\right) + 6 \cdot \frac{\alpha_{GS}}{D_{sm,o}} \cdot \left(\frac{1 - \alpha}{1 - \alpha_{GS}}\right)$ $A_{int} = IAC \times Vol$	$N_{Lo} = 0.2261$ $N_D = 0.6741$ $D_{sm,o} = 0.0016 \text{ m}$ $IAC = 616.2 \text{ m}^{-1}$ $A_{int} = 0.002933 \text{ m}^2$

A.2 Model sample calculations

Inputs	Equations	Results
Mass and species conservation		
$A_{\text{int}} = 0.002933 \text{ m}^2$ $M_a = 17.03 \text{ kg kmol}^{-1}$ $M_w = 18.02 \text{ kg kmol}^{-1}$ $\dot{n}_A'' = 7.98 \times 10^{-5} \text{ kmol m}^{-2} \text{ s}^{-1}$ $\dot{n}_W'' = -1.68 \times 10^{-5} \text{ kmol m}^{-2} \text{ s}^{-1}$	$\dot{m}_{\text{abs},A} = \dot{n}_A'' \cdot A_{\text{int}} \cdot M_A$ $\dot{m}_{\text{abs},W} = \dot{n}_W'' \cdot A_{\text{int}} \cdot M_W$ $\dot{m}_{\text{vap},\text{out}} = \dot{m}_{\text{vap},\text{in}} - \dot{m}_{\text{abs},A} - \dot{m}_{\text{abs},W}$ $x_{\text{vap},\text{out}} = \frac{\dot{m}_{\text{vap},\text{in}} \cdot x_{\text{vap},\text{in}} - \dot{m}_{\text{abs},A}}{\dot{m}_{\text{vap},\text{out}}}$ $\dot{m}_{\text{sol},\text{out}} + \dot{m}_{\text{vap},\text{out}} = \dot{m}_{\text{sol},\text{in}} + \dot{m}_{\text{vap},\text{in}}$ $\dot{m}_{\text{sol},\text{out}} \cdot x_{\text{sol},\text{out}} + \dot{m}_{\text{vap},\text{out}} \cdot x_{\text{vap},\text{out}} = \dot{m}_{\text{sol},\text{in}} \cdot x_{\text{sol},\text{in}} + \dot{m}_{\text{vap},\text{in}} \cdot x_{\text{vap},\text{in}}$	$\dot{m}_{\text{abs},A} = 3.986 \times 10^{-6} \text{ kg s}^{-1}$ $\dot{m}_{\text{abs},W} = -8.87 \times 10^{-7} \text{ kg s}^{-1}$ $\dot{m}_{\text{vap},\text{out}} = 4.822 \times 10^{-5} \text{ kg s}^{-1}$ $x_{\text{vap},\text{out}} = 0.9804$ $\dot{m}_{\text{sol},\text{out}} = 0.001152 \text{ kg s}^{-1}$ $x_{\text{sol},\text{out}} = 0.006451$
Energy balance		
$T_{\text{vap},\text{int},\text{in}} = 44.52 \text{ }^\circ\text{C}$ $T_{\text{vap},\text{in}} = 43.2 \text{ }^\circ\text{C}$ $T_{\text{vap},\text{int},\text{out}} = 75.86 \text{ }^\circ\text{C}$ $T_{\text{sol},\text{in}} = 38.9 \text{ }^\circ\text{C}$ $T_{\text{CF},\text{out},\text{seg}} = 22.93 \text{ }^\circ\text{C}$ $A_{\text{int}} = 0.002933 \text{ m}^2$	$LMTD_{\text{vap}} = \frac{(T_{\text{vap},\text{int},\text{in}} - T_{\text{vap},\text{in}}) - (T_{\text{vap},\text{int},\text{out}} - T_{\text{vap},\text{out}})}{\ln \left[\frac{(T_{\text{vap},\text{int},\text{in}} - T_{\text{vap},\text{in}})}{(T_{\text{vap},\text{int},\text{out}} - T_{\text{vap},\text{out}})} \right]}$ $LMTD_{\text{wet}} = \frac{(T_{\text{sol},\text{in}} - T_{\text{CF},\text{out},\text{seg}}) - (T_{\text{sol},\text{out}} - T_{\text{CF},\text{in},\text{seg}})}{\ln \left[\frac{(T_{\text{sol},\text{in}} - T_{\text{CF},\text{out},\text{seg}})}{(T_{\text{sol},\text{out}} - T_{\text{CF},\text{in},\text{seg}})} \right]}$	$T_{\text{vap},\text{out}} = 46.23 \text{ }^\circ\text{C}$ $LMTD_{\text{vap}} = 9.1 \text{ K}$ $LMTD_{\text{wet}} = 21.57 \text{ K}$ $\phi_T = 0.1675$ $\dot{Q}_{\text{vap}} = 0.3624 \text{ W}$ $R_{\text{CF}} = 2.246 \text{ K W}^{-1}$

A.2 Model sample calculations

Inputs	Equations	Results
$\alpha_{vap} = 12.5 \text{ W m}^{-2} \text{ K}^{-1}$ $\alpha_{CF} = 878.8 \text{ W m}^{-2} \text{ K}^{-1}$	$\phi_T = \frac{\dot{n}_A'' \cdot C_{p,a,molar} + \dot{n}_W'' \cdot C_{p,w,molar}}{\alpha_{vap}}$ $\dot{Q}_{vap} = \alpha_{vap} \cdot \left(\frac{\phi_T}{1 - \exp(-\phi_T)} \right) \cdot (A_{int}) \cdot LMTD_{vap}$ $R_{CF} = \frac{1}{\alpha_{CF} \cdot A_{o,seg}}$ $R_{cond} = \frac{\ln(D_{io} / D_{ii})}{2 \cdot \pi \cdot k_{ss} \cdot Length}$ $R_{sol} = \frac{1}{\alpha_{sol} \cdot A_{i,seg}}$ $R_{total} = R_{CF} + R_{sol} + R_{cond}$ $UA_{seg} = 1 / R_{total}$ $\dot{Q}_{abs} = UA_{seg} \cdot LMTD_{wet}$ $\dot{m}_{sol,in} \cdot h_{sol,in} + \dot{m}_{vap,in} \cdot h_{vap,in} - \dot{Q}_{abs} = \dot{m}_{sol,out} \cdot h_{sol,in} + \dot{m}_{vap,out} \cdot h_{vap,out}$ $\dot{Q}_{vap} = \dot{m}_{vap,in} \cdot Cp_{vap,bulk} \cdot (T_{vap,out} - T_{vap,in})$ <p>ui</p>	$R_{cond} = 0.1276 \text{ K W}^{-1}$ $R_{sol} = 4.963 \text{ K W}^{-1}$ $R_{total} = 7.336 \text{ K W}^{-1}$ $UA_{seg} = 0.1363 \text{ W K}^{-1}$ $\dot{Q}_{abs} = 2.941 \text{ W}$ $T_{CF,in,seg} = 22.85^\circ\text{C}$

A.2 Model sample calculations

Inputs	Equations	Results
Wall temperatures		
$T_{sol,in} = 38.9^{\circ}\text{C}$ $T_{CF,out,seg} = 22.93^{\circ}\text{C}$ $T_{CF,in,seg} = 22.85^{\circ}\text{C}$ $\alpha_{CF} = 878.8 \text{ W m}^{-2} \text{ K}^{-1}$ $\alpha_{sol} = 462.4 \text{ W m}^{-2} \text{ K}^{-1}$ $D_{ii} = 0.01092 \text{ m}$ $D_{io} = 0.0127 \text{ m}$ $T_{sol,int,out} = 75.86^{\circ}\text{C}$	$LMTD_{sol} = \frac{(T_{sol,in} - T_{wall,in}) - (T_{sol,out} - T_{wall,out})}{\ln \left[\frac{(T_{sol,in} - T_{wall,in})}{(T_{sol,out} - T_{wall,out})} \right]}$ $LMTD_{wet} = \frac{(T_{wall,in} - T_{CF,out,seg}) - (T_{wall,out} - T_{CF,in,seg})}{\ln \left[\frac{(T_{wall,in} - T_{CF,out,seg})}{(T_{wall,out} - T_{CF,in,seg})} \right]}$ $\dot{Q}_{CF} = \alpha_{sol} \cdot A_{i,seg} \cdot LMTD_{sol}$ $\dot{Q}_{CF} = U_{CF,wall} \cdot A_{o,seg} \cdot LMTD_{CF}$ $R_{cond,o} = D_{ii} \cdot \frac{\ln(D_{io} / D_{ii})}{2 \cdot k_{SS}}$ $\frac{1}{U_{CF,wall}} = \frac{1}{\alpha_{CF}} + R_{cond,o}$ $T_{sol,out} = \frac{T_{sol,int,out} + T_{wall,out}}{2}$	$LMTD_{sol} = 14.59 \text{ K}$ $LMTD_{wet} = 21.57 \text{ K}$ $T_{wall,out} = 26.55^{\circ}\text{C}$ $T_{sol,out} = 51.21^{\circ}\text{C}$

REFERENCES

- Agble, D. and M. A. Mendes-Tatsis (2000), "The effect of surfactants on interfacial mass transfer in binary liquid–liquid systems," *International Journal of Heat and Mass Transfer*. Vol. 43(6), pp. 1025-1034 DOI: [https://doi.org/10.1016/S0017-9310\(99\)00184-2](https://doi.org/10.1016/S0017-9310(99)00184-2).
- AHRI (2008). *Performance rating of unitary air-conditioning & air-source heat pump equipment*. AHRI Standard, Vol. 210 p. 240.
- Akita, K. and F. Yoshida (1974), "Bubble Size, Interfacial Area, and Liquid-Phase Mass Transfer Coefficient in Bubble Columns," *Industrial & Engineering Chemistry Process Design and Development*. Vol. 13(1), pp. 84-91 DOI: 10.1021/i260049a016.
- Altamirano, A., B. Stutz and N. Le Pierrès (2020), "Review of small-capacity single-stage continuous absorption systems operating on binary working fluids for cooling: Compact exchanger technologies," *International Journal of Refrigeration*. Vol. 114, pp. 118-147 DOI: <https://doi.org/10.1016/j.ijrefrig.2020.02.033>.
- Amani, P., S. Hurter, V. Rudolph and M. Firouzi (2020), "Comparison of flow dynamics of air-water flows with foam flows in vertical pipes," *Experimental Thermal and Fluid Science*. Vol. 119, p. 110216 DOI: <https://doi.org/10.1016/j.expthermflusci.2020.110216>.
- Amaris, C., M. Vallès and M. Bourouis (2018), "Vapour absorption enhancement using passive techniques for absorption cooling/heating technologies: A review," *Applied Energy*. Vol. 231, pp. 826-853 DOI: <https://doi.org/10.1016/j.apenergy.2018.09.071>.
- ASME (2021). *Boiler and Pressure Vessel Code*. American Society of Mechanical Engineers, New York.
- Bell, K. J. and M. A. Ghaly (1973). *An approximate generalized design method for multicomponent/partial condensers*. AIChE Symposium Series Heat Transfer Research, Vol. 69 pp. 72-79.
- Bell, K. J., R. Shah, E. Subbarao and R. Mashelkar (1988), "Delaware method for shell-side design," *Heat Transfer Equipment Design*, Hemisphere Publishing, New York. p. 145.
- Ben Jaballah, R., M. B. Ben Hamida, J. Saleh and M. A. Almeshaal (2019), "Enhancement of the performance of bubble absorber using hybrid nanofluid as a cooled absorption system," *International Journal of Numerical Methods for Heat & Fluid Flow*. Vol. 29(10), pp. 3857-3871 DOI: 10.1108/HFF-05-2018-0212.

- Bergles, A. E. and R. M. Manglik (2013), "Current progress and new developments in enhanced heat and mass transfer." Vol. 20(1), pp. 1-15 DOI: 10.1615/JEnhHeatTransf.2013006989.
- Beutler, A., I. Greiter, A. Wagner, L. Hoffman, S. Schreier and G. Alefeld (1996), "Surfactants and fluid properties," *International Journal of Refrigeration*. Vol. 19(5), pp. 342-346 DOI: [https://doi.org/10.1016/S0140-7007\(96\)00034-5](https://doi.org/10.1016/S0140-7007(96)00034-5).
- Bohra, L. K., S. Lee and S. Garimella (2019), "Visual documentation of transfer processes in horizontal-tube falling-film ammonia–water absorbers," *International Journal of Refrigeration*. Vol. 103, pp. 91-105 DOI: <https://doi.org/10.1016/j.ijrefrig.2019.03.032>.
- Bradski, G. and A. Kaehler (2008). *Learning OpenCV: Computer vision with the OpenCV library*. O'Reilly Media, Newton, MA.
- Brian, P. L. T., J. E. Vivian and S. T. Mayr (1971), "Cellular Convection in Desorbing Surface Tension-Lowering Solutes from Water," *Industrial & Engineering Chemistry Fundamentals*. Vol. 10(1), pp. 75-83 DOI: 10.1021/i160037a014.
- Bung, D. B. and D. Valero (2016), "Optical flow estimation in aerated flows," *Journal of Hydraulic Research*. Vol. 54(5), pp. 575-580 DOI: 10.1080/00221686.2016.1173600.
- Castro, J., C. Oliet, I. Rodríguez and A. Oliva (2009), "Comparison of the performance of falling film and bubble absorbers for air-cooled absorption systems," *International Journal of Thermal Sciences*. Vol. 48(7), pp. 1355-1366 DOI: <https://doi.org/10.1016/j.ijthermalsci.2008.11.021>.
- Cerezo, J., R. Best and R. J. Romero (2011), "A study of a bubble absorber using a plate heat exchanger with $\text{NH}_3\text{--H}_2\text{O}$, $\text{NH}_3\text{--LiNO}_3$ and $\text{NH}_3\text{--NaSCN}$," *Applied Thermal Engineering*. Vol. 31(11), pp. 1869-1876 DOI: <https://doi.org/10.1016/j.applthermaleng.2011.02.032>.
- Cerezo, J., M. Bourouis, M. Vallès, A. Coronas and R. Best (2009), "Experimental study of an ammonia–water bubble absorber using a plate heat exchanger for absorption refrigeration machines," *Applied Thermal Engineering*. Vol. 29(5), pp. 1005-1011 DOI: <https://doi.org/10.1016/j.applthermaleng.2008.05.012>.
- Chandrasekaran, S., M. Hughes, G. Kini and S. Garimella (2020), "A Microchannel Shell-And-Tube Absorber for Ammonia-Water Absorption," *Applied Thermal Engineering*. p. 116321 DOI: <https://doi.org/10.1016/j.applthermaleng.2020.116321>.
- Cheng, L., D. Mewes and A. Luke (2007), "Boiling phenomena with surfactants and polymeric additives: A state-of-the-art review," *International Journal of Heat and Mass Transfer*. Vol. 50(13), pp. 2744-2771 DOI: <https://doi.org/10.1016/j.ijheatmasstransfer.2006.11.016>.

- Colburn, A. P. and T. B. Drew (1937), "The condensation of mixed vapors," *Transactions of American Institute of Chemical Engineers*. Vol. 33, pp. 197-215.
- Darwish, N. A., S. H. Al-Hashimi and A. S. Al-Mansoori (2008), "Performance analysis and evaluation of a commercial absorption–refrigeration water–ammonia (ARWA) system," *International Journal of Refrigeration*. Vol. 31(7), pp. 1214-1223 DOI: <https://doi.org/10.1016/j.ijrefrig.2008.02.005>.
- Dejesus, J. and M. Kawaji (1990), "Investigation of interfacial area and void fraction in upward, cocurrent gas-liquid flow," *The Canadian Journal of Chemical Engineering*. Vol. 68(6), pp. 904-912 DOI: <https://doi.org/10.1002/cjce.5450680603>.
- Determan, M. D. and S. Garimella (2012), "Design, fabrication, and experimental demonstration of a microscale monolithic modular absorption heat pump," *Applied Thermal Engineering*. Vol. 47, pp. 119-125 DOI: <https://doi.org/10.1016/j.applthermaleng.2011.10.043>.
- Donnellan, P., K. Cronin, W. Lee, S. Duggan and E. Byrne (2014), "Absorption of steam bubbles in lithium bromide solution," *Chemical Engineering Science*. Vol. 119, pp. 10-21 DOI: <https://doi.org/10.1016/j.ces.2014.07.060>.
- Duangprasert, T., A. Sirivat, K. Siemanond and J. O. Wilkes (2008), "Vertical two-phase flow regimes and pressure gradients under the influence of SDS surfactant," *Experimental Thermal and Fluid Science*. Vol. 32(3), pp. 808-817 DOI: <https://doi.org/10.1016/j.expthermflusci.2007.10.005>.
- English, N. J. and S. G. Kandlikar (2006), "An Experimental Investigation into the Effect of Surfactants on Air-Water Two-Phase Flow in Minichannels," *Heat Transfer Engineering*. Vol. 27(4), pp. 99-109 DOI: 10.1080/01457630500523980.
- Farn, R. J. (2008). *Chemistry and technology of surfactants*. John Wiley & Sons, New York.
- Fernández-Seara, J., J. Sieres, C. Rodríguez and M. Vázquez (2005), "Ammonia–water absorption in vertical tubular absorbers," *International Journal of Thermal Sciences*. Vol. 44(3), pp. 277-288 DOI: <https://doi.org/10.1016/j.ijthermalsci.2004.09.001>.
- Ferreira, C. A. I., C. Keizer and C. H. M. Machielsen (1984), "Heat and mass transfer in vertical tubular bubble absorbers for ammonia-water absorption refrigeration systems," *International Journal of Refrigeration*. Vol. 7(6), pp. 348-357 DOI: [https://doi.org/10.1016/0140-7007\(84\)90004-5](https://doi.org/10.1016/0140-7007(84)90004-5).
- Forinash, D. (2015). *Novel air-coupled heat exchangers for waste heat-driven absorption heat pumps*. MS Thesis, Georgia Institute of Technology, Atlanta.

- Fronk, B. M. (2014). *Coupled heat and mass transfer during condensation of high-temperature-glide zeotropic mixtures in small diameter channels*. Ph.D. Thesis, Georgia Institute of Technology.
- Fronk, B. M. and S. Garimella (2016), "Condensation of ammonia and high-temperature-glide ammonia/water zeotropic mixtures in minichannels – Part I: Measurements," *International Journal of Heat and Mass Transfer*. Vol. 101, pp. 1343-1356 DOI: <https://doi.org/10.1016/j.ijheatmasstransfer.2016.05.049>.
- Fu Lin, S. J. and Z. Shigang (2011), "Experimental study on vertical vapor absorption into LiBr solution with and without additive," *Applied Thermal Engineering*. Vol. 31(14), pp. 2850-2854 DOI: <https://doi.org/10.1016/j.applthermaleng.2011.05.010>.
- García-Abuín, A., D. Gómez-Díaz, J. M. Navaza and B. Sanjurjo (2010), "Effect of surfactant nature upon absorption in a bubble column," *Chemical Engineering Science*. Vol. 65(15), pp. 4484-4490 DOI: <https://doi.org/10.1016/j.ces.2010.04.009>.
- Garimella, S. (2000), "Microchannel components for absorption space-conditioning systems," *Proceedings of Proceedings of the ASHRAE Winter Meeting*, Dallas, TX, pp. 453-462.
- Garimella, S. and R. N. Christensen (1995), "Heat Transfer and Pressure Drop Characteristics of Spirally Fluted Annuli: Part II—Heat Transfer," *Journal of Heat Transfer*. Vol. 117(1), pp. 61-68 DOI: 10.1115/1.2822324.
- Garimella, S., D. M. Forinash and D. B. Boman (2020), "Air-cooled absorbers for extreme-ambient absorption heat pumps," *International Journal of Refrigeration*. Vol. 120, pp. 260-270 DOI: <https://doi.org/10.1016/j.ijrefrig.2020.08.023>.
- Garimella, S., C. M. Keinath, J. C. Delahanty, D. C. Hoysall, M. A. Staedter, A. Goyal and M. A. Garrabrant (2016), "Development and demonstration of a compact ammonia–water absorption heat pump prototype with microscale features for space-conditioning applications," *Applied Thermal Engineering*. Vol. 102, pp. 557-564 DOI: <https://doi.org/10.1016/j.applthermaleng.2016.03.169>.
- Garrabrant, M. A. and R. N. Christensen (1997), "Modeling and experimental verification of a Perforated Plate-Fin Absorber for aqua-ammonia absorption systems," *Proceedings of ASME International Mechanical Engineering Congress and Exposition*, Dallas, TX, USA, pp. 337-347.
- Ghiaasiaan, S. M. (2007). *Two-phase flow, boiling, and condensation: in conventional and miniature systems*. Cambridge University Press, UK.
- Giannetti, N., S. Yamaguchi and K. Saito (2018), "Numerical simulation of Marangoni convection within absorptive aqueous Li-Br," *International Journal of*

- Refrigeration*. Vol. 92, pp. 176-184 DOI:
<https://doi.org/10.1016/j.ijrefrig.2018.05.035>.
- Goel, N. and D. Y. Goswami (2005), "A Compact Falling Film Absorber," *Journal of Heat Transfer*. Vol. 127(9), pp. 957-965 DOI: 10.1115/1.1929781.
- Golovin, A. A. (1992), "Mass transfer under interfacial turbulence: kinetic regulaties," *Chemical Engineering Science*. Vol. 47(8), pp. 2069-2080 DOI:
[https://doi.org/10.1016/0009-2509\(92\)80323-5](https://doi.org/10.1016/0009-2509(92)80323-5).
- Goyal, A., M. A. Staedter, D. C. Hoysall, M. J. Ponkala and S. Garimella (2017), "Experimental evaluation of a small-capacity, waste-heat driven ammonia-water absorption chiller," *International Journal of Refrigeration*. Vol. 79, pp. 89-100 DOI: <https://doi.org/10.1016/j.ijrefrig.2017.04.006>.
- Griffith, R. M. (1962), "The effect of surfactants on the terminal velocity of drops and bubbles," *Chemical Engineering Science*. Vol. 17(12), pp. 1057-1070 DOI:
[https://doi.org/10.1016/0009-2509\(62\)80084-0](https://doi.org/10.1016/0009-2509(62)80084-0).
- Hassan, Y. A. and E. E. Dominguez-Ontiveros (2008), "Flow visualization in a pebble bed reactor experiment using PIV and refractive index matching techniques," *Nuclear Engineering and Design*. Vol. 238(11), pp. 3080-3085 DOI:
<https://doi.org/10.1016/j.nucengdes.2008.01.027>.
- Hewitt, G. F. and J. Barbosa (2008). *Heat exchanger design handbook*. Begell house New York.
- Hewitt, G. F., G. L. Shires and T. R. Bott (1994). *Process heat transfer*. CRC press Boca Raton, FL.
- Hibiki, T. and M. Ishii (2002), "Interfacial area concentration of bubbly flow systems," *Chemical Engineering Science*. Vol. 57(18), pp. 3967-3977 DOI:
[https://doi.org/10.1016/S0009-2509\(02\)00263-4](https://doi.org/10.1016/S0009-2509(02)00263-4).
- Hihara, E. and T. Saito (1993), "Effect of surfactant on falling film absorption," *International Journal of Refrigeration*. Vol. 16(5), pp. 339-346 DOI:
[https://doi.org/10.1016/0140-7007\(93\)90006-T](https://doi.org/10.1016/0140-7007(93)90006-T).
- Hoffmann, L., I. Greiter, A. Wagner, V. Weiss and G. Alefeld (1996), "Experimental investigation of heat transfer in a horizontal tube falling film absorber with aqueous solutions of LiBr with and without surfactants," *International Journal of Refrigeration*. Vol. 19(5), pp. 331-341 DOI: [https://doi.org/10.1016/S0140-7007\(96\)00026-6](https://doi.org/10.1016/S0140-7007(96)00026-6).
- Hoysall, D. C. and S. Garimella (2018), "Investigation of a serpentine micro-pin fin heat and mass exchanger for absorption systems," *International Journal of Refrigeration*. Vol. 93, pp. 108-121 DOI:
<https://doi.org/10.1016/j.ijrefrig.2018.07.012>.

- Hoysall, D. C. and S. Garimella (2019), "Investigation of a microchannel heat and mass exchanger for absorption systems," *Applied Thermal Engineering*. Vol. 148, pp. 650-661 DOI: <https://doi.org/10.1016/j.applthermaleng.2018.11.077>.
- Hoysall, D. C., K. Keniar and S. Garimella (2018), "Addressing Two-Phase Flow Maldistribution in Microchannel Heat and Mass Exchangers," *Journal of Heat Transfer*. Vol. 140(11) DOI: 10.1115/1.4040706.
- IEA (2018). "The Future of Cooling - Opportunities for energy-efficient air-conditioning," International Energy Agency.
- Imaishi, N., Y. Suzuki, M. Hozawa and K. Fujinawa (1980), "Interfacial Turbulence in Gas-Liquid Mass Transfer," *Kagaku Kogaku Ronbunshu*. Vol. 6(6), pp. 585-590 DOI: 10.1252/kakoronbunshu.6.585.
- Incropera, F., D. P. DeWitt, T. L. Bergman and A. S. Lavine (1996). *Fundamentals of heat and mass transfer*. Wiley, Hoboken, NJ.
- Inoue, T., Y. Teruya and M. Monde (2004), "Enhancement of pool boiling heat transfer in water and ethanol/water mixtures with surface-active agent," *International Journal of Heat and Mass Transfer*. Vol. 47(25), pp. 5555-5563 DOI: <https://doi.org/10.1016/j.ijheatmasstransfer.2004.05.037>.
- Ishii, M. and K. Mishima (1980). "Study of Two-fluid Model and Interfacial Area.," NUREG/CR-1873. ANL-80-111, USA.
- Ishii, M. and K. Mishima (1984), "Two-fluid model and hydrodynamic constitutive relations," *Nuclear Engineering and Design*. Vol. 82(2), pp. 107-126 DOI: [https://doi.org/10.1016/0029-5493\(84\)90207-3](https://doi.org/10.1016/0029-5493(84)90207-3).
- Jiménez-García, J. C. and W. Rivera (2019), "Parametric analysis on the experimental performance of an ammonia/water absorption cooling system built with plate heat exchangers," *Applied Thermal Engineering*. Vol. 148, pp. 87-95 DOI: <https://doi.org/10.1016/j.applthermaleng.2018.11.040>.
- Jung, C. W., S. S. An and Y. T. Kang (2014), "Thermal performance estimation of ammonia-water plate bubble absorbers for compression/absorption hybrid heat pump application," *Energy*. Vol. 75, pp. 371-378 DOI: <https://doi.org/10.1016/j.energy.2014.07.086>.
- Kandlikar, S. G. (2006). Chapter 5 - Flow boiling in minichannels and microchannels. *Heat Transfer and Fluid Flow in Minichannels and Microchannels*. S. G. Kandlikar, S. Garimella, D. Li, S. Colin and M. R. King. Elsevier Science Ltd, Oxford pp. 175-226.
- Kang, B. H., K. H. Kim and D. Y. Lee (2007), "Fluid flow and heat transfer on a falling liquid film with surfactant from a heated vertical surface," *Journal of Mechanical Science and Technology*. Vol. 21(11), p. 1807 DOI: 10.1007/BF03177436.

- Kang, Y., A. Akisawa and T. Kashiwagi (2000), "Analytical investigation of two different absorption modes: falling film and bubble types," *International Journal of Refrigeration*. Vol. 23(6), pp. 430-443 DOI: [https://doi.org/10.1016/S0140-7007\(99\)00075-4](https://doi.org/10.1016/S0140-7007(99)00075-4).
- Kang, Y. T., A. Akisawa and T. Kashiwagi (1999a), "Experimental correlation of combined heat and mass transfer for $\text{NH}_3\text{--H}_2\text{O}$ falling film absorption," *International Journal of Refrigeration*. Vol. 22(4), pp. 250-262 DOI: [https://doi.org/10.1016/S0140-7007\(98\)00076-0](https://doi.org/10.1016/S0140-7007(98)00076-0).
- Kang, Y. T., A. Akisawa and T. Kashiwagi (1999b), "Visualization and model development of Marangoni convection in $\text{NH}_3\text{--H}_2\text{O}$ system," *International Journal of Refrigeration*. Vol. 22(8), pp. 640-649 DOI: [https://doi.org/10.1016/S0140-7007\(99\)00019-5](https://doi.org/10.1016/S0140-7007(99)00019-5).
- Kang, Y. T. and R. N. Christensen (1994), "Development of a counter-current model for a vertical fluted tube GAX absorber," *Proceedings of Proceedings of the International Absorption Heat Pump Conference*, pp. 7-16.
- Kang, Y. T., R. N. Christensen, T. Kashiwagi and F. Ziegler (1998), "Ammonia-water bubble absorber with a plate heat exchanger/Discussion," *ASHRAE Transactions*. Vol. 104, p. 1565.
- Kang, Y. T. and T. Kashiwagi (2002), "Heat transfer enhancement by Marangoni convection in the $\text{NH}_3\text{--H}_2\text{O}$ absorption process," *International Journal of Refrigeration*. Vol. 25(6), pp. 780-788 DOI: [https://doi.org/10.1016/S0140-7007\(01\)00074-3](https://doi.org/10.1016/S0140-7007(01)00074-3).
- Kang, Y. T. and J.-K. Kim (2006), "Comparisons of Mechanical and Chemical Treatments and Nano Technologies for Absorption Applications," *HVAC&R Research*. Vol. 12(sup2), pp. 807-819 DOI: [10.1080/10789669.2006.10391209](https://doi.org/10.1080/10789669.2006.10391209).
- Kashiwagi, T. (1988), "Basic mechanism of absorption heat and mass transfer enhancement by the Marangoni effect," *Newsletter IEA Heat Pump Center*. Vol. 6(4), pp. 2-6.
- Kim, H. Y., B. B. Saha and S. Koyama (2003a), "Development of a slug flow absorber working with ammonia-water mixture: part I—flow characterization and experimental investigation," *International Journal of Refrigeration*. Vol. 26(5), pp. 508-515 DOI: [https://doi.org/10.1016/S0140-7007\(03\)00020-3](https://doi.org/10.1016/S0140-7007(03)00020-3).
- Kim, H. Y., B. B. Saha and S. Koyama (2003b), "Development of a slug flow absorber working with ammonia-water mixture: part II—data reduction model for local heat and mass transfer characterization," *International Journal of Refrigeration*. Vol. 26(6), pp. 698-706 DOI: [https://doi.org/10.1016/S0140-7007\(03\)00021-5](https://doi.org/10.1016/S0140-7007(03)00021-5).
- Kim, J.-K., A. Akisawa, T. Kashiwagi and Y. T. Kang (2007a), "Numerical design of ammonia bubble absorber applying binary nanofluids and surfactants,"

- International Journal of Refrigeration*. Vol. 30(6), pp. 1086-1096 DOI: <https://doi.org/10.1016/j.ijrefrig.2006.12.011>.
- Kim, J.-K., J. Y. Jung and Y. T. Kang (2007b), "Absorption performance enhancement by nano-particles and chemical surfactants in binary nanofluids," *International Journal of Refrigeration*. Vol. 30(1), pp. 50-57 DOI: <https://doi.org/10.1016/j.ijrefrig.2006.04.006>.
- Kim, J.-K., J. Y. Jung, J. H. Kim, M.-G. Kim, T. Kashiwagi and Y. T. Kang (2006), "The effect of chemical surfactants on the absorption performance during NH₃-H₂O bubble absorption process," *International Journal of Refrigeration*. Vol. 29(2), pp. 170-177 DOI: <https://doi.org/10.1016/j.ijrefrig.2005.06.006>.
- Kim, K. J., N. S. Berman and B. D. Wood (1996), "The interfacial turbulence in falling film absorption: effects of additives," *International Journal of Refrigeration*. Vol. 19(5), pp. 322-330 DOI: [https://doi.org/10.1016/S0140-7007\(96\)00025-4](https://doi.org/10.1016/S0140-7007(96)00025-4).
- Kini, G., S. Chandrasekaran, M. T. Hughes and S. Garimella (2021), "Experimental investigation of surfactant-enhanced ammonia-water absorption in a shell-and-tube absorber," *International Journal of Refrigeration*. Vol. 129, pp. 43-51 DOI: <https://doi.org/10.1016/j.ijrefrig.2021.04.034>.
- Kini, G., S. Chandrasekaran, M. Tambasco and S. Garimella (2020), "A Residential Absorption Chiller for High Ambient Temperatures," *International Journal of Refrigeration*. DOI: <https://doi.org/10.1016/j.ijrefrig.2020.08.022>.
- Kini, G. and S. Garimella (2019), "Screening of surface active agents to enhance absorption in ammonia-water systems," *Proceedings of 25th IIR International Congress of Refrigeration*, Montreal
- Kini, G. and S. Garimella (2021), "Passive enhancement of ammonia-water absorption by the addition of surfactants," *International Journal of Heat and Mass Transfer*. Vol. 176, p. 121478 DOI: <https://doi.org/10.1016/j.ijheatmasstransfer.2021.121478>.
- Klein, S. A. (2018). *Engineering Equation Solver*. F-chart software, Madison, WI.
- Kulankara, S. and K. E. Herold (2000), "Theory of Heat/Mass Transfer Additives in Absorption Chillers," *HVAC&R Research*. Vol. 6(4), pp. 369-380 DOI: 10.1080/10789669.2000.10391422.
- Kulankara, S. and K. E. Herold (2002), "Surface tension of aqueous lithium bromide with heat/mass transfer enhancement additives: the effect of additive vapor transport," *International Journal of Refrigeration*. Vol. 25(3), pp. 383-389 DOI: [https://doi.org/10.1016/S0140-7007\(01\)00013-5](https://doi.org/10.1016/S0140-7007(01)00013-5).

- Kumar, N., M. Q. Raza and R. Raj (2018), "Surfactant aided bubble departure during pool boiling," *International Journal of Thermal Sciences*. Vol. 131, pp. 105-113 DOI: <https://doi.org/10.1016/j.ijthermalsci.2018.05.025>.
- Kuo, J. T. and G. B. Wallis (1988), "Flow of bubbles through nozzles," *International Journal of Multiphase Flow*. Vol. 14(5), pp. 547-564 DOI: [https://doi.org/10.1016/0301-9322\(88\)90057-2](https://doi.org/10.1016/0301-9322(88)90057-2).
- Kurimoto, R., H. Minagawa and T. Yasuda (2019), "Effects of surfactant on gas-liquid slug flow in circular microchannels." Vol. 31(3), pp. 273-286 DOI: 10.1615/MultScienTechn.2019031945.
- Kwon, K. and S. Jeong (2004), "Effect of vapor flow on the falling-film heat and mass transfer of the ammonia/water absorber," *International Journal of Refrigeration*. Vol. 27(8), pp. 955-964 DOI: <https://doi.org/10.1016/j.ijrefrig.2004.06.009>.
- Kyung, I.-S. and K. E. Herold (2001), "Performance of Horizontal Smooth Tube Absorber With and Without 2-Ethyl-Hexanol," *Journal of Heat Transfer*. Vol. 124(1), pp. 177-183 DOI: 10.1115/1.1418366.
- Lauren, S. (2017). "Surface and interfacial tension - How to select the best measurement method," Biolin Scientific.
- Leandro, J., D. B. Bung and R. Carvalho (2014), "Measuring void fraction and velocity fields of a stepped spillway for skimming flow using non-intrusive methods," *Experiments in Fluids*. Vol. 55(5), p. 1732 DOI: 10.1007/s00348-014-1732-6.
- Lee, K. B., B. H. Chun, J. C. Lee, C. H. Lee and S. H. Kim (2002), "Experimental analysis of bubble mode in a plate-type absorber," *Chemical Engineering Science*. Vol. 57(11), pp. 1923-1929 DOI: [https://doi.org/10.1016/S0009-2509\(02\)00089-1](https://doi.org/10.1016/S0009-2509(02)00089-1).
- Lioumbas, J. S., A. A. Mouza and S. V. Paras (2006), "Effect of surfactant additives on co-current gas-liquid downflow," *Chemical Engineering Science*. Vol. 61(14), pp. 4605-4616 DOI: <https://doi.org/10.1016/j.ces.2006.02.034>.
- Lips, S. and J. P. Meyer (2012), "Experimental study of convective condensation in an inclined smooth tube. Part I: Inclination effect on flow pattern and heat transfer coefficient," *International Journal of Heat and Mass Transfer*. Vol. 55(1), pp. 395-404 DOI: <https://doi.org/10.1016/j.ijheatmasstransfer.2011.09.033>.
- Liu, L., X. Li, L. Tong and Y. Liu (2014), "Effect of surfactant additive on vertical two-phase flow," *Journal of Petroleum Science and Engineering*. Vol. 115, pp. 1-10 DOI: <https://doi.org/10.1016/j.petrol.2014.02.004>.
- Lu, H.-H., Y.-M. Yang and J.-R. Maa (1996), "Effect of Artificially Provoked Marangoni Convection at a Gas/Liquid Interface on Absorption," *Industrial & Engineering Chemistry Research*. Vol. 35(6), pp. 1921-1928 DOI: 10.1021/ie950565h.

- Lu, H.-H., Y.-M. Yang and J.-R. Maa (1997), "On the Induction Criterion of the Marangoni Convection at the Gas/Liquid Interface," *Industrial & Engineering Chemistry Research*. Vol. 36(2), pp. 474-482 DOI: 10.1021/ie960370p.
- MATLAB (2017). *MATLAB 2017b*. The Mathworks Inc, Natick, Massachusetts.
- Meacham, J. M. and S. Garimella (2004), "Ammonia-Water Absorption Heat and Mass Transfer in Microchannel Absorbers with Visual Confirmation," *ASHRAE Transactions*. Vol. 110(1).
- Milkie, J. A. (2014). *Condensation of hydrocarbon and zeotropic hydrocarbon/refrigerant mixtures in horizontal tubes*. Georgia Institute of Technology.
- Miller, W. (1999), "The synergism between heat and mass transfer additive and advanced surfaces in aqueous LiBr horizontal tube absorbers," *Proceedings of International sorption heat pump conference Munich*, pp. 257-267.
- Möller, R. and K. F. Knoche (1996), "Surfactants with $\text{NH}_3\text{-H}_2\text{O}$," *International Journal of Refrigeration*. Vol. 19(5), pp. 317-321 DOI: [https://doi.org/10.1016/S0140-7007\(96\)00035-7](https://doi.org/10.1016/S0140-7007(96)00035-7).
- Murai, Y., Y. Tasaka, Y. Nambu, Y. Takeda and S. R. Gonzalez A (2010), "Ultrasonic detection of moving interfaces in gas-liquid two-phase flow," *Flow Measurement and Instrumentation*. Vol. 21(3), pp. 356-366 DOI: <https://doi.org/10.1016/j.flowmeasinst.2010.03.007>.
- Nagavarapu, A. K. (2012). *Binary fluid heat and mass exchange at the microscale in internal and external ammonia-water absorption*. Ph.D. Thesis, Georgia Institute of Technology.
- Nagavarapu, A. K. and S. Garimella (2019), "Experimentally validated models for falling-film absorption around microchannel tube banks: Heat and mass transfer," *International Journal of Heat and Mass Transfer*. Vol. 139, pp. 303-316 DOI: <https://doi.org/10.1016/j.ijheatmasstransfer.2019.05.024>.
- Nakoryakov, V. E., N. I. Grigoryeva, N. S. Bufetov and R. A. Dekhtyar (2008), "Heat and mass transfer intensification at steam absorption by surfactant additives," *International Journal of Heat and Mass Transfer*. Vol. 51(21), pp. 5175-5181 DOI: <https://doi.org/10.1016/j.ijheatmasstransfer.2008.03.018>.
- Nekoeian, S., M. Aghajani, S. M. Alavi and F. Sotoudeh (2019), "Effect of surfactants on mass transfer coefficients in bubble column contactors: an interpretative critical review study." (0), p. 20180089 DOI: <https://doi.org/10.1515/revce-2018-0089>.
- Nordgren, M. and F. Setterwall (1996), "An experimental study of the effects of surfactant on a falling liquid film," *International Journal of Refrigeration*. Vol. 19(5), pp. 310-316 DOI: [https://doi.org/10.1016/S0140-7007\(96\)00033-3](https://doi.org/10.1016/S0140-7007(96)00033-3).

- Nusselt, W. (1916), "The surface condensation of water vapor," *Zeitschrift Des Vereines Deutscher Ingenieure*. Vol. 60, pp. 541-546.
- Olbricht, M., F. Lonardi and A. Luke (2018), "Performance improvement of absorption chillers by means of additives – A numerical study," *Solar Energy*. Vol. 166, pp. 138-145 DOI: <https://doi.org/10.1016/j.solener.2018.03.048>.
- Orell, A. and J. W. Westwater (1962), "Spontaneous interfacial cellular convection accompanying mass transfer: Ethylene glycol-acetic acid-ethyl acetate," *AIChE Journal*. Vol. 8(3), pp. 350-356 DOI: 10.1002/aic.690080317.
- Ozar, B., A. Dixit, S. W. Chen, T. Hibiki and M. Ishii (2012), "Interfacial area concentration in gas–liquid bubbly to churn-turbulent flow regime," *International Journal of Heat and Fluid Flow*. Vol. 38, pp. 168-179 DOI: <https://doi.org/10.1016/j.ijheatfluidflow.2012.08.006>.
- Patel, V. K. and R. V. Rao (2010), "Design optimization of shell-and-tube heat exchanger using particle swarm optimization technique," *Applied Thermal Engineering*. Vol. 30(11), pp. 1417-1425 DOI: <https://doi.org/10.1016/j.applthermaleng.2010.03.001>.
- Price, B. C. and K. J. Bell (1974), "Design of binary vapor condensers using Colburn-Drew equations," *AIChE Symp. Series*. Vol. 70, pp. 163-171.
- Proctor, S. J., M. W. Biddulph and K. R. Krishnamurthy (1998), "Effects of Marangoni surface tension forces on modern distillation packings," *AIChE Journal*. Vol. 44(4), pp. 831-835 DOI: 10.1002/aic.690440408.
- Raisul Islam, M., N. E. Wijesundera and J. C. Ho (2004), "Simplified models for coupled heat and mass transfer in falling-film absorbers," *International Journal of Heat and Mass Transfer*. Vol. 47(2), pp. 395-406 DOI: <https://doi.org/10.1016/j.ijheatmasstransfer.2003.07.001>.
- Rozenblit, R., M. Gurevich, Y. Lengel and G. Hetsroni (2006), "Flow patterns and heat transfer in vertical upward air–water flow with surfactant," *International Journal of Multiphase Flow*. Vol. 32(8), pp. 889-901 DOI: <https://doi.org/10.1016/j.ijmultiphaseflow.2006.03.003>.
- Ruckenstein, E., O. Smigelschi and D. G. Suci (1970), "A steady dissolving drop method for studying the pure Marangoni effect," *Chemical Engineering Science*. Vol. 25(8), pp. 1249-1254 DOI: [https://doi.org/10.1016/0009-2509\(70\)80001-X](https://doi.org/10.1016/0009-2509(70)80001-X).
- Ruhemann, M. (1947), "A study of the transfer of heat and matter in an ammonia absorber," *Transactions of Institute of Chemical Engineers*. Vol. 25, pp. 158-162.
- Sardeing, R., P. Painmanakul and G. Hébrard (2006), "Effect of surfactants on liquid-side mass transfer coefficients in gas–liquid systems: A first step to modeling,"

Chemical Engineering Science. Vol. 61(19), pp. 6249-6260 DOI:
<https://doi.org/10.1016/j.ces.2006.05.051>.

- Sehgal, S., J. L. Alvarado, I. G. Hassan and S. T. Kadam (2021), "A comprehensive review of recent developments in falling-film, spray, bubble and microchannel absorbers for absorption systems," *Renewable and Sustainable Energy Reviews*. Vol. 142, p. 110807 DOI: <https://doi.org/10.1016/j.rser.2021.110807>.
- Semkov, K. R. and N. Kolev (1991), "On the evaluation of the interfacial turbulence (the Marangoni effect) in gas (vapour)—liquid mass transfer: Part I. A method for estimating the interfacial turbulence effect," *Chemical Engineering and Processing: Process Intensification*. Vol. 29(2), pp. 77-82 DOI: [https://doi.org/10.1016/0255-2701\(91\)87016-V](https://doi.org/10.1016/0255-2701(91)87016-V).
- Shah, M. M. (1979), "A general correlation for heat transfer during film condensation inside pipes," *International Journal of Heat and Mass Transfer*. Vol. 22(4), pp. 547-556 DOI: [https://doi.org/10.1016/0017-9310\(79\)90058-9](https://doi.org/10.1016/0017-9310(79)90058-9).
- Shi, J. (1994), "Good features to track," *Proceedings of 1994 Proceedings of IEEE conference on computer vision and pattern recognition*, pp. 593-600.
- Shindler, L., M. Moroni and A. Cenedese (2012), "Using optical flow equation for particle detection and velocity prediction in particle tracking," *Applied Mathematics and Computation*. Vol. 218(17), pp. 8684-8694 DOI: <https://doi.org/10.1016/j.amc.2012.02.030>.
- Silver, L. (1947), "Gas cooling with Aqueous Condensation," *Transactions of American Institute of Chemical Engineers*. Vol. 25, pp. 30-42.
- Smigelschi, O., D. G. Suciú and E. Ruckenstein (1969), "Absorption under the action of artificially provoked Marangoni effect," *Chemical Engineering Science*. Vol. 24(8), pp. 1227-1234 DOI: [https://doi.org/10.1016/0009-2509\(69\)85043-8](https://doi.org/10.1016/0009-2509(69)85043-8).
- Sözen, A. (2001), "Effect of heat exchangers on performance of absorption refrigeration systems," *Energy Conversion and Management*. Vol. 42(14), pp. 1699-1716 DOI: [https://doi.org/10.1016/S0196-8904\(00\)00151-5](https://doi.org/10.1016/S0196-8904(00)00151-5).
- Spore, J. W., S. J. Jolly-Woodruff, T. K. Knight, J. C. Lin, R. A. Nelson, K. O. Pasamehmetoglu, R. G. Steinke and C. Unal (1993). "TRACE V5.0 theory manual," US Nuclear Regulatory Commission, Washington, D.C.
- Staedter, M. A. and S. Garimella (2018a), "Design and modeling of a microscale diabatic distillation column for small capacity ammonia–water absorption systems," *International Journal of Refrigeration*. Vol. 94, pp. 161-173 DOI: <https://doi.org/10.1016/j.ijrefrig.2018.06.018>.
- Staedter, M. A. and S. Garimella (2018b), "Development of a micro-scale heat exchanger based, residential capacity ammonia–water absorption chiller," *International*

- Journal of Refrigeration*. Vol. 89, pp. 93-103 DOI:
<https://doi.org/10.1016/j.ijrefrig.2018.02.016>.
- Staedter, M. A., K. Keniar and S. Garimella (2018), "Hydrodynamic considerations and design concepts for optimal thermal compressors," *International Journal of Heat and Mass Transfer*. Vol. 127, pp. 209-223 DOI:
<https://doi.org/10.1016/j.ijheatmasstransfer.2018.06.109>.
- Stauffer, C. E. (1965), "The Measurement of Surface Tension by the Pendant Drop Technique," *The Journal of Physical Chemistry*. Vol. 69(6), pp. 1933-1938 DOI:
 10.1021/j100890a024.
- Sternling, C. V. and L. E. Scriven (1959), "Interfacial turbulence: Hydrodynamic instability and the marangoni effect," *AIChE Journal*. Vol. 5(4), pp. 514-523 DOI: 10.1002/aic.690050421.
- Sun, Z. F., K. T. Yu, S. Y. Wang and Y. Z. Miao (2002), "Absorption and Desorption of Carbon Dioxide into and from Organic Solvents: Effects of Rayleigh and Marangoni Instability," *Industrial & Engineering Chemistry Research*. Vol. 41(7), pp. 1905-1913 DOI: 10.1021/ie010707+.
- Taitel, Y., D. Bornea and A. E. Dukler (1980), "Modelling flow pattern transitions for steady upward gas-liquid flow in vertical tubes," *AIChE Journal*. Vol. 26(3), pp. 345-354 DOI: 10.1002/aic.690260304.
- Takagi, S. and Y. Matsumoto (2011), "Surfactant Effects on Bubble Motion and Bubbly Flows," *Annual Review of Fluid Mechanics*. Vol. 43(1), pp. 615-636 DOI: 10.1146/annurev-fluid-122109-160756.
- Takagi, S., T. Ogasawara and Y. Matsumoto (2008), "The effects of surfactant on the multiscale structure of bubbly flows," *Philosophical Transactions of the Royal Society A: Mathematical, Physical and Engineering Sciences*. Vol. 366(1873), pp. 2117-2129 DOI: <https://doi.org/10.1098/rsta.2008.0023>.
- Tanford, C. (1974), "Theory of micelle formation in aqueous solutions," *The Journal of Physical Chemistry*. Vol. 78(24), pp. 2469-2479 DOI: 10.1021/j100617a012.
- Taylor, B. N. and C. E. Kuyatt (1994). "NIST Technical Note 1297."
- Triché, D., S. Bonnot, M. Perier-Muzet, F. Boudéhenn, H. Demasles and N. Caney (2017), "Experimental and numerical study of a falling film absorber in an ammonia-water absorption chiller," *International Journal of Heat and Mass Transfer*. Vol. 111, pp. 374-385 DOI:
<https://doi.org/10.1016/j.ijheatmasstransfer.2017.04.008>.
- Van Nimwegen, A. T., L. M. Portela and R. A. W. M. Henkes (2015), "The effect of surfactants on air–water annular and churn flow in vertical pipes. Part 1: Morphology of the air–water interface," *International Journal of Multiphase*

- Flow*. Vol. 71, pp. 133-145 DOI:
<https://doi.org/10.1016/j.ijmultiphaseflow.2014.03.008>.
- Van Nimwegen, A. T., L. M. Portela and R. A. W. M. Henkes (2016), "The effect of surfactants on upward air–water pipe flow at various inclinations," *International Journal of Multiphase Flow*. Vol. 78, pp. 132-147 DOI:
<https://doi.org/10.1016/j.ijmultiphaseflow.2015.07.011>.
- Wang, G., M. Zhang, Z. Dang and M. Ishii (2021), "Axial interfacial area transport and flow structure development in vertical upward bubbly and slug flow," *International Journal of Heat and Mass Transfer*. Vol. 169, p. 120919 DOI:
<https://doi.org/10.1016/j.ijheatmasstransfer.2021.120919>.
- Wasekar, V. M. and R. M. Manglik (1999), "A Review of Enhanced Heat Transfer in Nucleate Pool Boiling of Aqueous Surfactant and Polymeric Solutions." Vol. 6(2-4), pp. 135-150 DOI: 10.1615/JEnhHeatTransf.v6.i2-4.70.
- Wilke, C. and P. Chang (1955), "Correlation of diffusion coefficients in dilute solutions," *AIChE journal*. Vol. 1(2), pp. 264-270.
- Wu, H., T.-W. Chung and M.-H. Lai (2001), "Effects of Marangoni Convection on the Mass Transfer Performance in a Packed-Bed Absorber," *Industrial & Engineering Chemistry Research*. Vol. 40(3), pp. 885-891 DOI: 10.1021/ie000468a.
- Wu, W.-T., Y.-M. Yang and J.-R. Maa (1998), "Effect of surfactant additive on pool boiling of concentrated lithium bromide solution," *International Communications in Heat and Mass Transfer*. Vol. 25(8), pp. 1127-1134 DOI:
[https://doi.org/10.1016/S0735-1933\(98\)00103-1](https://doi.org/10.1016/S0735-1933(98)00103-1).
- Xu, Z. Y. and R. Z. Wang (2016), "Absorption refrigeration cycles: Categorized based on the cycle construction," *International Journal of Refrigeration*. Vol. 62, pp. 114-136 DOI: <https://doi.org/10.1016/j.ijrefrig.2015.10.007>.
- Zhang, H., D. Yin, S. You, W. Zheng and S. Wei (2019), "Experimental investigation of heat and mass transfer in a LiBr-H₂O solution falling film absorber on horizontal tubes: Comprehensive effects of tube types and surfactants," *Applied Thermal Engineering*. Vol. 146, pp. 203-211 DOI:
<https://doi.org/10.1016/j.applthermaleng.2018.09.127>.
- Zhang, S., D. Wang, F. Bu, X. Zhang and P. Fan (2013), "Gas–liquid mass transfer in the presence of ionic surfactant: effect of counter-ions and interfacial turbulence," *Surface and Interface Analysis*. Vol. 45(7), pp. 1152-1157 DOI:
<https://doi.org/10.1002/sia.5242>.
- Zukauskas, A. (1972), "Heat transfer from tubes in cross flow," *Advances in heat transfer*. Vol. 8(1), pp. 93-160.